Chapter 23

GEOKINETICS

Sections 23.1, 23.2, and 23.3   J.C. Johnston and J.C. Battis
Section 23.4   J.J. Cipar and G.H. Cabaniss
Section 23.5   J.A. Shearer and J.M. Novak Capt. USAF

The surface of the earth is in constant motion in response to natural (gravitational, rotational, hydrological, meteorological, tectonic) and manmade (detonations, surface loading, vibrating machinery) forces. Some of these motions are of great interest to earth scientists and engineers, but many compose the background noise spectrum from which the signals of interest must be extracted.

The nature of the motions range from transient vibrations caused by earthquakes through continuous long period oscillations. There are also non-periodic rotations of large blocks of the outer shell of the earth. Due to the small amplitude or low frequency of these motions, most go unnoticed in the common experience. The most catastrophic of these motions are the transient waves generated by large earthquakes or explosions. In this chapter the general characteristics, magnitude, and measurement of crustal motions will be discussed.

23.1 STRUCTURE OF THE EARTH

The mechanical and chemical properties of the earth, such as density, rigidity and compressibility, are strong functions of depth and therefore pressure [Anderson and Hart, 1976]. Four major discontinuities in these properties have been identified and on this basis the interior of the earth has been subdivided into four regions that on a gross scale are laterally homogeneous (Figure 23-1). From the surface downward these regions are as follows:

1. Crust—This region ranges in thickness from 5 km beneath oceans to 35 km beneath continents, to a maximum of 60 km beneath the Himalaya Mountains. The crust, which is composed of silicates, exhibits radial and lateral homogeneity to a much greater extent than any of the other three zones. The lower boundary of the crust is defined by a sharp seismic velocity discontinuity, known as the Mohorovicic discontinuity, commonly called the "Moho." Typical upper crustal rock density is 2.5 g/cm³. The variation in depth to the Moho is thought to be an expression of isostatic equilibrium since the crustal material is of lower den-

sity than that of the mantle. In other words, the so called "crustal roots" beneath continents or mountain ranges compensate for the additional material in such a way that the pressure from a vertical column of mass at some depth anywhere around the planet will be equal (Figure 23-2). This process is not instantaneous and it can be demonstrated that some areas of the world have not reached isostatic equilibrium.

2. Mantle—Starting at the base of the crust, the mantle extends to a depth of 2885 km. The upper
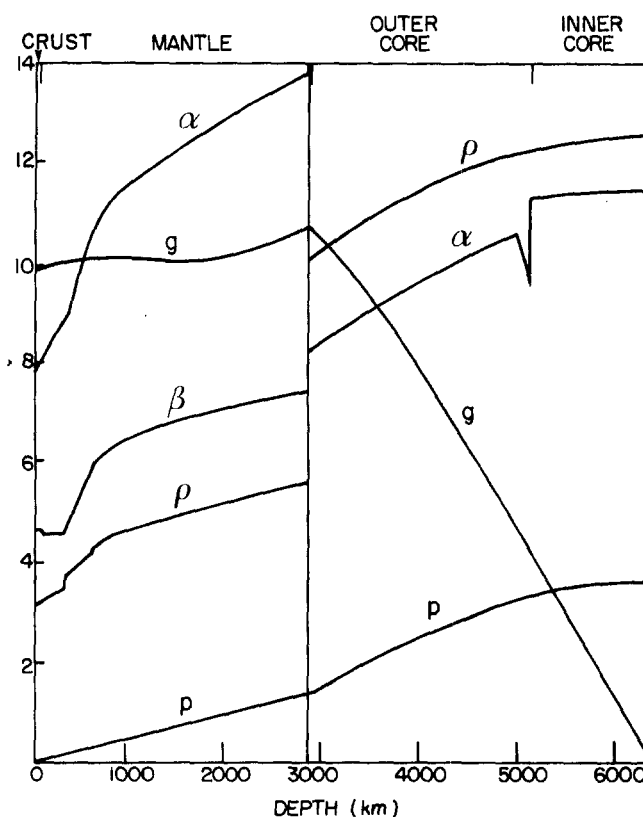

Figure 23-1. Variation of physical properties with depth in the earth (P-pressure in 10^{12} dyn/cm; ρ = density in gm/cm³; α, β = P- and S-wave velocities in km/s; g = acceleration of gravity in 10^2cm/s²) [Anderson and Hart, 1976].

PRESSURE AT BOTTOM OF COLUMN ρ IN UNITS OF mass/length
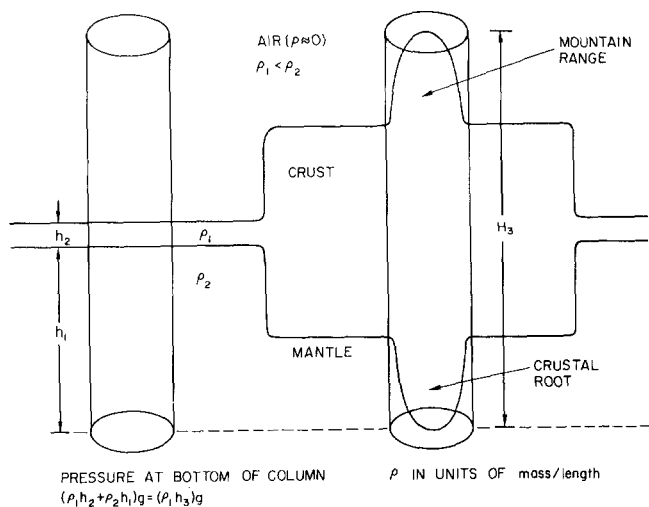$(\rho_1 h_2 + \rho_2 h_1)g = (\rho_1 h_3)g$

Figure 23-2.   Isostacy principle—crustal roots under continents and mountain ranges permit a spherical shell of equal pressure to exist at some depth beneath the surface of the earth.

cussions can be found in geological and geophysical texts published since 1970 (for example, Garland [1971] and Wyllie [1971]). There are also several collections of scientific papers (such as Bird and Isacks [1972] and Cox [1973]) that illustrate the chronological development of the theory.

Plate tectonics is primarily concerned with the kinematics of the first several hundred kilometers below the surface of the earth. This region is divided into two zones: the lithosphere, from the Greek word meaning "rock", and the asthenosphere, from the Greek word meaning "weak" or lacking strength. The lithosphere exhibits finite strength and is capable of brittle fracture, while the asthenosphere can be viewed as a basement of weak material having low mechanical strength. The lithosphere includes the crust, but also extends into the upper mantle. The boundary between these two regions is associated with the top of a seismic low velocity zone (LVZ) which typically occurs at approximately 100 km depth. See Dorman [1969] and Figure

part of the mantle is probably composed mainly of peridotites (olivines and pyroxines). The term "pyrolite" has been applied to the composition of the upper mantle [Clark and Ringwood, 1964]. The composition of the lower mantle is uncertain. It may consist of oxides and silicates of magnesium and iron with small amounts of aluminum and calcium [Verhoogen et al, 1970]. Typical mantle densities range from 3 to 5 g/cm^3.

3. Outer core—This region ranges from a depth of 2885 to 5155 km. It is believed to be composed of liquid iron and nickel and therefore cannot support shear forces. The density of the outer core ranges from approximately 9 g/cm^3 to 12 g/cm^3.

4. Inner core—Beginning at a depth of 5155 km, the inner core extends to the center (6371 km depth) of the earth. Like the outer core, it is believed to consist of iron and nickel; however, as a result of the extreme pressure it is solid. The density of the inner core material is approximately 11 g/cm^3.

In geophysical literature there is another radial division of the earth into the lithosphere and the asthenosphere. This is primarily a division based on strength, and the boundary does not correspond to any of the ones previously discussed. The next section, which is an overview of the theory of plate tectonics, is concerned with this division.

23.2 PLATE TECTONICS

The development of the theory of plate tectonics represents a revolution in the understanding of the evolution of the surface of the earth. Because the theory is referred to in several of the following sections, a brief survey of the subject will be presented here. More comprehensive dis-

Figure 23-3.   Crust and upper mantle velocity distributions (solid line—Pacific Ocean; dash line—Alpine; dotted line—Canadian Shield). Thick horizontal bars indicate top of low velocity zone [Dorman, 1969].

SHEAR VELOCITY (km/sec)
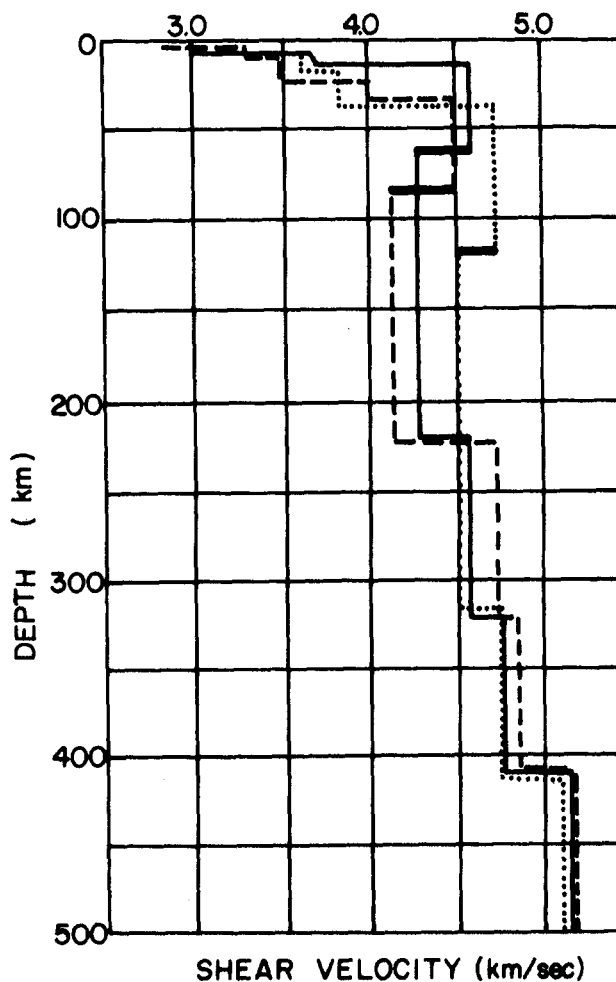
23-3. The depth of this interface varies with tectonic province, that is, whether it is beneath oceans, continents, or mountains. It should be noted that the lithosphere-asthenosphere boundary does not correspond to the classical crust-mantle velocity discontinuity, the Moho.

Major fracture systems occur in the lithosphere, dividing the outer shell of the earth into a number of sections or plates (Figure 23-4). Twelve major plates and numerous minor plates capable of motion along the surface of the earth have been identified. The interior of the plates can be considered essentially rigid and the effect of the interactions of the moving plates confined primarily to the plate margins. Plates can be composed of either oceanic floor, continental material, or both. The major distinction between the theory of plate tectonics and the old concept of continental drift is that continents are not separate mobile entities, but are part of the plates. For example, as seen in Figure 23-4, the North American plate includes a large portion of the Atlantic Ocean as well as the continent of North America.

Three basic types of plate boundaries have been identified. The first type is an extensional margin where new oceanic lithosphere is created. This is referred to as sea-floor spreading and occurs when two adjacent plates are moving away from each other. Here basaltic magma from the asthenosphere is intruded at the margin (Figure 23-5a). Normal faulting, an expression of extension with strike (direction) parallel to the margin axis, is found here. In these areas, the lithosphere is very thin, elevated, and has high heat flow. Examples of this type of boundary are the East

Pacific Rise and the Mid-Atlantic Ridge. Since the area of the surface of the earth must be conserved, it is obvious that there must be a mechanism for destroying lithosphere. This type of margin is called a consuming plate margin or a subduction zone. Subduction occurs when oceanic lithosphere converges with either oceanic or continental lithosphere (Figure 23-5b). The oceanic plate will be overridden by the other plate and sink because it is colder, older, and thus denser than its surroundings. At the point of contact, the subducting plate will down-warp the overriding plate forming a trench. As the subducting plate enters the asthenosphere it is heated until it melts. A chain of volcanoes is formed at the rear of the trench system.

Typical examples of this type of plate boundary are the Japanese island arc system and the Aleutian Islands. Subduction zones exhibit marked gravity anomalies because formation of a trench creates a mass deficiency. These zones are often the sites of the world's largest (fault lengths 100–800 km) and deepest (to depths of 700 km) earthquakes. This zone of earthquakes, not to be confused with the actual slab, is known as the Benioff zone. Various geometries of subducted lithosphere and subduction rates have been identified. Generally, we expect that the faster the subduction rate, the deeper the plate can descend before melting; however, this is also dependent on the time constant for assimilation into the athenosphere. The dip angle of the slabs varies and in some cases fragments of plate seem to have broken off (Figure 23-6). The type of faulting varies with the position on the slab. Because the plate has some flexural
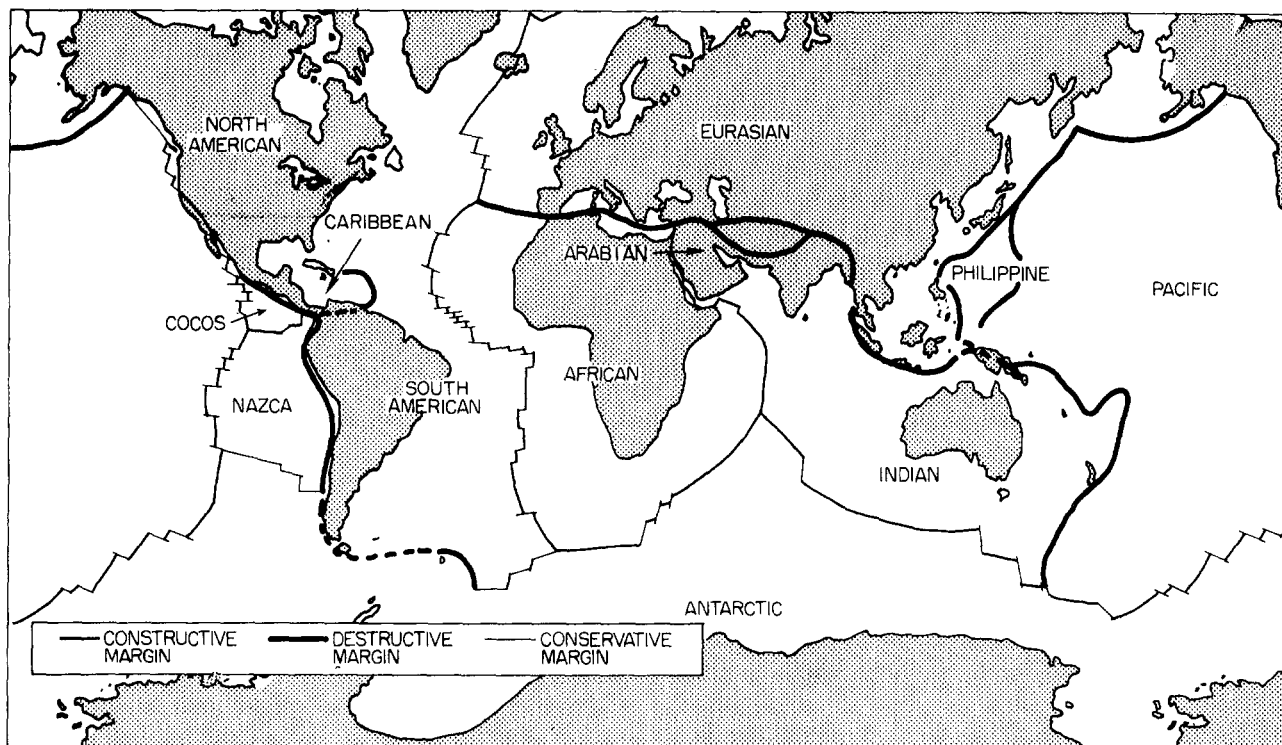

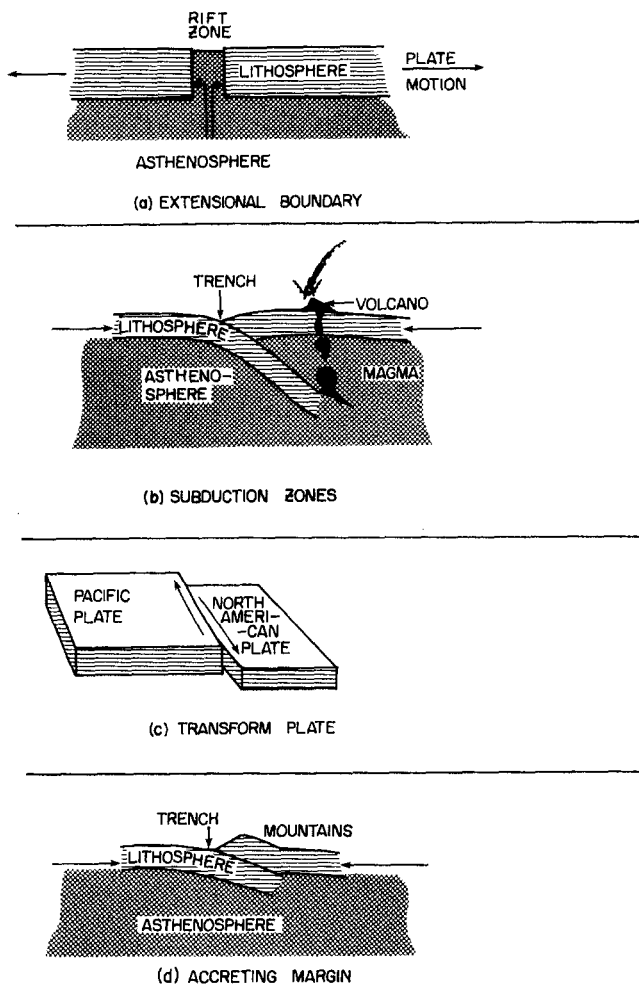Figure 23-4. Major plate boundaries of the world.

Figure 23-5. Plate boundary types.

Figure 23-6. Various geometries of subducting slabs.
(a) shallow angle
(b) steep angle
(c) short slab
(d) broken slab

rigidity, the downgoing slab actually warps upward about the radius of curvature. Tensional faulting is observed in this region. Compressional thrust faulting is found further down the subducted slab. In some areas of the world, parts of the downgoing slab appear to be breaking off and are in tension (axis of least compressive stress is parallel to the slab and dipping down). This could be caused by gravitational sinking [Isacks et al., 1968]. In some cases of subduction of oceanic lithosphere beneath continental lithosphere, slivers of ocean crust have been scraped off onto the continent. These fragments are called "ophiolites" [Gass, 1982].

While the combination of the spreading mid-ocean ridge systems with the subduction zones creates a recycling scheme for the surface of the earth, a third type of boundary neither creates nor destroys lithosphere. If two plates do not converge but slide past each other, the plate margin is called a transform or strike-slip fault. See Figure 23-5c and Wilson [1965]. The San Andreas Fault in California is the best known example of a transform fault. In this case, the only resistance to the relative motion results from irregularities
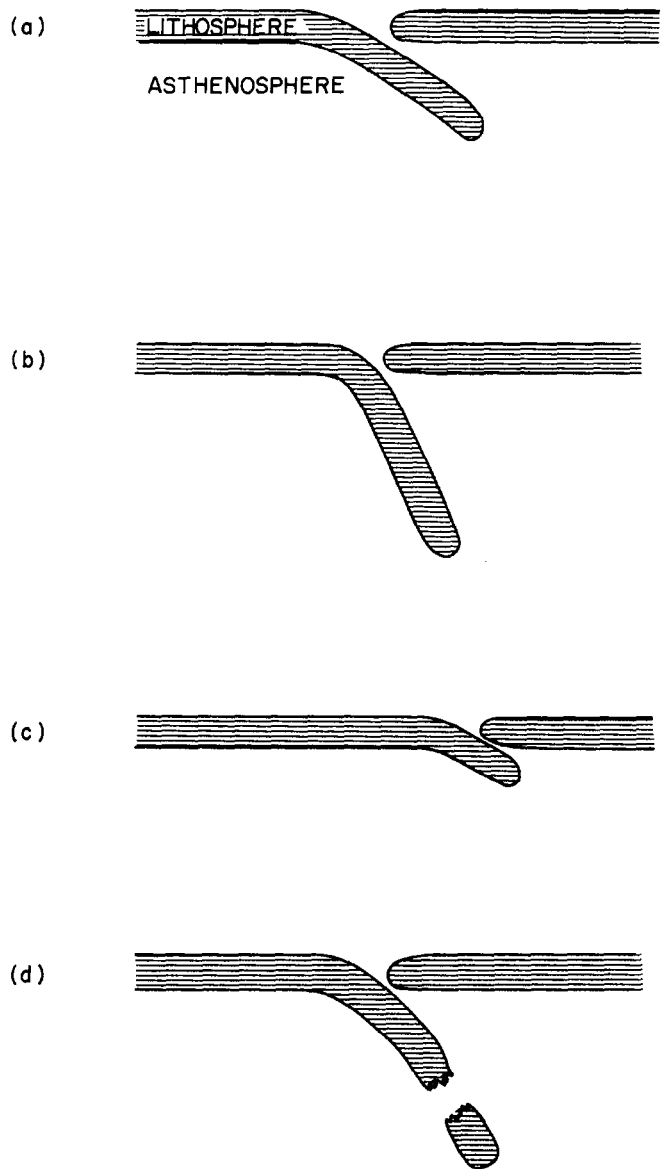
in the plate boundaries and friction between the two plates. In this case, the Pacific plate is rotating in a counterclockwise direction relative to the North American Plate.

It should be noted that the recycling scheme mentioned above refers only to oceanic lithosphere. Continental lithosphere, which is buoyant and thick, generally does not subduct. As a consequence, the oldest oceanic lithosphere (about 200 million years) is younger than most continental lithosphere. When the collision involves continental lithosphere of both plates, the buoyant forces of the overridden plate produce uplift of the overriding plate resulting in mountain building forces (Figure 23-5d). The Tibetan Plateau, site of the convergence of the India and Eurasian

plates, is an example of this type of plate margin. The plate approximation becomes less useful for continent to continent collisions and the plastic properties of the lithosphere must be considered. Since continental lithosphere cannot be destroyed, the oldest rocks in the world are found on the stable, inactive continental shields such as Canada and Africa. Island arcs, which are not part of the continental lithosphere, are usually "scraped off" ih slivers by the overriding plate when the plate subducts. This is thought to be a mechanism for creation of the continents.

23.2.1 Driving Mechanism

The driving mechanism for plate motion is unknown; however, several hypotheses have been proposed. Initially, thermal convection cells in the mantle resulting from dissipation of heat in the deep mantle from radioactive decay were believed to drive the system by exerting viscous drag on the bottom of the lithospheric plates. Although this mechanism has not been discounted, other explanations have been offered. Other hypothetical mechanisms include gravitational pulling by subducting plates, pushing by injection of new crust at mid-ocean ridges (considered unlikely on the basis of simple energy arguments), and excitation by the Chandler wobble or change in the length of day (rotation rate). In the latter, it is unclear which is the cause and which is the effect.

The geometric boundaries of the plates are not static since the processes occurring at any margin may change with time and new plate margins may be created by the subdivision of existing plates. Approximately 200 million years ago, the continental land masses were united in one paleocontinent known as Pangaea. See Figure 23-7 and Dietz and Holden [1970]. Gradually, this single continent has been subdivided by rifting and the creation of new oceans including the Atlantic and Indian Oceans. In addition, the rifting of continents has been initiated at several points but
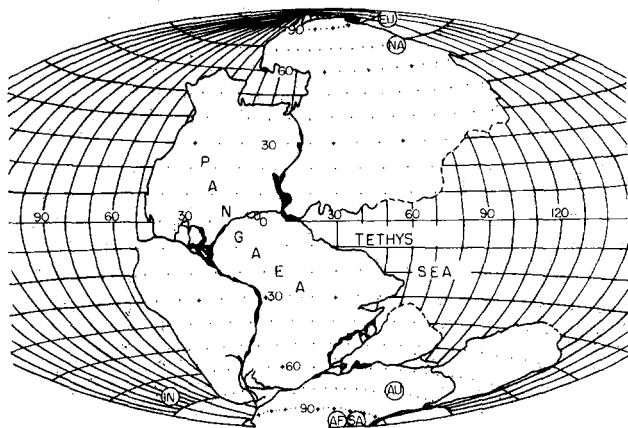

Figure 23-7 Reconstruction of Pangaea from present continents (approximately 200 million years before present) [Dietz and Holden, 1970].

seems to have terminated prior to significant separation. The Mississippi and St. Lawrence River Valleys may be regions of failed rifting. This theory postulates that a plate begins to break up because of upwelling mantle plumes which are convective cells of molten material that reach the surface. It can be shown that the least energy configuration for fracture from a point source is a triple junction with radially symmetric fracture arms at 120 degrees. If several of these spreading arms from other plumes intersect, the coalescing arms become a spreading ridge. The third faulted arm becomes relatively dormant. A name sometimes applied to these "failed arms" is alachogen.

23.2.2 Plate Motions

Relative plate motions can be estimated by the analysis of spreading rates at extensional margins, displacement across transform faults, and earthquake slip at subduction zones. Spreading rates at sea floor spreading ridges are generally measured by paleomagnetic anomalies. When magma is intruded at these ridges, it is heated past the Curie temperature, the temperature at which material gives up its remanent magnetization and realigns itself with the ambient magnetic field. When the magma cools it "freezes" in the ambient magnetic field. This makes estimates of spreading rates possible because of two facts. First, the polarity of the earth's magnetic field reverses itself on a seemingly random basis at periods ranging from thousands to tens of thousands of years. As the plates move away from the ridge, they carry distinctive magnetic signatures on the sea floor. The cause of the reversal is not known. Second, each magnetic signature can be dated by other means, such as radioactive isotope rock dating and fossil remains.

Using a simplified plate structure, Minster and Jordan [1978] estimated the relative plate motions by using an averaging interval of less than three million years. Because any motion on a sphere can be depicted as a rotation, plate motions are given as relative rotation vectors. Each vector gives the latitude and longitude of the radial axis of rotation and the angular velocity. Their calculated relative rotation vectors for abutting plate pairs are given in Table 23-1. It must be remembered that these poles are mathematical and have no physical expressions.

In addition to the relative movement of the plates, the entire lithosphere is apparently free to slip around on the surface of the earth like a shell. Mantle plumes, which are theorized to be areas of hot, upwelling, mantle material, appear to provide a stationary reference frame for the estimation of these absolute motions [Morgan, 1972]. Mantle plumes have as surface manifestations localized volcanic activity such as that found in Iceland and the Hawaiian Islands. As a plate moves over a plume, the active center of volcanism appears to move in a direction opposite to that of the plate motion leaving a trail of extinct volcanism on the plate, for example the Emperor Seamount Chain off

CHAPTER 23

Table 23-1. Locations of poles of rotation for relative plate motions [Minster and Jordan, 1978].

Plate Pair	Relative Rotation Vector*						Error Ellipse[+]			Importance Distribution			
	θ °N	σ_θ deg	ϕ °E	σ_ϕ deg	ω deg/m.y.	σ_ω deg/m.y.	ζ_{max} deg	σ_{max} deg	σ_{min} deg	RA	TF	SV	Total
NOAM-PCFC	48.77	1.10	-73.91	1.94	0.852	0.025	S71°E	1.30	1.08	0.405	0.398	0.694	1.497
COCO-PCFC	38.72	0.89	-107.39	1.01	2.208	0.070	S37°E	1.00	0.63	0.977	0.272	0.009	1.258
NAZC-PCFC	56.64	1.89	-87.88	1.81	1.539	0.029	N09°E	1.91	0.96	0.849	0.341	0.038	1.228
EURA-PCFC	60.64	1.04	-78.92	3.04	0.977	0.027	S78°E	1.51	1.02	0	0	0	0
INDI-PCFC	60.71	0.77	-5.79	1.83	1.246	0.023	S82°E	0.90	0.76	0	0	0.246	0.246
ANTA-PCFC	64.67	0.90	-80.23	2.32	0.964	0.014	N52°E	1.11	0.75	1.200	0.811	0.039	2.050
COCO-NOAM	29.80	1.06	-121.28	2.07	1.489	0.070	S75°E	1.84	0.99	0	0	0.165	0.165
AFRC-NOAM	80.43	1.57	56.36	35.29	0.258	0.019	N86°E	5.88	1.51	0.851	0.246	0.091	1.188
EURA-NOAM	65.85	6.17	132.44	5.06	0.231	0.015	S14°E	6.36	1.39	1.055	0.626	0.366	2.047
NOAM-CARB	-33.83	9.19	-70.48	2.76	0.219	0.052	S13°E	9.42	0.97	0.952	1.741	0.253	2.946
COCO-CARB	23.60	1.48	-115.55	2.26	1.543	0.084	S63°E	2.24	1.21	0	0	0.111	0.111
NAZC-CARB	47.30	5.37	-97.57	4.57	0.711	0.056	S19°E	5.59	0	0	0	0	
COCO-NAZC	5.63	1.40	-124.40	2.61	0.972	0.065	N89°E	2.60	1.40	1.829	0.732	0.076	2.637
NOAM-SOAM	25.57	7.12	-53.82	6.22	0.167	0.029	S14°E	7.22	5.49	0	0	0	0
CARB-SOAM	73.51	11.75	60.84	48.86	0.202	0.038	S52°E	16.84	6.84	0	0	0	0
NAZC-SOAM	59.08	3.76	-94.75	3.73	0.835	0.034	S05°E	3.77	1.90	0	0	0.464	0.464
AFRC-SOAM	66.56	2.83	-37.29	2.65	0.356	0.010	S08°E	2.85	0.98	1.201	1.108	0.072	2.381
ANTA-SOAM	87.69	1.30	75.20	79.29	0.302	0.018	N84°E	3.22	1.26	0.167	0.608	0.283	1.058
INDI-AFRC	17.27	0.97	46.02	1.06	0.644	0.014	S47°E	1.24	0.66	0.843	1.098	0	1.941
ARAB-AFRC	30.82	3.44	6.43	11.48	0.260	0.047	S79°E	10.02	2.93	1.989	0.934	0.077	3.000
AFRC-EURA	25.23	4.25	-21.19	0.98	0.104	0.036	S01°E	4.25	0.89	0	0.783	1.167	1.950
INDI-EURA	19.71	1.40	38.46	2.66	0.698	0.024	S65°E	2.72	0.90	0	0	0	0
ARAB-EURA	29.82	2.53	-1.64	9.57	0.357	0.054	S85°E	8.33	2.45	0	0	0	0
INDI-ARAB	7.08	2.15	63.86	2.30	0.469	0.066	S51°E	2.51	1.89	0	0	0	0
NAZC-ANTA	43.21	4.50	-95.02	3.28	0.605	0.039	S01°E	4.50	2.39	0.246	0.058	0.222	0.526
AFRC-ANTA	9.46	3.77	-41.70	3.55	0.149	0.009	S42°E	4.93	1.45	0.697	1.243	0.195	2.135
INDI-ANTA	18.67	1.16	32.74	1.41	0.673	0.011	S62°E	1.39	1.10	1.012	0.135	0.025	1.172
Total										14.273	11.134	4.593	30.000

*First plate named moves counterclockwise with respect to the second. Uncertainties are the standard deviations of marginal distributions.
[+]One-sigma error ellipses are specified by the azimuth ζ_{max} of the major axis; lengths of the axes are geocentric angles.

Hawaii. By dating the volcanic rocks at various places along the island chain, the plate motion relative to this so-called "hot spot frame of reference" can be determined. The absolute rotation vectors, (with respect to the rotation axis of the earth) as determined by Minster and Jordan [1978] assuming stationary mantle plumes, are shown in Table 23-2.

23.3 SHORT PERIOD MOTIONS SEISMOLOGY

Seismology is commonly defined as the study of elastic waves that propagate through the earth, the study of their source, and the analysis of the waves to determine the physical properties and processes of the earth. Although seismology is classically concerned with the study of earthquakes, it has expanded to include the study of any source of elastic waves ranging from nuclear explosions to cultural activities. The common characteristics of these sources are the generation of transient signals with a concentration of energy at relatively high frequencies as compared to other earth motions such as solid earth tides.

The most significant class of elastic wave sources, in terms of radiated energy and frequency of occurrence, is earthquakes. An earthquake is defined as the sudden release of strain energy by the rupturing of rocks in which the strain energy has gradually accumulated. Although additional mechanisms such as instantaneous volumetric change accompanying a chemical phase transition, ice fractures (cryoseisms), and rock bursts have been suggested for limited classes of earthquakes, almost all earthquakes can be considered rupture type events. Fracture begins at one point, spreading over the fault plane at a rupture velocity of 2 to 3 km/s. As the rupture front reaches each point, the abutting surfaces break and slide against each other. The velocity of the particle movement on either side of the fault plane is typically on the order of 1 to 2 m/s. Note that two processes are at work: the propagation of the rupture over the fault plane and also relative motion of the sides of the fault. In some instances, fault rupture has stopped on one branch of a fault system and restarted on an adjacent preexisting fault. This behavior, known as "incoherent" rupture, can generate complexities on the seismic recordings known as starting and stopping phases. The June 1966 Parkfield event [Lindh and Boore, 1981] is an example.

Table 23-2. Locations of poles of rotation for absolute plate motions [Minster and Jordan, 1978].

Plate	Absolute Rotation Vector							Error Ellipse		
	θ °N	σ_θ deg	ϕ °E	σ_ϕ deg	ω deg/m.y.	σ_ω deg/m.y.	ζ_{max} deg	σ_{max} deg	σ_{min} deg
AFRC	18.76	33.93	−21.76	42.20	0.139	0.055	S73°E	40.40	33.24
ANTA	21.85	91.81	75.55	63.20	0.054	0.091	N12°E	93.01	56.12
ARAB	27.29	12.40	−3.94	18.22	0.388	0.067	S76°E	16.38	12.11
CARB	−42.80	39.20	66.75	40.98	0.129	0.104	N30°E	43.21	23.90
COCO	21.89	3.08	−115.71	2.81	1.422	0.119	S32°E	3.35	2.25
EURA	0.70	124.35	−23.19	146.67	0.038	0.057	S67°E	151.10	118.90
INDI	19.23	6.96	35.64	6.57	0.716	0.076	S25°E	7.16	5.97
NAZC	47.99	9.36	−93.81	8.14	0.585	0.097	S02°E	9.37	5.43
NOAM	−58.31	16.21	−40.67	39.62	0.247	0.080	S57°E	23.12	12.14
PCFC	−61.66	5.11	97.19	7.71	0.967	0.085	S16°E	5.23	3.50
SOAM	−82.28	19.27	75.67	85.88	0.285	0.084	N03°E	19.28	11.38

Earthquake location is described by the following convention: the actual location, possibly at some depth below the surface, is called the hypocenter or the focus; the projection of the focus onto the surface of the earth is called the earthquake epicenter.

Seismologists measure earth motion as a function of time with seismometers or accelerometers. See Aki and Richards [1980] for a discussion of these instruments. A typical seismometer is a velocity sensor consisting of a damped pendulum free to move in a magnetic coil.

23.3.1 Seismic Waves

For any given earthquake source, the characteristics of the mechanism of faulting (for example, focal mechanism and rupture velocity) will determine the energy distribution with respect to frequency and the radiation pattern of that energy. However, earth motions produced by any seismic source are limited to only four categories of waves: two are body waves and two are surface waves [Bath, 1973]. Body waves propagate through the earth while surface waves propagate along the surface of the earth. The first type of body wave is the compressional or dilatational wave, designated as the P-wave, ("primary" or "pressure") and the second is the S-wave ("shear" or "secondary"). The P-wave is analogous to an acoustic pressure wave with particle motion parallel to the direction of propagation as indicated in Figure 23-8. For the S-wave, particle motion is perpendicular to the direction of motion. The velocities of these waves are given by

$$V_p = \alpha = \sqrt{\frac{\lambda + 2\mu}{\rho}} = \sqrt{\frac{\kappa + (4\mu/3)}{\rho}}$$

[Bullen, 1965]

$$V_s = \beta = \sqrt{\frac{\mu}{\rho}}$$

where V_p is the P-wave velocity, V_s is the S-wave velocity, ρ is the material density, κ is the bulk modulus, μ is the shear modulus, and λ is the Lame parameter. V_p is always greater than V_s. For liquids, the value of μ is zero implying that S-waves can not propagate through liquids. Typical velocity ranges for earth materials are given in Table 23-3 [Crawford, 1974].

A typical simplifying assumption of seismology is that the variation of seismic properties within the earth can be approximated by horizontal layers or radial shells of uniform physical properties. For flat layers, the path of body waves through the medium can be approximated by optical ray theory or Snell's law: sin i/V = P, where i is the angle of
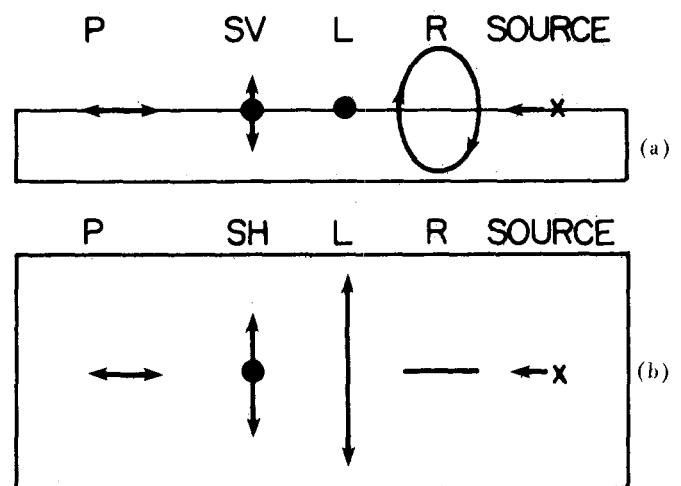

Figure 23-8. Propagational modes for waves traveling along a slab (as seen from the side,(a)and above,(b)

Table 23-3. Typical seismic velocities.

Material	Seismic Velocity ft/s	Seismic Velocity m/s
Loose and dry soils	600– 3 300	180–1 000
Clay and wet soils	2 500– 6 300	760–1 900
Coarse and compact soils	3 000– 8 500	910–2 600
Sandstone and cemented soils	3 000–14 000	910–4 300
Shale and marl	6 000–17 500	1 800–5 300
Limestone—chalk	7 000–21 000	2 100–6 400
Metamorphic rocks	10 000–21 000	3 000–6 400
Volcanic rocks	10 000–22 000	3 000–6 700
Sound plutonic rocks	13 000–25 000	4 000–7 600
Jointed granite	8 000–15 000	2 400–4 600
Weathered rocks	2 000–10 000	600–3 100

incidence of a ray at the interface, V is the appropriate velocity for P or S waves and p, the ray parameter, is a constant along the ray path. At each interface, an impinging P or S wave can generate both reflected and transmitted P and S waves. Thus, the potential paths over which body wave energy can travel from the source to the point of observation grow quickly with an increasing number of layers. Over many paths, however, insufficient energy is transmitted to define a distinct arrival at the observation point.

There is a standard method for identifying body waves as they pass through the earth. See Richter [1958] and Ben-Menahem and Singh [1981] for a complete discussion.

Briefly the convention is

P	P-wave
S	S-wave
PP	P-wave reflected once by the surface
SS	S-wave reflected once from the surface
PPP...,SSS...	Multiply reflected Ps or Ss
SP	S wave reflected by surface changed into P wave.
PSPS...	Reflected wave which changed on reflection into P or S
K	Wave is transmitted through outer core (no shear wave in liquid outer core). Example: PKP
I	Wave passes through inner core
c	Wave reflects off outer core
j	Wave reflects off inner core
p,s..pP,sS..	Depth phase p and s waves travel up to the surface from deep focus earthquakes. Example: pP,sS

These symbols are combined to uniquely describe the wave type and path. Several of these waves are shown in Figure 23-9. The last phases listed, the depth phases, are important for determining the depth of an earthquake. Seismic waves travel from a focus in all directions; when an event occurs, some of the rays travel up to the surface, then reflect downward into the familiar P or S patterns. Since the velocity of propagation is known, the arrival time delay on a seismo-
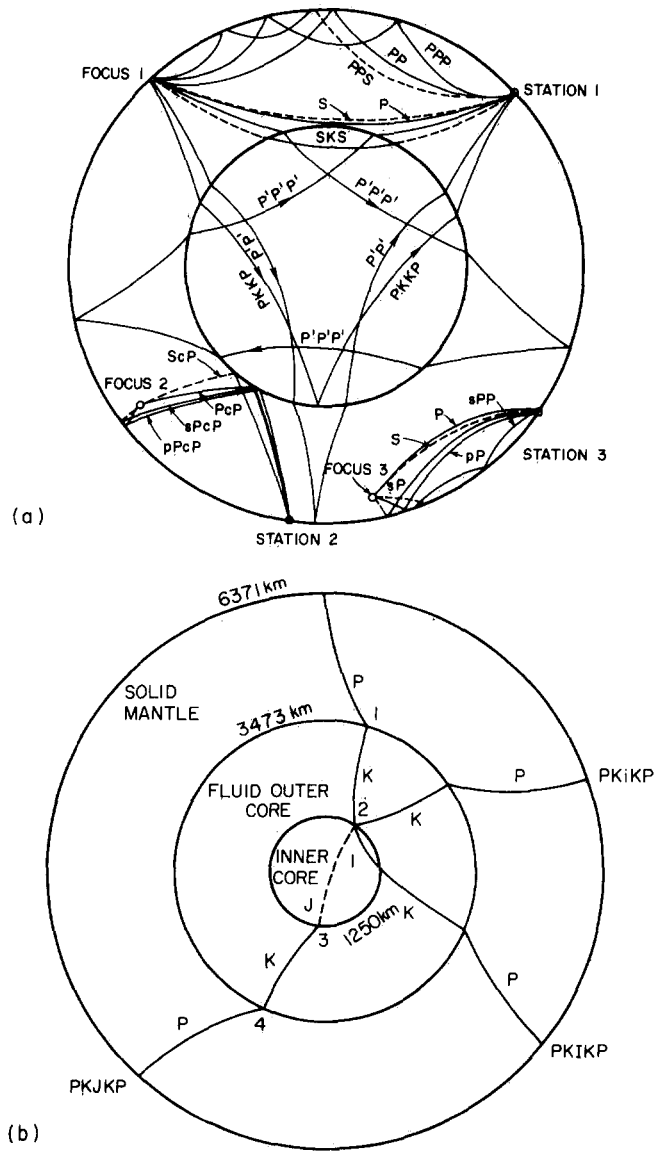

Figure 23-9. Types of body waves, modified from Ben-Menahem and Singh [1981].

gram between a pP and P for example, will be a function of the depth.

In addition to reflection and transmission, seismic body waves can undergo refraction and diffraction. Because of diffraction about the core, for example, a certain distance range on the surface of the earth from the source will experience a "shadow zone" in which direct waves cannot be detected (Figure 23-10).

Surface waves observed on the free surface of the earth are either Love (L) or Rayleigh (R) waves. The particle motion of Love waves is perpendicular to the propagation direction and in the plane of the surface, while Rayleigh waves have retrograde elliptical particle motion in the vertical plane of propagation (Figure 23-8). The particle motion decreases with depth as a function of frequency, with longer periods sampling greater depths. Thus, the velocity of surface waves is a function of the period of the wave and of the velocity structure of the earth (dispersion). In general, Love wave velocities are higher than Rayleigh wave velocities and the velocity of long period waves are faster than short period surface waves. In Figure 23-11 typical Rayleigh and Love wave phase velocities (the velocities at which distinct frequency waves travel) are shown for several geologic structures [Brune, 1969].

A typical seismogram recording will show the following characteristics. The first signal to arrive will be P-waves (including direct P, pP, PP, etc.) which, in a general layered medium, will arrive at the receiver over different paths. This packet will be followed by S-waves, also arriving along different paths. Next, the Love wave will appear with longer periods arriving first. The frequency of Love waves becomes higher and the later Love waves overlap the long-period Rayleigh wave arrivals. Short-period Rayleigh waves arrive last. Many arrivals in the seismogram can be identified with distinct paths through the earth; hence the nomenclature for these distinct signals has been developed. The travel times of these arrivals are well known as functions of event depth and distance from the observation point. By fitting the arrival times of these phases at a number of stations to the known travel time curves for each phase, the epicenter, depth, and origin time of a seismic event can be determined.

Earthquakes or large explosions radiate surface waves in all directions with amplitudes that depend on the radiation pattern [Ben-Menahem and Singh, 1981]. Most commonly observed are surface waves that travel the shortest arc of a great circle between source and station. Large events possess sufficient energy so that surface waves traveling the long arc are also recorded. Surface waves from the largest earthquakes, for example the 1960 Chilean shock, can be detected after multiple trips around the globe. Important information on earthquake source parameters and the deep interior of the earth can be gleaned by studying the velocity and amplitudes of these waves. See, for example, Kanamori [1970] and Kanamori and Cipar [1974].
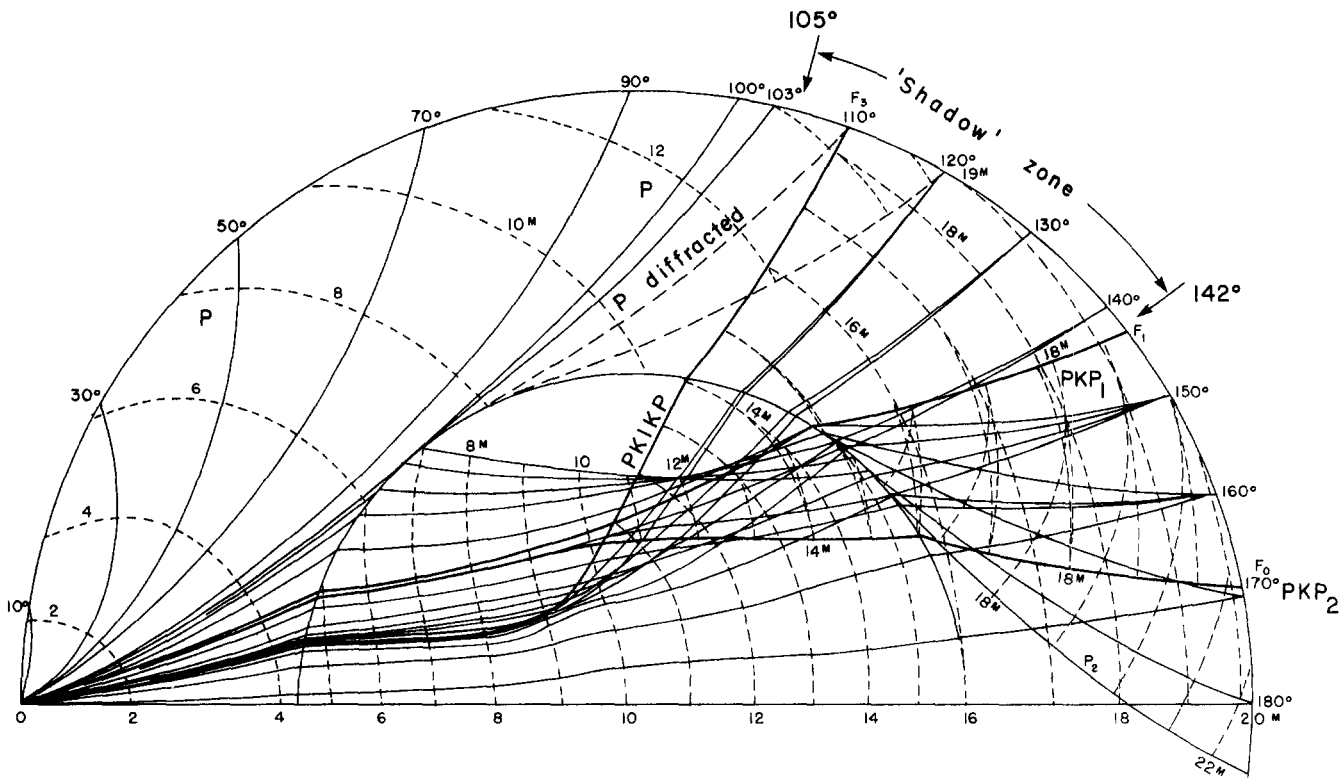

Figure 23-10. P wave, diffracted by the core-mantle interface, creates a "shadow zone" at 105° to 142° distance, modified from Ben-Menahem and Singh [1981].
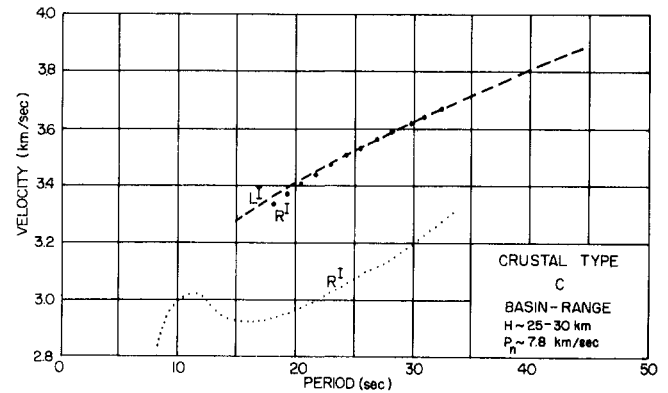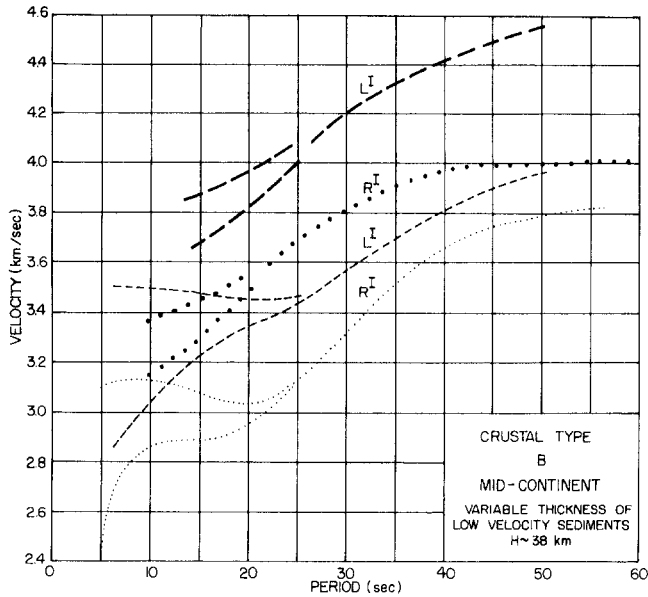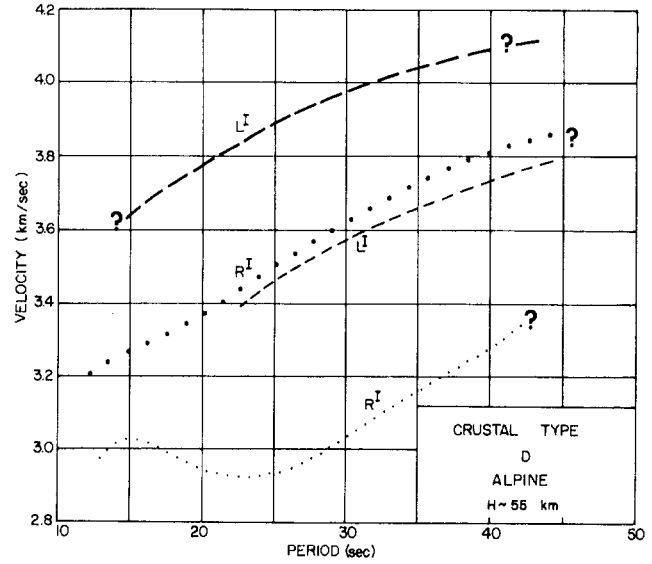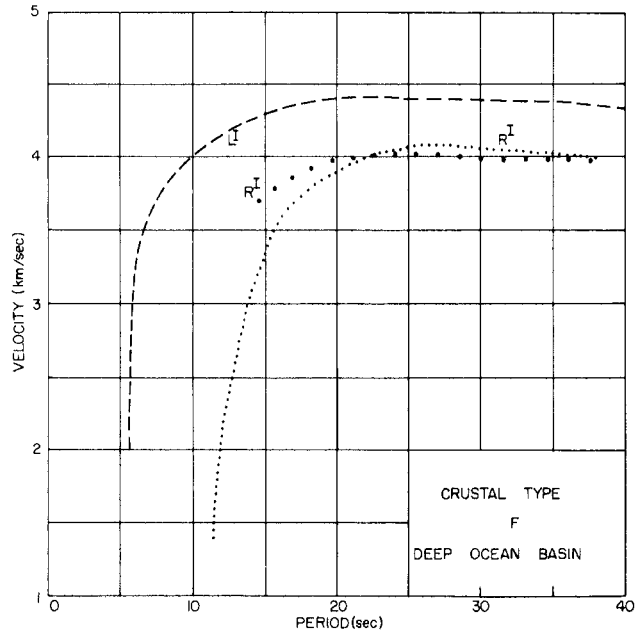
Figure 23-11. Rayleigh (R) and Love (L) wave phase velocity (bold dots and dashes) and group velocity (small dots and dashes) curves for various crustal structures [Brune, 1969].

Surface waves have been described above as traveling over the surface of the earth. Alternatively, the motion of the earth following a giant earthquake can be pictured as superimposed fundamental and higher mode oscillations, analogous to those produced by the ringing of a bell. These free oscillations, in effect standing waves, can be detected up to several days following a large earthquake. A line spectrum of a long-period horizontal seismogram exhibits both torsional and spheroidal oscillations, which are the free oscillation representations of Love and Rayleigh waves,

respectively. Such line spectra exhibit line broadening due to earth rotation, damping, and non-symmetrical earth structure. Details of spectral amplitudes are diagnostic of the source processes of the giant earthquakes which generate these motions. The lowest order free oscillations sample the entire earth (the lowest spheroidal oscillation has a period of 54 minutes) and thus are diagnostic of the structure of the deep interior.

No discussion of wave propagation is complete without mention of attenuation effects. Basically, there are two pro-

cesses at work. The first, geometric spreading, is an inverse square function of the distance from the source, analogous to the falloff of gravity as $1/r^2$ where r is the distance. This occurs because the area at distance r subtended by a steradian (solid angle) is proportional to r^2. The second type, called intrinsic attentuation or internal friction, is a function of the distance from the source and the wavelength of the wave, that is, the number of cycles traversed over the distance. Some of the causes of anelastic damping are changes in internal vibrational energy in the molecules, coulomb force (friction) effects on the particles as a result of the physical interaction, viscous damping, and mechanical damping during the acceleration of the particles. The energy is dissipated in the form of heat. The form of the expressions in the equations for the anelastic damping factor, Q, varies and the reader should refer to one of the standard texts, for example, Aki and Richards [1980], for details. Generally, a high value of Q connotes low attenuation and vice versa.

23.3.2 Earthquakes

23.3.2.1 Spatial Distribution.
On a worldwide scale, the distribution of earthquakes is not random. The vast majority of earthquakes occur along plate boundaries (Figure 23-12) where relative motions of the plates produce large stress concentrations. The depths of earthquakes range between the surface of the earth and about 700 km. Earthquakes occurring away from consuming plate boundaries (at trans-

form boundaries and at extensional margins) are generally shallow with depths less than 35 km. At subduction zones the whole range of depths can be seen in a distinct pattern. At the trench side of the margin, the depths are shallow, increasing away from the trench and under the overriding plate. The focal depth increases with the depth of penetration of the subducting plate into the asthenosphere.

In California, where almost all major and minor fault zones are well mapped, most earthquakes can be associated with pre-existing fault zones. This is readily explained by the fact that a pre-existing fault represents a zone of weakness in the crust where stresses accumulate and lower stress concentrations are required to cause rupturing. In other regions away from major plate boundaries, such as New England or the Central Mississippi River Valley, the patterns of earthquake occurrence are less clear. In these regions the lack of surficial expression of faults due to the thickness of soil and alluvial coverage over bedrock and the lower temporal rate of occurrence of earthquakes tends to produce more diffuse patterns of seismic activity.

23.3.2.2 Measurement.
The size of an earthquake can be described by its epicentral intensity, magnitude, and seismic moment. In modern seismological practice, magnitude is the most commonly reported measurement.

Intensity of shaking is a measure of the damage effects produced by an earthquake at a specific location. The maximum damage usually occurs in the epicentral region and this intensity is assigned to an event for purposes of com-
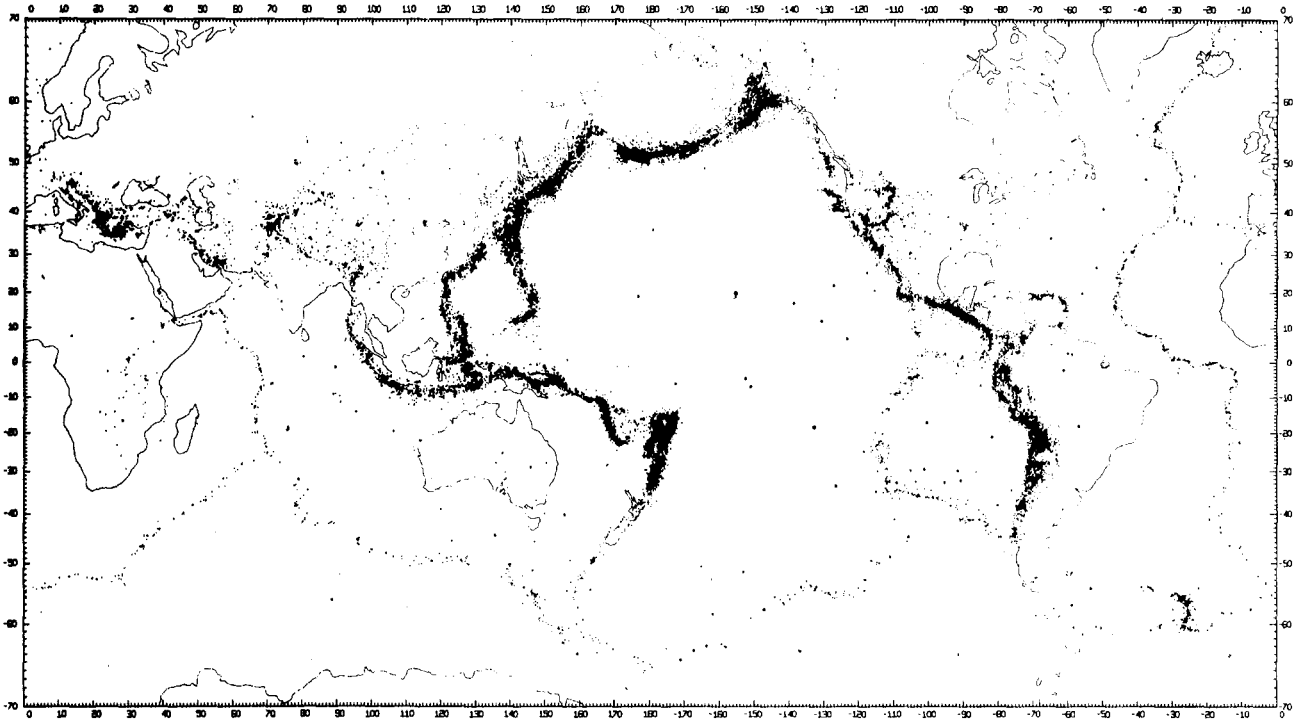
Figure 23-12. Worldwide distribution of epicenters for 1961 through 1967 [Isacks, 1968].

parison. Several intensity scales have been developed; the most commonly used in the United States is the Modified Mercalli Intensity Scale (MMI). Table 23-4 describes the intensities, typically shown as Roman numerals. The MMI ranges from I to XII, with XII being the maximum intensity that can be assigned to an event. While intensity scales have been superseded by more quantitative measures of earthquake size based on instrumental recordings, they are essential in comparing the size of historical earthquakes with modern events. There are few instrumentally recorded events prior to about 1925, but accounts of damage from earthquakes have been published by journals in the past with sufficient detail to assign an intensity and an approximate

epicenter. Magnitude-versus-intensity relationships can be used to construct an earthquake history of an area. Using reports of intensity at different distances from the same event, attenuation of ground motion with distance can be examined. This information is particularly valuable in areas such as Cape Ann, Mass., Charlestown, S.C., and New Madrid, Mo. that have experienced large earthquakes in the past but currently exhibit low seismicity. A drawback of this system is that level of shaking, level of panic, and so forth are subjective. Local damage levels are functions of the size of an earthquake and of several variable factors such as construction quality in the area, geological foundation characteristics, population density, and the scientific

Table 23-4. Modified Mercalli intensity scale of 1931.

I. Not felt except by a very few under specially favorable circumstances. (I Rossi-Forel scale.)

II. Felt only by a few persons at rest, especially on upper floors of buildings. Delicately suspended objects may swing. (I to II Rossi-Forel scale.)

III. Felt quite noticeably indoors, especially on upper floors of buildings, but many people do not recognize it as an earthquake. Standing motorcars may rock slightly. Vibration like passing of truck. Duration estimates. (III Rossi-Forel scale.)

IV. During the day felt indoors by many, outdoors by few. At night some awakened. Dishes, windows, doors disturbed; walls make creaking sound. Sensation like heavy truck striking building. Standing motorcars rocked noticeably. (IV to V Rossi-Forel scale.)

V. Felt by nearly everyone, many awakened. Some dishes, windows, etc., broken; a few instances of cracked plaster; unstable objects overturned. Disturbances of trees, poles, and other tall objects sometimes noticed. Pendulum clocks may stop. (V to VI Rossi-Forel scale.)

VI. Felt by all, many frightened and run outdoors. Some heavy furniture moved; a few instances of fallen plaster or damaged chimneys. Damage slight. (VI to VII Rossi-Forel scale.)

VII. Everybody runs outdoors. Damage negligible in buildings of good design and construction; slight to moderate in well-built ordinary structures; considerable in poorly built or badly

designed structures; some chimneys broken. Noticed by persons driving motorcars. (VIII Rossi-Forel scale.)

VIII. Damage slight in specially designed structures; considerable in ordinary substantial buildings with partial collapse; great in poorly built structures. Panel walls thrown out of frame structures. Fall of chimneys, factory stacks, collumns, monuments, walls. Heavy furniture overturned. Sand and mud ejected in small amounts. Changes in well water. Persons driving motorcars disturbed. (VIII+ to IX− Rossi-Forel scale.)

IX. Damage considerable in specially designed structures; well-designed frame structures thrown out of plumb; great in substantial buildings, with partial collapse. Buildings shifted off foundations. Ground cracked conspicuously. Underground pipes broken. (IX+ Rossi-Forel scale.)

X. Some well-built wooden structures destroyed; most masonry and frame structures destroyed with foundations; ground badly cracked. Rails bent. Landslides considerble from riverbanks and steep slopes. Shifted sand and mud. Water splashed (slopped) over banks. (X Rossi-Forel scale.)

XI. Few, if any, (masonry) structures remain standing. Bridges destroyed. Broad fissues in ground. Underground pipelines completely out of service. Earth slumps and land slips in soft ground. Rails bent greatly.

XII. Damage total. Waves seen on ground surfaces. Lines of sight and level distorted. Objects thrown upward into air.

integrity of the observer. If population is sparse in the epicentral area, reports of the maximum damage may be missing, thus underestimating the size of the event or mislocating the epicenter.

Because of these problems, data used to compile relationships of intensity to quantitative measures of earthquake size such as peak acceleration or magnitude are derived from scattered data sets. A potentially more informative intensity parameter, earthquake felt area, is often computed. It is defined as the area enclosed by a particular "isoseismal" line. These lines are contours of intensity data drawn around an epicenter. Felt area is usually computed to the transition between intensity III to IV or II to III.

The magnitude of an earthquake is calculated from an instrumental measurement of the amplitude of a specified wave packet, such as body waves or surface waves. The general form is $M_x = (\log[A/T]$ or $\log A) + C_p + C_s + C_r$, where M is the magnitude, x is the subscript that identifies the type of magnitude, A is amplitude, T is the period of the waves (equal to approximately 1 s for body waves, 20 s for surface waves), C_p is the correction factor whereby stations at all distances theoretically calculate the same magnitude for an event (a function of the depth of the event and the epicentral distance to the event from the station), C_s is a correction factor for local conditions and C_r encompasses regional correction factors allowing for effects of recording site, wave path, and focal mechanism [Willmore, 1979]. As can be seen from the above representation, earthquake magnitude is a logarithmic scale so that a change of one unit of magnitude roughly represents a change of a factor of 10 in actual ground motion.

The concept of magnitude was developed by Richter in the 1930's for California earthquakes and has been expanded for other areas and different wave packets by Richter and many others. Among the most common magnitudes used today are local magnitude (M_L), the original scale proposed by Richter (M), teleseismic body wave magnitude (m_b), and surface wave magnitude (M_S).

Due to many factors, the magnitude determined for each scale usually will not be identical for a given earthquake. The shape of the seismic wave spectrum is generally flat up to some "corner frequency" after which the amplitude decays. The level of the flat portion is a function of the size of an earthquake: generally the larger the earthquake, the larger the amplitude of the spectrum at a given frequency. This is why m_b and M_s magnitudes, which are measures of the amplitudes at specific frequencies, are used to measure size. However, the corner frequency moves to lower frequencies and longer periods as the size of the earthquake increases. Thus the relationships between magnitude scales, besides being almost completely empirical, are often nonlinear. Mathematically, there is no upper limit to the earthquake magnitude scale; however, because of this shift in corner frequency, the size of an earthquake can get increasingly larger with a smaller and smaller increase in M_s as discussed by Chinnery [1975]. This effect is called satu-

ration of the magnitude scale. The highest magnitude ever evaluated is $8.9M_s$ for an event near Japan on 2 March 1933. This event approached the theoretical maximum magnitude based on the strengths of rocks. On the lower end of the scale, the sensitivity of the instruments and the distance from the event are the only limiting values with negative magnitudes being determined for some events detected at very close range. Approximate relationships between these scales have been determined by several authors [for example, Nuttli, 1979; Bath, 1973]. Examples of such empirical relationships are $m_b = 1.7 + 0.8M_L - 0.01 M_L^2$ and $m_b = 0.56M_s + 2.9$.

Local magnitude is strictly defined only for California, or places with very similar attenuation characteristics, while the body wave and surface wave magnitudes are applied on a worldwide basis. A common mistake found in the literature, especially in engineering studies, is to combine all magnitudes or to simply assume they are all the same. Such a practice, as indicated by the relationships above, can completely invalidate the study. Even though some reports and agencies may simply quote "Magnitude" or "Richter Magnitude", care should be taken to understand how the magnitude was calculated. Richter magnitude often means "M_L" up to M = 6.0 and "M_S" above M = 6.0. Improper discrimination of magnitude types causes major problems in communication and comparison of data, for example the estimation of maximum credible earthquakes in specific regions.

Relationships between magnitude and intensity have also been developed and these functions have strong regional dependencies [Brazee, 1976]. For the Western United States, the relation between maximum intensity, I_o, and body wave magnitude is $m_b = 2.886 + 0.365I_o$, while for the Central United States the relation is $m_b = 2.607 + 0.341 I_o$. The importance of this regional variation and the difficulties of using intensity scales for determination of earthquake size are demonstrated by comparing the 1906 San Francisco earthquake and the 1811-1812 New Madrid earthquakes [Nuttli, 1973]. The San Francisco earthquake probably had a higher magnitude than any of the New Madrid earthquakes. However, due to regional differences in seismic wave attenuation, the San Francisco earthquake was felt over an area less than one-tenth of that for the largest of the New Madrid series of events. This is the result of lower seismic wave attenuation in the Central and Eastern United States than in California. Attenuation will be discussed further in the section on seismic hazard (Section 23.3.2.5).

The seismic moment (M_o) of an earthquake is defined as the product of the rigidity (μ), the average offset along the fault (D) and the area of the fault (S) [Kanamori, 1977]. It is usually calculated in units of dyne-cm. When these parameters are not directly observed, spectral analysis and speculation must be used. This measurement of earthquake size is closer to describing the physical dimensions of a rupture then other kinds of measures (I_o, MMI, M). Relative to earthquake magnitude, which is systematically calculated

by various international agencies such as the International Seismological Centre in Edinburg, only a handful of moments, mostly for larger events, have been determined. A new type of magnitude based on the strain energy drop (the moment) has been computed for some events. It was developed by Kanamori [1977] and is defined by log $W_o = 1.5M_w + 11.8$ where W_o is the minimum strain energy drop and M_w is the moment magnitude. This magnitude scale circumvents the problem of saturation of M_s that was discussed earlier in this section. The great Chilean earthquake had an M_w of 9.5 but an M_s of only 8.3.

There are numerous magnitude scales developed for use with events too small to be recorded teleseismically (definitions of this term vary; here 1000 km is considered the cutoff distance). Measurement of such events presents a problem because the recordings are heavily influenced by the path through the crust.

### 23.3.2.3 Focal Mechanisms and Fault Plane Solutions.

Another common tool used to understand the nature of earthquakes is the fault plane solution. This is determined quantitatively by a special plot of the polarity of the first motions of seismic waves recorded at all stations where the first motion is readable. Figure 23-13 shows examples of the three main kinds of fault motion: thrust, normal and strike slip. Thrust faulting occurs when two fault blocks are pushed together and the overhanging wall rises over the foot block wall. Normal faulting occurs when blocks are pulled apart (tension) and one block drops down. Strike-slip faulting occurs when two fault blocks slide past each other. The strike of the fault (the angle the fault plane makes with north) and the dip (the angle that the fault plane makes with the surface) are easily read off these plots. There is, however, an ambiguity over which focal plane is the fault plane. This must be resolved either through surficial expressions of the fault or knowledge of the tectonic regime. Figure 23-14a shows how a fault plane solution is constructed for thrust or normal faulting. Basically, it represents a projection of a hemisphere, usually a lower hemisphere, centered about the focus of the earthquake onto a plane. The angles of incidence of the seismic waves leaving the scene of an earthquake to recording stations have been calculated for various distances. Compressional or dilatational waves reaching a station are coded on a plot (solid circles for compressional, open circles for dilatational). Focal planes are drawn dividing compressional and dilatational regions, with the stipulation that the planes are mutually perpendicular. Figure 23-14b shows the rationale for the characteristics of the strike-slip fault plane solution. These faults are often described as "right lateral" or "left lateral". This means that if the ground on the opposite side of a fault from an observer moves to the right, the fault is said to be right lateral; if it moves to the left, left lateral (Figure 23-15). Faults can also exhibit combinations of the motions described in this section.
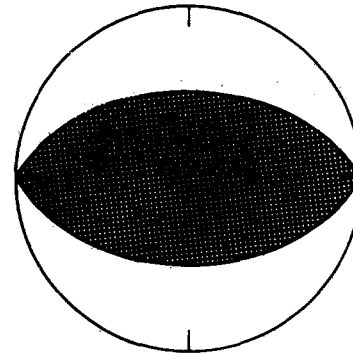
STRIKE=90° DIP=45°

(a) PURE THRUST FAULTING
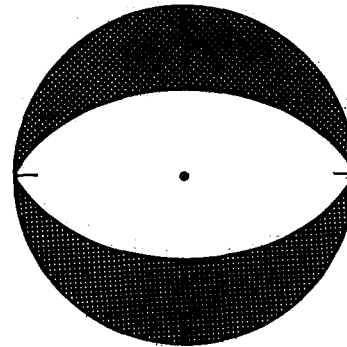
STRIKE=90° DIP=45°

(b) PURE NORMAL FAULTING
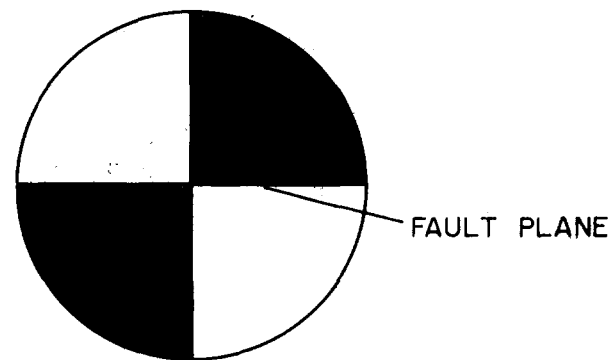
FAULT PLANE

STRIKE 90° DIP=90°

(c) PURE STRIKE-SLIP FAULTING

Figure 23-13. Examples of fault-plane solutions for different types of earthquake mechanisms.

SIDE VIEW OF THRUST FAULT
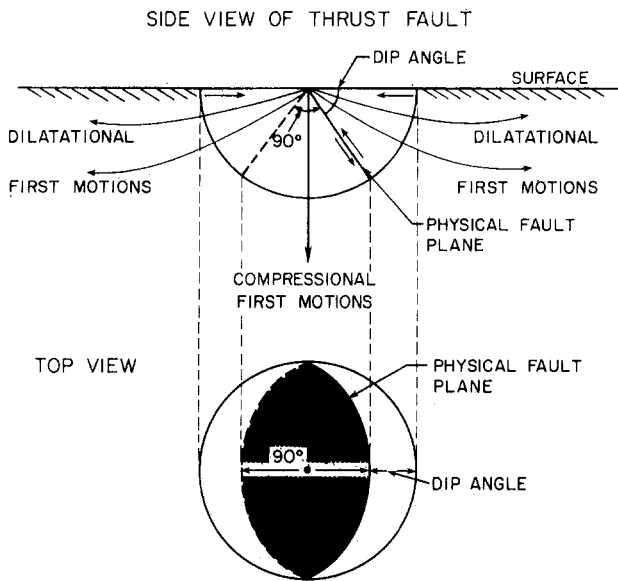

TOP VIEW OF
STRIKE-SLIP FAULT

(a)

TOP VIEW

(b)

Figue 23-14. How to construct a fault-plane solution.
(a) Side and top view of thrust fault plane solution
(b) Top view of strike-slip fault and top view of fault plane solution

23.3.2.4 Temporal Distribution.

The rate of earthquake occurrence has been found to be described approximately by the function $\log N = a - bM$, where N is the number of earthquakes of magnitude M per unit time. For the entire earth from the period 1918 to 1964 the constants of this equation have been found to be a = 8.73 and b = 1.15, where N is the number of events per year based on earthquakes in the range of 6.0 to 8.9M [Bath, 1973]. Recurrence

LEFT LATERAL MOTION
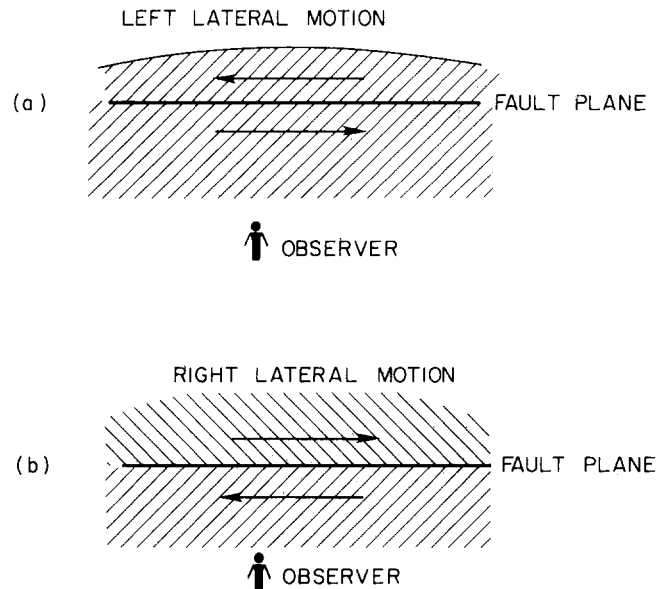

RIGHT LATERAL MOTION

Figure 23-15. Fault motion convention
(a) Observer sees land on opposite side of fault line move to his left.
(b) Observer sees land on opposite side of fault line move to his right.

curves of this form are useful for areas as small as $10^4 km^2$. The slope, or b-value, of the curve is normally found to lie between 0.5 and 1.5. It is not clear whether the variations are caused by scatter or are indicators of the seismic processes in a region. The value of "a" is highly variable, however. Obviously regions of high seismic activity, such as southern California, have higher "a" values than less seismically active regions, such as New England.

23.3.2.5 Hazard Evaluation.

Strong ground motions from earthquakes constitute a great threat to facilities near the causative fault. Earthquakes capable of producing strong ground motions have been recorded in almost every state of the United States (Figure 23-16). Two approaches have been developed by seismologists to estimate potential strong ground motion levels at particular sites. The deterministic method attempts to predict the maximum ground motion possible while the probabilistic approach predicts the likelihood that a given ground motion will occur over some specified period of time. The two methods need not be mutually independent. The most physically realistic model would ideally incorporate elements common to both.

The deterministic approach to seismic hazard evaluation requires a knowledge of faults in the vicinity (radius of 100 km or more) of the facility. In general, faults that have shown any activity during the Quaternary (past two million years) are considered capable of sustaining seismic activity. An estimate is made of the maximum length of each fault that could rupture in one earthquake and this value is used
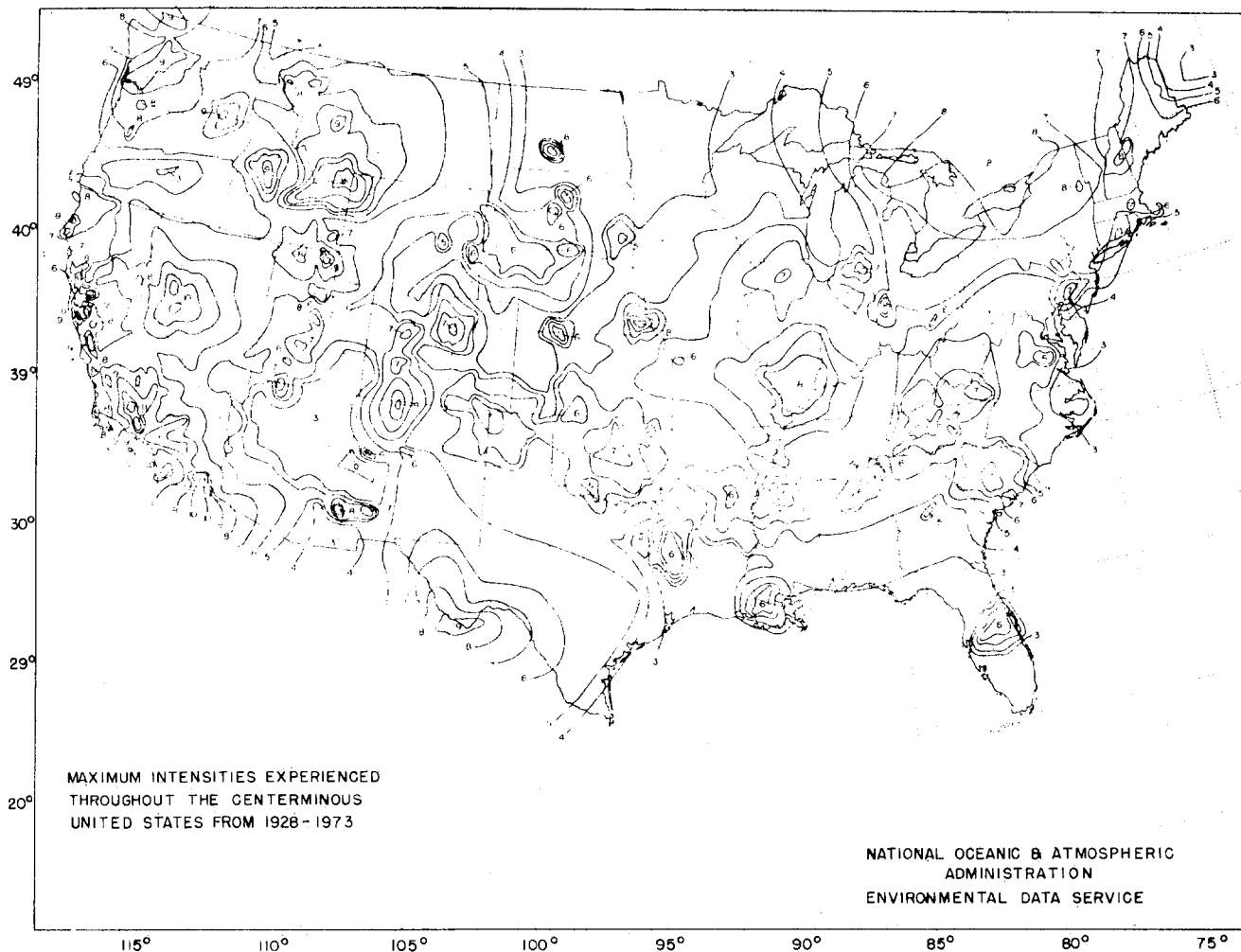
Figure 23-16. Maximum earthquake intensities throughout the United States from 1928 to 1973 [Brazee, 1976].

to evaluate a maximum credible earthquake, that is, the largest earthquake with a reasonable chance of occurring on the given fault. The evaluation is done using any of several empirical equations relating magnitude to maximum fault rupture length [Slemmons, 1977]. One equation of this form is $M_L = 5.4 + 1.4 \log L$, $\sigma = 0.26$, where L is the length of the fault in kilometers [Greensfelder, 1974]. This phase of the deterministic approach, estimating the maximum possible earthquake, is the most difficult. Often the length of the fault is unknown and estimates of magnitude of past events from geological examination of fault offsets do not always yield unique values. When the estimation is made, strong ground motions at a site can then be evaluated using empirical relations between magnitude, distance, acceleration, velocity, or displacement. A compilation of various relationships can be found in McGuire [1976]. Caution must be used however in selecting a set of equations since they are not all valid worldwide; some were developed for specific areas, such as California. One set of equations of this type is

$$\ln a_s = 6.16 + 0.645M_L - 1.3(R+25)$$

$$\ln v_s = 1.63 - 0.921M_L - 1.2(R+25)$$

$$\ln d_s = 0.393 + 0.99M_L - 0.88(R+25),$$

where a_s, v_s and d_s are the site acceleration, velocity, and displacement, M_L is the event magnitude, and R is the distance from the fault to the site in kilometers. Note that these equations are valid only for rock sites in the western United States. A modified acceleration function for the central United States is given by Battis [1981]: $\ln a_s = 3.155 + 1.240m_b - 1.244 \ln(R + 25)$. Further modification of these equations is required to compensate for local site conditions, but these methods are beyond the scope of this review.

One problem with a purely deterministic approach is that the return period of the maximum event may be so large that it is unreasonable logistically and financially to design a relatively short lived facility to a very high value. For

23-16

example, if a magnitude 7.0 event had a return period of 100 000 years, the annual rate of occurrence would be 1×10^{-5}. If the life of the structure in question is 40 years, then the probability of exceeding a magnitude 7 during the lifetime of the structure would be approximately 4×10^{-4}. At this point the probabilistic approach should be utilized.

Another problem is that these relationships for acceleration do not predict the level of ground motion over the entire frequency range. Standardized spectra have been developed (Nuclear Regulatory Guide 1.60) which can be anchored at a peak acceleration value. As yet, modification of the shape of the spectra for the type of soil at the site and for the magnitude of the event is not a routine process [Johnston et al., 1980].

The method of using seismic hazard estimates to design structures has gained acceptance in recent years. A computer program by McGuire [1976] that will perform the necessary calculations has been made available to the public. Since the concepts and assumptions that make up the calculation must be understood in order to assess the appropriate use and the limitations of the method, a brief overview is presented. Once the site of interest has been selected, a catalogue of earthquakes in terms of date, location, and size (magnitude or intensity) is examined. If the catalogue is not homogeneous, then conversions from one magnitude scale to another (for example m_b to M_s) or from intensity to magnitude must be made. Care must be taken to select the proper conversion relationship (Section 23.3.3). A range of scenarios are tried, using source zones of various sizes, to model the seismicity (Figure 23-17a).

Once source zones are defined, the enclosed seismicity is tabulated. Earthquakes are counted according to magnitude, or any other measure of size and time interval. The seismologist decides on the appropriate time intervals using judgements of the completeness of the catalogue for various years for the different magnitude ranges. A recurrence curve is derived for each source zone (Figure 23-17b). These curves represent the modeled cumulative number of earthquakes that will occur in a given source zone at any magnitude (per year if the calculations are for annual risk). Next, all the modeled seismicity that occurs annually in this zone is distributed evenly throughout the zone according to location. Even if the natural occurring seismicity is clustered in a small area within the zone, it will be spread out uniformly. This is an important detail because of the distance calculation (Figure 23-17c). Therefore, the geometry of the zones plays an important part. The next step requires an attenuation relationship that relates magnitude to acceleration, velocity, or displacement and distance to the site (Figure 23-17d). Distances are then computed to the seismicity which is now distributed evenly in the zone. When all this has been tabulated, the result is Figure 23-17e, the annual risk of exceeding the ground motion parameter used in the figure.
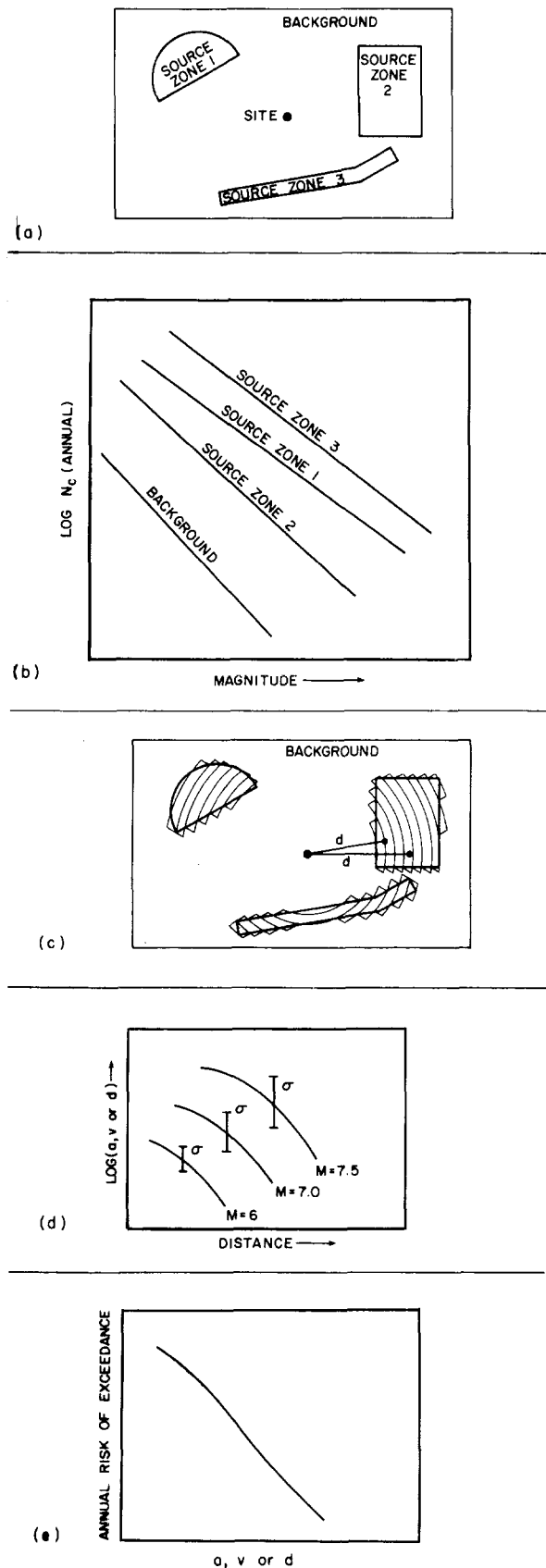
This type of analysis is probably most useful for com-

(a)

(b)

(c)

(d)

(e)

Figure 23-17. Performance of seismic hazard calculation.

23-17

parison purposes: performing this calculation for two distinct sites that have a fairly accurate earthquake catalog will yield a good estimate of the relative seismic hazard of the two regions. Since there are some elements of the deterministic approach incorporated into the hazard, such as choosing the source zone boundaries and an event upper magnitude cutoff, this method gives more information about the actual hazard to a facility during its useful lifetime (typically 30 to 50 years). It also allows designers or regulating agencies to quantitatively incorporate conservatism into the design or to set guidelines. Often a 10 000 year return period is considered to be an acceptable hazard. The actual probability of damage to a stucture using seismic hazard and engineering methods is called the seismic risk.

Another limitation of the hazard method is that it does not include the duration of the ground motion contributing to the annual risk. Seismic waves from a magnitude 7.0 earthquake at 100 km distance may, for example, have higher amplitude ground motion and longer time duration at periods greater than approximately 0.8 s than will a magnitude 5.5 which is located within 10 km of the site. Since structures respond to periodic signals more readily than to a single spike of motion and have specific natural frequencies, these complications should be considered.

The maximum credible earthquake may have a much longer return period than the useful life of most structures. Probabilistic methods are generally considered to provide more realistic estimates of the ground motions and may be more useful in the case of life-line structures or structures such as nuclear reactor facilities whose failure would produce a significant threat.

Several methods have been devised to provide regionalized seismic hazard maps for the United States. The results of two of these studies are shown in Figures 23-18, 23-19, and 23-20 [Algermission, 1969; Donovan et al., 1977]. Figure 23-18 is the result of a deterministic approach while Figures 23-19 and 23-20 result from probabilistic methods.
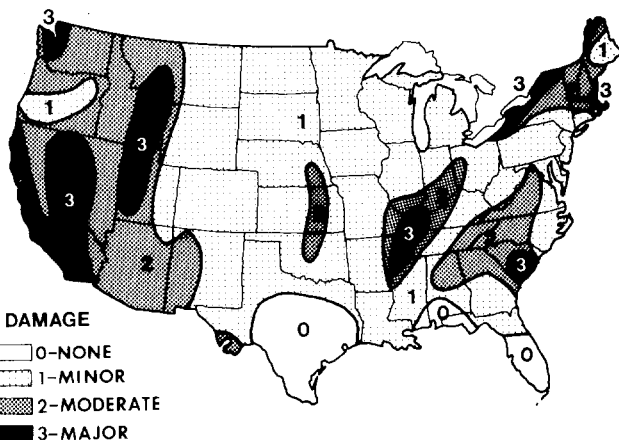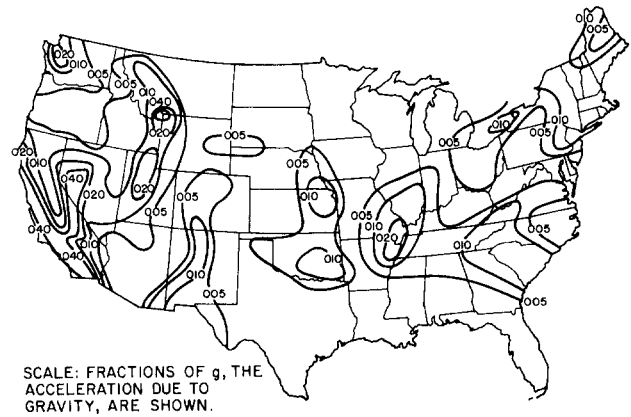

Figure 23-19. Contours of peak accelerations due to earthquakes at the 90% confidence level for any 50-yr period [Donovan et al., 1977]. Reprinted with permission from *Technology Review*, © 1977.

23.3.2.6 Premonitory Phenomena. In recent years earthquake prediction has become one of the major areas of study in seismology. The basic premise of prediction is that as stresses accumulate in the crust, physical properties of the rock will change and these changes are detectable. Compression of rock along the future earthquake rupture zone is expected to produce changes in porosity, electrical resistivity, seismic velocities, water table levels, and the radon content of ground water. Tilt and elevation changes may also be indicators of future significant events. Each of these phenomena are detectable by various means. For short term prediction, abnormal animal behavior has been associated with seismic events. In addition, the spatial and temporal distribution of low magnitude earthquakes is thought to be altered by stress accumulation and provides an indication of an imminent large earthquake. To date, significant advances have been made in earthquake prediction with at least one significant major prediction (4 Feb 1975, Liaoning

Figure 23-18. Seismic hazard zonation of the United States based on deterministic methods [Algermissen, 1969].
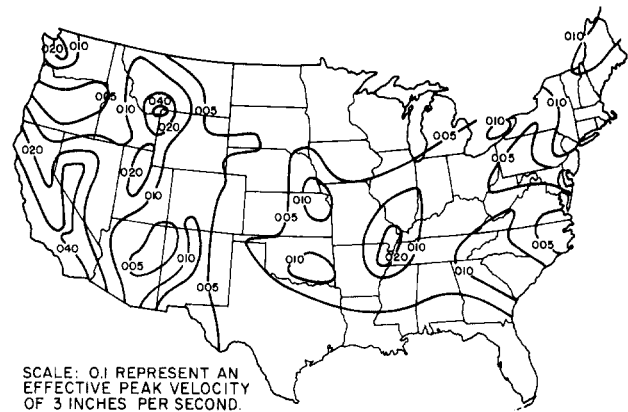

Figure 23-20. Contours of maximum peak velocity due to earthquakes at the 90% confidence level for any 50-yr period [Donovan et al., 1977]. Reprinted with permission from *Technology Review*, © 1977.

Province, China, 7.3 M_L) possibly saving thousands of lives. However, prediction is more complex than it first appeared to be. Many of the phenomena which are believed to precede an earthquake have been detected without the occurrence of an earthquake. Methods used to predict an earthquake at one place in the world do not always work at another time or location. At the present time, earthquake prediction is not an exact science and will require more time and research to achieve routine practical application.

23.3.3 Other Sources of Seismic Radiation

23.3.3.1 Seismic Noise. A seismometer placed anywhere on the surface of the earth will record virtually continuous earth motions of variable intensity. This seismic background noise is known as microseisms. Typically, the generation of microseisms is the result of cultural, meteorologic, and oceanographic conditions and is unrelated to tectonic processes responsible for earthquakes. Worldwide, the documented sources of microseisms appear to be surf or other near-shore action along steep coast lines and cyclonic activity over deep water [Bath, 1973]. More localized sources include traffic, heavy machinery, rivers, and wind-induced motion in buildings or trees. At any given site, seismic noise can be classified into three frequency dependent branches.

1. Microseisms having periods of less than 2 s are generally caused by local sources. Maximum amplitudes usually occur near 1 Hz and are rapidly attenuated away from the source [Ossing and Gray, 1978]. The localized nature of generation makes the amplitudes of these microseisms highly site dependent. These sources can normally be readily identified as cultural in origin.

2. Between 2 and 10 s lie the storm microseisms. In this band, the occurrence of high level activity has been strongly correlated with deep low pressure areas and frontal passages impinging on continental margins. The nature of the storm microseismic source suggests two facts: first, the intensity of storm microseisms are significantly higher during the winter, and second, coastal sites are affected to a much greater degree than sites in the continental interiors. The mode of propagation approaches the Rayleigh surface wave mode traveling at a velocity of 2.7 km/s [Iyer, 1964]. Amplitude attenuation is low for propagation through uniform geologic structures but is greatly increased at discontinuities such as continental margins or mountain boundaries [Ossing and Gray, 1978].

3. The long period microseisms, greater than 10 s, peak at approximately 20 to 25 s. This peak is associated with microseisms generated by the coupling of the ocean floor with cyclonic induced ocean waves over deep water. Attempts to track tropical cyclones using these microseisms have met with varying success [Bullen, 1965]. A pronounced minimum in the noise spectrum is also noted for periods between 30 and 40 s. This minimum appears to be

global in character and exhibits stable spatial and temporal characteristics.

Brune and Oliver [1959] have derived minimum, average and maximum displacement amplitude curves for non-local seismic noise levels in the period range of 0.1 to 31.5 s. These curves, converted to amplitude spectral density, are shown in Figure 23-21 and represent limiting values of the microseism spectrum. The actual spectrum calculated for any given site over a short time interval would be expected to lie between the minimum and maximum curves but they might have a significantly different shape than the plotted curves. For example, the depicted 8-s storm microseism peak could vary between a 4 and 10 s period.
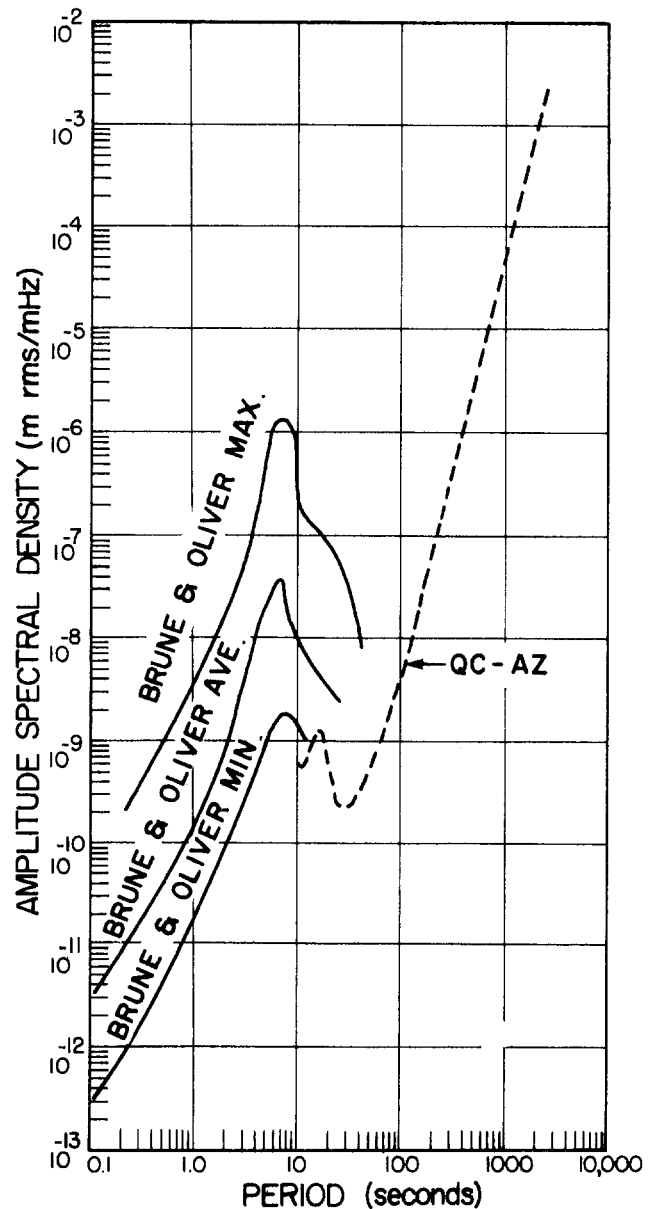

Figure 23-21. Amplitude spectral density of seismic noise from 10 to 2560 s period [compiled from Brune & Oliver, 1959 and Fix, 1972].
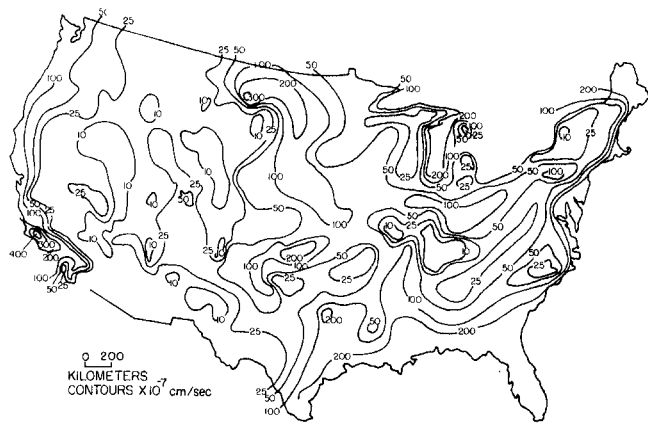
Figure 23-22. Contour map of seismic noise levels in the United States in terms of particle velocity [Ossing and Gray, 1978].

Also plotted in Figure 23-21 is the seismic noise amplitude spectral density for data recorded at a quiet site (Queen Creek, Arizona) for periods between 10 and 2560 s [Fix, 1972]. Particular care was taken in the installation of this station to minimize all locally induced noises. It is thought that this spectrum is a good representation of the minimum noise levels in this period range.

The seismic noise level observed at any site is also a function of geographic location. The proximity to coastlines

and population, the type of vegetation and local geologic structure will all influence noise levels. In Figures 23-22 and 23-23, contour maps of average seismic background noise levels for displacements and particle velocities near 1 Hz in the continental United States are shown [Ossing and Gray, 1978].

23.3.3.2 Other Sources of Seismic Radiation. While earthquakes (and volcanoes to some extent) are the most prominent natural source of destructive seismic radiation, many other sources are of interest for different reasons. Some of these sources are nuclear and chemical explosions, air coupled seismic waves generated by aircraft acoustic energy (especially low-flying aircraft such as the cruise missile) or atmospheric explosions, vibrating machinery, rockbursts (collapsing mines), cryoseisms (ice fracturing), moving vehicles (trucks or landing airplanes), and people. Following are some examples of how these sources affect life on earth.

Large chemical or nuclear explosions generate significant motions which must be considered in many military construction projects. Away from the source region where cratering and other source particular effects must be considered, these motions can often be treated like earthquake generated motion. Differences in the characteristics of explosions and earthquakes, however, also allow the seismologist to provide information on the detection and dis-
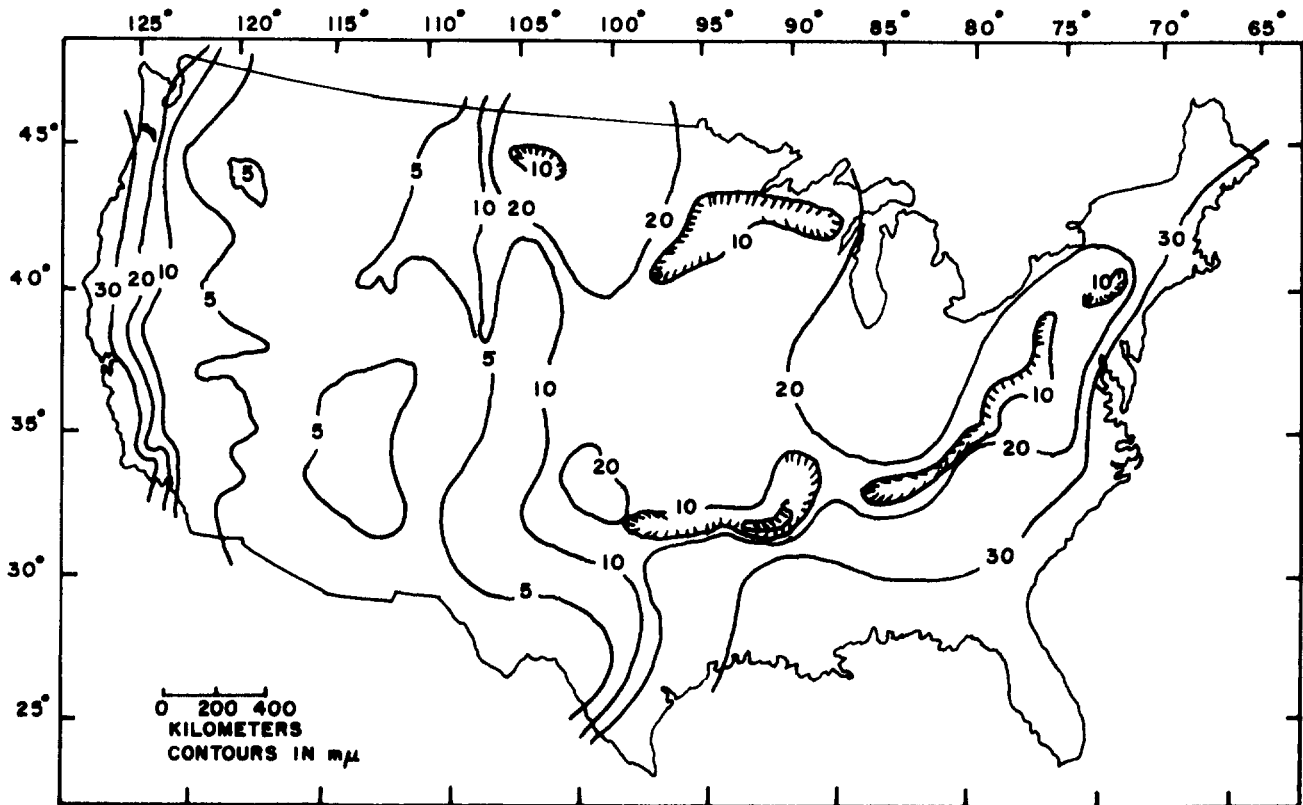

Figure 23-23. Contour map of average background noise displacements in the United States [Ossing and Gray, 1978].

crimination of nuclear explosions for the purpose of test ban treaty verification. In the siting of motion sensitive instruments, local disturbances caused by any source should be considered, especially where large concrete structures are constructed. Vibrations caused by even small quarry blasts during the critical curing period can prevent the proper cohesion from developing.

The fact that moving vehicles and personnel produce seismic signals has been used to develop security systems and methods of remote battlefield sensing. Pressure waves generated by military aircraft can, under certain conditions, couple with the ground to produce large amplitude seismic motions which could affect ground facilities or be used to track the aircraft.

The study of seismic sources in the high frequency regime has almost unlimited practical applications in geologic exploration, nuclear detection, and earthquake prediction.

23.4 LONG PERIOD AND SECULAR EARTH MOTIONS

This section briefly treats measurement of crustal motion and puts some bounds on the magnitude of such deformations and the accuracy of the observations. Some of the most important techniques used are from the field of geodesy, which is reviewed in Chapter 24. In the first subsection, details of the motions caused by tectonic processes, which were reviewed in Section 23.2 will be examined; in the second, the earth tides; and in the third, other more localized types of motions, which often form the noise background and hinder the performance of instruments and systems. Specifically excluded from consideration are various geological processes, such as soil creep, landslides, glaciological activity, and volcanic activity, all of which can exhibit substantial motions.

23.4.1 Tectonic Motions

We know from geological and paleomagnetic studies that portions of the earth have moved, at least in a relative sense, thousands of kilometers horizontally and tens of kilometers vertically (the top of Mt. Everest is marine limestone). We also have found from such studies that these movement velocities are not constant but are discontinuous, episodic, or even cyclical. One of the main challenges in solid earth geophysics is to directly measure such motions, relate them to the past rates determined geologically or paleomagnetically, and develop empirical or physical models to predict future motions. These goals are not without practical application, for the most dramatic form of tectonic motion is the sudden release of accumulated strain during major earthquakes with the concurrent generation of potentially destructive seismic waves. Volcanoes, which are an-

other manifestation of tectonic processes, are capable of producing large, if localized, motion.

Recent tectonic theory has given the broad picture of relative motions between rigid plates, but the details are considerably blurred for several reasons. First, the plate boundaries are not simple discontinuities but are generally zones up to 100 km or more in width where strain can accumulate. A second problem is that plate tectonics does not explain crustal motions in plate interiors. Another problem of a different nature is the proclivity of many investigators to discover "micro-plates". Then, of course, there are large-scale secular motions that have no direct relationship to plate tectonics, for example, the mid-continental downwarps associated with deposition in sedimentary basins.

23.4.1.1 Horizontal Motions. Almost all earthquakes that cause observable surface displacements are associated with faults or fault zones. Coseismic fault displacements range from negligible for small earthquakes, to several centimeters for magnitude 5, to several meters over hundreds of kilometers for magnitude 9 shocks. The maximum total displacement for the great Alaskan earthquake of 1964 was over 25 m. The ratio of displacement to fault length ranges from 10^{-4} to 10^{-6}. Well-defined, natural or artificial (planned or fortuitous) linear or planar features (for example, fences, alignment arrays, stream channels, or shorelines) crossing the fault can be used to determine the offset. Repeated geodetic surveys (Chapter 24) are also made to determine both earthquake displacements and accumulation of strain. The U.S. Geological Survey runs an active deformation monitoring program in California, using laser geodimeters to measure the distances among benchmarks in several geodetic networks [Savage et al., 1981]. The formal errors (standard deviations) in these surveys are between 10^{-6} and 10^{-7} for lines between 20 and 50 km long. Most of the error is attributable to variations of the index of refraction along the line of sight. The strain accumulation rate in the San Andreas fault zone is about 0.3×10^{-6}/yr, or where the motion is creep on the faults themselves with little or no strain buildup, about 3-5cm/yr. Thus the expected line length changes are of the order of the present day survey accuracy and several years must elapse between surveys before reliable results can be obtained. Since several crustal plates converge in Japan, the deformation rate is high and the motion pattern complex [Mogi, 1981]. Similar programs are in progress in Turkey, India, New Zealand, the USSR, Central America, Alaska, Canada, and many others. See Simpson and Richards [1981] for examples.

23.4.1.2 Vertical Displacements. Secular vertical crustal motions rarely exceed 1 mm/yr. Some exceptions are Japan (7 mm/yr in some regions), where tectonic activity is high, the Hudson Bay region (10 mm/yr), which is still responding to the removal of the continental ice sheet 10 000 years ago, and several other, usually local, areas.
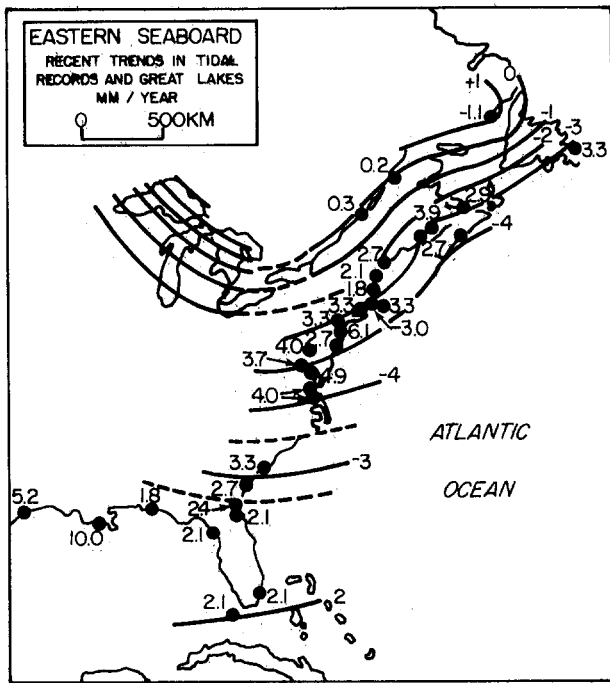
Figure 23-24. Recent trends in tidal gages [Anderson, et al., 1978].

See Figure 23-24 and Walcott [1972]. Thrust and normal faulting during earthquakes generally produce relative vertical displacements of less than 5 m, except for the very largest tremors. Classically, vertical movements have been measured by repeated spirit leveling (Chapter 24), a simple surveying procedure that has been more or less routine for the past 100 years in which errors accumulate as some function of line length. An examination of leveling surveys by Castle et al. [1976] revealed that a broad area of crustal upwarp of up to 25 cm had occurred between 1960 and 1974 in southern California. This aseismic uplift was soon christened the "Palmdale Bulge" for a small town 50 km north of Los Angeles near the zone of maximum uplift. Additional surveys over the past decade showed that not only was the bulge much larger than previously expected, extending over most of the Mojave Desert region, but also that there had been a partial collapse since 1974. Theoreticians and modelers were puzzled because of the lack of seismicity and the difficulty of fitting the bulge into the known horizontal movements of the region. At this point, Jackson and Lee [1979] questioned the very existence of the bulge, attributing it to systematic rod calibration and atmospheric refraction errors that can accumulate over large elevation changes, such as those occurring between Los Angeles and Palmdale. After a heated debate, tests by National Geodetic Survey (NGS) [Strange, 1981], and refutation by the U.S Geological Survey [Stein, 1981], a good portion of the Palmdale Bulge has disappeared. Furthermore, many other surveys that suggested recent vertical movements were found to be contaminated by these topo-

graphically correlated errors [Reilinger and Brown, 1981]. This can be seen in a paper by Brown [1978] where surveys along the east coast of the U.S. suggest substantial local movement, but the tide gauges along the coast do not. Incidentally, new survey procedures published by the NGS should eliminate these errors by tightening rod calibration standards and reducing sight lengths.

23.4.1.3 Measurement Techniques.
Tide gauges have long been used to estimate vertical movements (Figure 23-24). However, depending on the record length there are some problems which include long-period tides, climatic and seasonal effects (pressure and temperature), meteorological effects (wind), river discharge variations, local site stability, instrumentation, and eustatic (world-wide) sea level changes [Anderson, 1978]. It appears that sea level is probably rising at a rate of less than 1 mm/yr, although it apparently rose about 6 m in the last 18 000 years. The release of water stored as ice in the great continental ice sheets is accommodated to a great extent by the deflection of the crust under the redistributed.load [Walcott, 1972].

Another method often used to infer elevation changes is repeated gravimeter surveys. After corrections for earth tides (Section 23.4.2) and atmospheric pressure variations, temporal changes of gravity can occur from either (1) displacement of the observation point along the free-air gravity gradient (-3.086 μgal/cm, $\pm 5\%$ typically), or (2) variations in the subsurface density field (for example, 0.43σ μgal/cm for an extended sheet of material with density contrast σ). These two factors generally interact, constructively or destructively, depending on the process operating. Usually this is not known, so a model must be assumed. For example, a section of material subjected to horizontal elastic compression would bulge upward, thus reducing the gravity in accord with (1) above; however, the increase in density, effect (2), would cancel this almost exactly, resulting in no net change of gravity. Whitcomb [1976] presents a number of models and the corresponding gravity and elevation changes. Measurement of both could strongly constrain such models.

Aside from the fact that some tectonic phenomena produce elevation but little or no gravity change, detection requires careful measurement and removal of spurious effects as well as the variations caused by the solid earth and ocean tides (Section 23.4.2). Lambert and Liard [1981] recently assessed their accuracy of measurement in a strongly interconnected gravity network established with La Coste and Romberg "D" gravimeters, the best instrument currently available. They estimated that with very careful work, the conservative long-term accuracy of a single station after least-squares adjustment of the network is about 4 μgal, which corresponds to a free-air elevation change of about 1 cm. Everndon [1981] found a relative accuracy (RMS) of about 20 μgal for stations along profiles in southern California. A major contributor to changes in gravity is the

movement of groundwater. For example, water filling the intergranular voids of a 1 m thick sandstone with 10% porosity would cause a gravity increase of 4.3 μgal. Lambert and Beaumont [1977] found seasonal gravity changes as high as 12 μgal due to fluctuations in ground water level. In locales where the geohydrology is simple and wells are plentiful it is perhaps possible to correct for such effects, but in complex regions such as those with many aquifers or with strong lateral heterogeneity, ground water changes strongly limit this technique. Variations in the elevation of the water surface in reservoirs, rivers, lakes, and seas also cause gravity variations at nearby stations. These can usually be easily calculated if the phenomena are adequately monitored.

Despite the problems and ambiguities associated with gravity surveys, there are two distinct advantages over leveling. First, it is much easier to make spot measurements over a wide area. Second, gravity survey errors propagate as a function of time rather than with distance, so given the proper logistical support, better precision at distant points could be achieved.

Repeated Very Long Baseline Interferometry (VLBI) measurements using satellites as sources, apparently have the precision ($< \pm 10$ cm over 5000$^+$ km lines) to detect relative plate motions. With expected improvements, the formal error for repeated observations should drop to about ± 5 cm or better for the horizontal components. The precision of the vertical component is typically twice that be-

cause of the observing geometry. Table 23-5, derived from Minster and Jordan [1978] shows expected plate velocities among the existing VLBI radio observatories. Thus, for example, to detect the 2 cm/yr separation between Europe and North America, caused by sea floor spreading at the Mid-Atlantic Ridge at the 95% confidence level, would require several years between two measurements. In practice, the precision can be improved by numerous repeated observations. The major limitation to VLBI measurements is the presence of water vapor in the atmosphere. At a 20° elevation angle the correction is 30$^+$ cm. With only surface measurement of water vapor the uncertainty would be about 5 cm. Radiometers are being developed to make such corrections.

Satellite laser ranging from a number of ground stations to an orbiting vehicle equipped with retroreflectors has proved sufficiently precise to measure crustal displacements of several centimeters over 10^2 to 10^3 km. This technique was used for the San Andreas Fault Experiment (SAFE) to determine the relative velocity between the North American and Pacific plates [Smith et al., 1979]. The average velocity, determined from measurements taken in 1972, 1974, 1976, and 1979, was 9 ± 3 cm/yr, which is considerably greater than the Minster and Jordan [1978] value of 5-6 cm/yr and even greater than the observed creep or strain (equivalent to 2-3 cm/yr) in the fault zone. This could be due to the fact that the plate model has a time resolution of no better than 10 000 years and that the present motion is greater

Table 23-5. Interplate velocities (cm/jr) for proposed VLBI baselines.

From:	Onsala (Sweden)	Effelsberg (W. Germany)	Kashima (Japan)	Brazil	Hawaii	Kwajalein	Arecibo (Puerto Rico)
To:	NORTH AMERICAN PLATE						
Haystack, Mass.	+1.7	+1.9	−0.4	−0.2	+0.8	+0.5	+0.4
NRAO, (W Va.)	+1.7	+1.9	−0.5	−0.4	+1.5	+1.2	+0.4
Ft. Davis (Tex.)	+1.5	+1.6	−0.8	−0.7	+3.1	+2.8	+1.7
OVRO (Calif.)	+1.4	+1.5	−0.9	−0.6	+1.6	+2.3	+1.5
Alaska	+1.0	+1.1	−0.7	−0.2	−5.2	−2.3	N/A
Algonquin (Canada)	+1.7	+1.9	−0.5	−0.3	+0.4	+0.4	+0.6
To:	PACIFIC PLATE						
Hawaii	−2.7	−2.0	−8.7	+3.5	—	—	N/A
Kwajalein	−4.0	−3.6	−9.4	+2.4	—	—	N/A
To:	EURASIAN PLATE						
Onsala	—	—	—	+1.1	−2.7	−4.0	N/A
Effelsberg	—	—	—	+1.3	−2.0	−3.6	N/A
Kashima	—	—	—	−0.1	−8.7	−9.4	N/A
To:	SOUTH AMERICAN PLATE						
Brazil	+1.1	+1.3	−0.1	—	+3.5	+2.4	−1.3
To:	CARIBBEAN PLATE						
Arecibo	−0.6	−0.6	N/A	−1.3	N/A	N/A	—

than that average, or that slip between the plates is distributed over a much wider area than the San Andreas fault zone, possibly including the Basic-Range province of Nevada and Utah.

A third space-based system that has been proposed is a space-based laser ranging system [Smith, 1978]. In this concept, the laser would be placed in a circular orbit at 1000 km altitude at a 50° inclination to the equator. The spacecraft would be programmed to range to large numbers of retroreflectors placed on monuments in areas of interest. Simulations show that intersite distances of 20 to 200 km can be repeated to better than ± 1 cm. The space-based laser ranging system has an advantage over VLBI techniques in that atmospheric corrections are small at optical wavelengths.

Continuous or high-frequency measurements of crustal deformation are made with tiltmeters, strainmeters, and multiwavelength ranging devices. These are reviewed thoroughly elsewhere [Committees on Geodesy and Seismology, 1981] so will be mentioned only briefly. Long (750 m) laser strainmeters (interferometers) installed on the ground surface have been operated successfully for a number of years in southern California [Berger and Lovberg, 1970]. Pendulum-type tiltmeters have been used to infer long-period crustal motions, but their short baselengths make them susceptable to very small reference point instabilities from which even long-base line instruments are not entirely free. Deep borehole tiltmeters have shown more stability than those installed at shallow depths because of greater isolation from near-surface effects, but agreement among closely-spaced instruments has not been good. Long fluid tiltmeters, from which tilt is inferred from changes in the height of a liquid a known distance apart, promise greater stability by averaging out short wavelength spatial noise [Wyatt et al., 1982]. Laser surveying instruments operating at two wavelengths can correct for variations in atmospheric refraction because of dispersion effects. Operated with a third (microwave) frequency to correct for water vapor content, accuracies of a few parts in 10^8 are possible. One of these has been operated on a continual basis, ranging to a number of targets, near Hollister, California [Huggett et al., 1977].

Rapid advances are being made on both measuring and understanding earth motions. Although problems discussed in Section 23.3.3 are a limitation, long-base instruments and space techniques show great promise in producing increasingly accurate observations of crustal deformation [Committees on Geodesy and Seismology, 1981].

23.4.2 Earth Tides

Historically, it was thought that a study of the solid earth's response to the tidal effects of the sun and moon would shed important light on global mechanical properties and the rate of tidal energy dissipation. Over the past ten

years a number of perturbations, which cannot be adequately modeled, have rendered this goal futile. Much better models can be constructed from higher-frequency seismic data, and earth tidal effect over a wide range of these is only 1%–2% at most. Distinguishing among these is almost certainly not within the province of tidal measurements.

However, there have been rapid advances in theory, instrumentation, and techniques, many occurring within the past ten years that make the subject a fruitful field for research. In addition, there have been and still are practical reasons for tidal studies. A list, a very brief commentary, and references, follows. For many of these, the relative accuracy must be of the order of 1%.

1. Earth tide measurement can be used to help constrain ocean tidal models using shore-based gravity and tilt measurements [Kuo, 1978; Baker, 1978].

2. Baker [1978] has shown that the response to tidal loading is primarily due to the spatially averaged Young's modulus rather than density and Poisson's ratio, which are the primary parameters in seismic wave propagation. Thus tidal measurements can provide important supplementary information in elucidating crust and upper mantle structure.

3. The tidal admittances can be predicted initially from theory, or at worst, an observational period of several months (interior continental or coastal site, respectively) quite accurately. Changes in the tidal admittance could signal changes of physical properties at depth. Such observations could be useful in studies of earthquake mechanisms and prediction [Beaumont and Berger, 1978].

4. Because of the earth's liquid outer core, there is a near-diurnal (1.00217 cpd) free wobble [Wahr, 1979] that affects the tides. Very accurate measurements of the tidal response might reveal the details of the resonance and elucidate the nature of the hydro-dynamic coupling between core and mantle.

5. The tidal response can be used to map gross spatial variations in earth structure, such as the postulated partially molten rock underlying the Yellowstone region of Wyoming [Harrison, 1978]. As this response is dependent on rock parameters other than those governing the propagation of seismic waves, as in (2) above, valuable information is obtained.

6. New geodetic techniques such as Very Long Base Interferometry (VLBI) and Lunar or Satellite Laser Ranging (LLR or SLR) are approaching a precision of several centimeters (Chapter 24). The ranges, particularly the vertical component, must be corrected for tidal deformations of the sites, which can be of the order of tens of centimeters.

7. Earth tide measurements might be useful in observing possible nonlinearities in the deformational behavior of rock. These effects are much more detectable in tidal than in seismic measurements because the expected signal is much better known.

8. Advanced inertial components (gyros and accelerometers) are becoming sufficiently sensitive that the tides are detectable. They can thus provide low level, precisely-defined calibration signals.

9. Similarly, the tidal signal can act as a useful monitoring device of the response of instruments measuring long-period or secular deformations. The tidal amplitudes are of the same order as the annual tilt rate in tectonically active regions, although the periods are considerably different.

10. Tidal corrections have long been made to gravimeter surveys made for oil prospecting where the signals are of the order of 10–100 μgal (1 μgal = 1×10^{-6}cm/s^2). Normally only the solid earth tide, uncorrected for ocean loading, is applied although loading should be considered in high-precision surveys near coasts.

11. Similarly, earth tide corrections must be made to absolute gravity measurements to remove the time dependence. As the precision of these measurements is approaching 10 μgal, ocean loading terms must be included.

12. Finally, it should be mentioned that the tides affect satellite orbits, the rotational period of the earth, polar motion, and geodetic coordinates.

23.4.2.1 Solid Earth Tides. Numerous authors have derived expressions for the tidal potential on the earth caused by an exterior mass such as the sun or moon. Because of the nonlinear complexities of the orbits of the sun, moon, and earth, the tides display energy at the sum and difference frequencies corresponding to the periods

τ_1 = 27.3 days (lunar declination)

τ_2 = 365.24 days (solar declination)

τ_3 = 8.85 years (lunar perigee)

τ_4 = 18.61 years (lunar node)

τ_5 = 20940 years (perihelion)

τ_o = 1 solar day (24 solar hours)

τ_c = 1 lunar day (24.84 solar hours)

that is, $\sigma = S\left(\dfrac{\omega o}{\omega c}\right) + \sum_{k=1}^{5} M_k \omega_k$

$S = 0,1,2,3$

$\omega_k = 2\pi/\tau_k$

ϕ = longitude

Θ = phase angle

in harmonic representation,

$\sum C_i \cos(\sigma_i t + S_\phi + \Theta_i)$

for the long period (S = 0), the diurnal (S = 1), the demidiurnal (S = 2), or the terdiurnal (S = 3) tide-generating potential (at time t, longitude φ, and phase Θ with respect to Greenwich). The tidal force thus has energy in frequency bands about 0.3 cycles per day (cpd) wide, centered about 0, 1, 2, and 3 cpd with the frequency separation between components in each band corresponding to τ_1 and further splitting corresponding to longer and longer periods, as shown in Figure 23-25 [Agnew, 1979]. The number of harmonics required to adequately represent the tide ranges from 13 for a period of 1 to 6 months to 500 for decades [Cartwright and Edden, 1973]. Refer to Schureman [1958] for an exhaustive derivation of tidal harmonics.
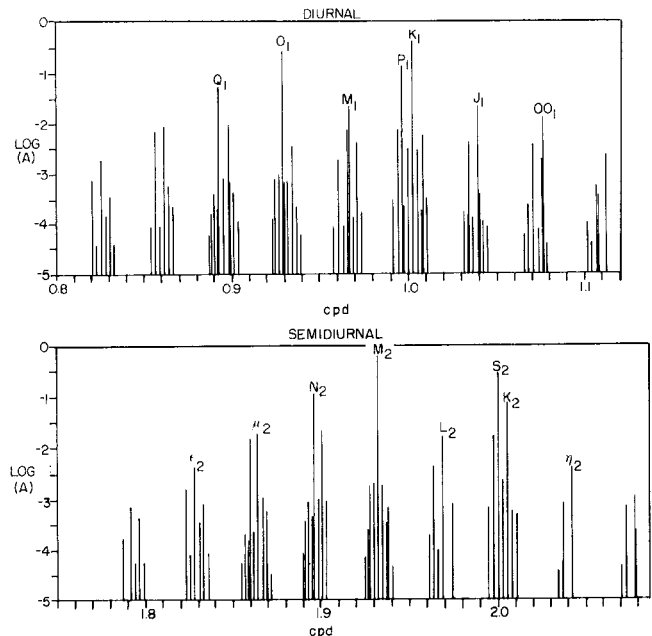

Figure 23-25. Tidal harmonics [Agnew, 1979].

The tidal potential itself cannot be observed, only changes in the vertical and horizontal components of the gravitational acceleration force g, which is the derivative of the potential. These components are the gravity tides $g = g \cdot z$ and tilt tides $h = |\bar{g} \times \bar{z}|/|g|$, where $\bar{z}$ is an earth-fixed unit vector parallel to mean $\bar{g}$. Occasionally tidal strain, the variation in distance between two nearby points, is measured while changes in the height of a liquid surface (the ocean tides) have been measured for thousands of years. Only in the past decade have tidal displacements of the earth's solid surface been measured with techniques such as satellite or lunar laser ranging and VLBI.

Although tides are almost always analyzed in the frequency domain, it is much more convenient to generate the theoretical tides as functions of time, the position of the disturbing body, and the position of the observer. The theoretical vertical g_m and horizontal h_m components of the

tide producing force of the moon on a rigid earth to the fourth order of lunar parallax to better than 0.04% are

$$g_m = \frac{GMr}{d^3}3\cos^2\Theta + \frac{3}{2}\frac{GMr}{d^4}(5\cos^3\Theta 3\cos\Theta)$$

$$h_m = \frac{3}{2}\frac{GMr}{d^3}\sin 2\Theta + \frac{3GMr}{2\ d^4}(5\cos^2\Theta - 1)\sin\Theta,$$

where

G = Newtonian gravitational constant

M = mass of the moon

d = distance between the centers of the earth and moon

Θ = zenith distance (angle) to the moon at the observation point

The vertical component is commonly expressed in microgal (10^{-6}cm/s^2) with reversal of sign to correspond to gravity observations, that is, a maximum tidal force produces a gravity minimum. The horizontal force is usually divided by the local value of gravity and multiplied by 1000, yielding the deflection of the vertical, or tilt, in nanoradians (10^{-9} radians), which may be converted to milliarcseconds (ms) by multiplying by 0.2063.

For the sun, the first term in each of the two expressions given above is adequate to the 0.002% level. The solar induced tides are 46% of the lunar. Numerous computer programs are available to calculate tidal time series [Cabaniss and Eckhardt, 1973].

On a rigid earth the maximum equilibrium tidal ranges are

	Gravity	Tilt	Geoid (or fluid earth)
moon	164.5 μgal	34.6 ms	53.4 cm
sun	75.8	15.5	24.6
Total	240.3	51.1	78.0

The theoretical amplitudes of gravity and tilt of the main tidal components as a function of latitude are given as Figure 23-26.

The earth is neither rigid or fluid but essentially elastic at tidal periods. Because the period of the longest free oscillation (54 min) of the earth is more than 10 times shorter than the tidal frequencies, the earth has more than adequate time to adjust to the tidal forces and its response is nearly independent of frequency. Thus the earth tides are of the equilibrium type; that is, the relative amplitudes and phases of the constituents should correspond to the theoretical ratios. Such behavior of a solid, spherical, oceanless earth can be described in terms of three characteristic numbers, h, k, and l. Historically, the reason for studying earth tides was to determine these so-called Love numbers, but they
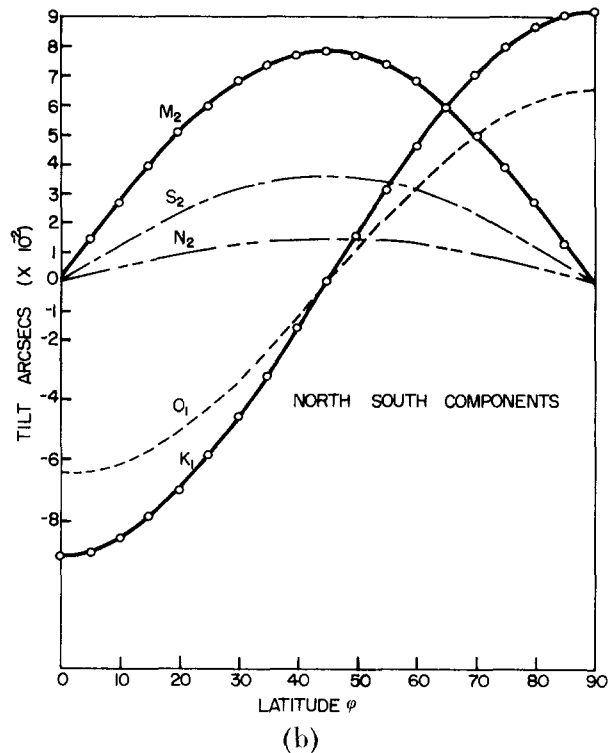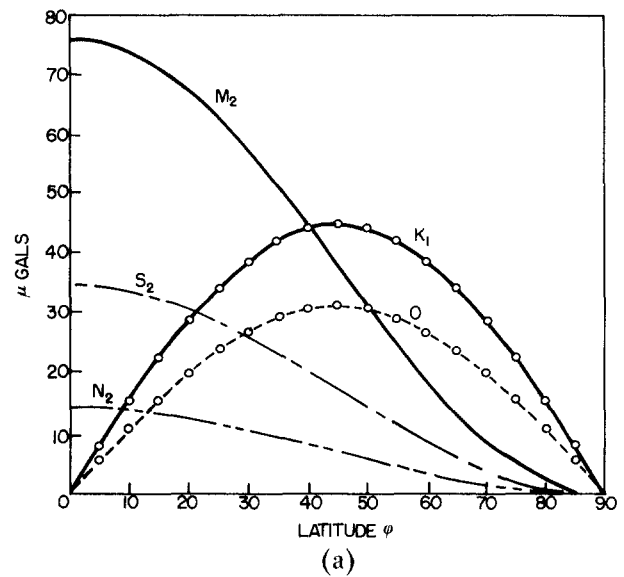
23-26

(a)

(b)

Figure 23-26. Amplitudes of the main diurnal and semi-diurnal earth tidal components versus latitude: (a) gravity, (b) north-south tilt, (c) east-west tilt.

can be derived much more accurately from seismic measurement because the tides are so perturbed by various indirect effects which will be discussed later. They are defined as follows:

h represents the ratio between the height of the tide on the elastic earth to the theoretical equilibrium height;

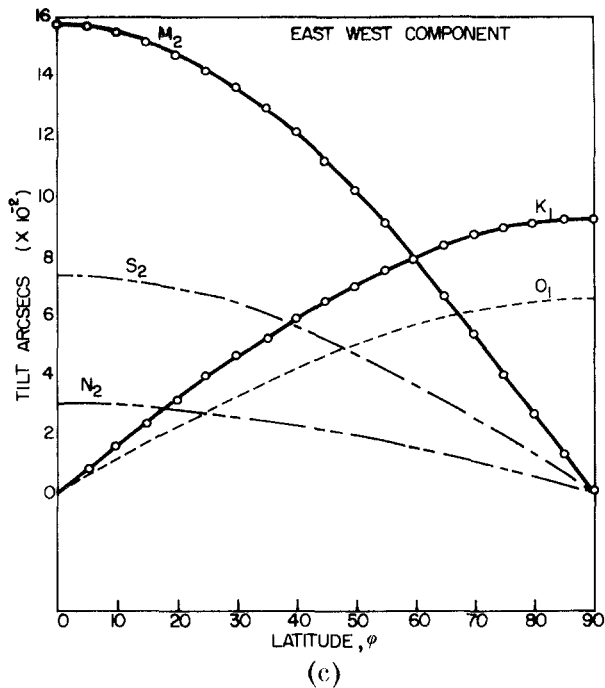k is the ratio of the additional potential due to the deformation of the elastic earth to the tidal potential; and

Figure 23-26. (*Continued*)

1 is the ratio of the horizontal displacement of the
elastic earth to the theoretical tide.
See Melchior [1966] for futher discussion.

From seismic data, $h = 0.603$, $k = 0.298$, and $1 = 0.084$ with a maximum variation of 1%–2% for reasonable seismic models. The ellipticity of the earth introduces latitudinally-dependent terms, but the effects are small [Wahr, 1979]. Thus the solid earth tides can be considered known on the surface of an oceanless spherically symmetrical earth. Here a tidal gravity meter would measure the equilibrium gravity tide $g_m + g_s$ multiplied by the constant $\delta = 1 + h - (3/2)k \approx 1.160$. Similarly, a tilt-meter would sense $(h_m + h_s)/g$ multiplied by $\gamma = 1 + k - h \approx 0.70$.

The gravity tides are increased by over 15% and the tilt tides diminished by about 30% because of elasticity. Surface strains depend on both h and l; the expressions are complex and will not be given here. See Agnew [1979] for details.

The one exception to the frequency independence of the earth to tidal forces is near 1 cpd, where the resonance caused by core-mantle coupling becomes important. Wahr [1979] finds from theoretical considerations that this effect should not exceed 20%. A number of investigators, including Levine [1978], have detected the phenomena but have not been able to elucidate the details of the resonance.

23.4.2.2 Ocean Loading Effects. The usual cause of the discrepancy between tidal theory and observation is the result of ocean tides, which can easily account for 10% of the total earth tide in gravity, 20% in strain, and 90% in tilt. The ocean tidal effect acts in three ways: (1) by the

direct attraction of the water, (2) by the physical bending of the crust beneath the weight of the water, and (3) by the distortion of the equipotential from the first two effects. Near seacoasts, the region of the ocean closest to the observation point causes the greatest perturbation and local ocean tidal models reasonably match the observations. In the centers of continents, however, all of the oceans are significant contributors (several percent) to the total signal. This is particularly true for the gravity tide, because the vertical component of the mass attraction of water decreases only as r^{-1} while the effect on strain and tilt falls off as r^{-2}, where r is distance.

Although the existence of ocean loading effects has been known for years, it was treated simplistically or even ignored until the 1960s for two reasons: (1) lack of methodology to calculate the effect loading and (2) poor open-ocean tidal models. Rapid advances have been made in both areas over the past decade, both requiring high speed computers.

The first attempts to correct for ocean loading used the solution for the displacements of an elastic, homogeneous, isotopic half-space subjected to a normal surface point load, which is called the Boussinesq problem. See Farrell [1972] or Lewkowicz and Cabaniss [1980]. When the attraction of the water mass and effects of the deformed potential are taken into account, the half-space model is often adequate for tilt corrections because most of the ocean loading contribution occurs within 1000 km of the observation point. Because the earth is spherical and radially heteorogenous, more realistic solutions are required. Takeuchi [1951], Longman [1962], and Kuo [1969], for example, made important contributions.

The complete problem was solved by Farrell [1972], who computed Green's functions for vertical displacement, gravity, tilt, strain, and horizontal displacements for a unit load on several realistic standard earth models. Using these functions $G(\Delta)$ for any of the above quantities, a mass M an angular distance Δ away would produce a change $MG(\Delta)$ in that quantity. Given an ocean tide model, one can convolve the tidal heights, with Farrell's tabulated Green's function, to compute the ocean loading. In practice, the oceans are compartmentalized and given the average tidal (complex) amplitude within each. Far away from the computation point the grid spacing can be coarse, but for points near coasts, the discretization must be comparatively fine [Goad, 1980].

The finite element method [Zienkiewicz, 1967] has been used by Beaumont and Lambert [1972] to deal with more complex structures, such as those with lateral variations, than those considered by Farrell. Such models are especially useful for computing tilts from nearby loads. This technique is quite adequate to an angular distance of about 30° but deteriorates beyond that because of the neglect of self-gravitation terms and the rigid bottom boundary required at the base of the model.

Concurrently, major advances have been made in the development of ocean tide models, a much more formidable

task than that for the earth tides. This is primarily because the natural frequencies of many of the ocean basins, gulfs, etc., are near the frequencies of tidal forces, so the dynamic resonant terms are important. Furthermore, nonlinearity plays a much greater role, particularly in shallow seas, because of friction and the nonlinearity of the equations for waves in shallow water, thus producing nonlinear tides called overtides by analogy with overtones.

Ocean tidal modelers integrate the Laplace Tidal Equations (LTE) to various boundary conditions, such as coastal tidal observations. Problems include dealing with realistic bathymetry, coastlines, and energy dissipation. In addition, only in the past 10 years have the self-attraction, loading, and solid earth tide term, all significant, been taken into account. Parke [1978] gives a review of the progress through 1978.

More recently Schwiderski [1979, 1980] has published a series of models for many of the major tidal constituents (M_2, O_1, K_1, N_2). These are available in geographical grid form on magnetic tape. In 1981, the Permanent Commission on Earth Tides, formed under the International Association of Geodesy of the International Union of Geodesy and Geophysics, adopted the Schweiderski models as the standard for ocean loading corrections.

Two problems still exist with ocean tide models. The first is that tide gauges are used for defining the boundary conditions. Almost invariably they are located in anomalous sites, that is, sheltered harbors, where tides are distorted for a number of reasons. Open ocean measurements using pressure transducers on the ocean floor are needed, but these are sparse and the number only slowly increasing [Cartwright, 1982]. Another problem is that world ocean models lack sufficient detail and accuracy near the coasts for earth tide measurements taken there. In some locales, for example the North Sea and southern California, local models are available which can be integrated with the coarser grids. Future advances will probably be made with satellite altimetry (Chapter 24), which has become sufficiently precise (fractions of a meter) to directly detect ocean height changes. The major problem to be overcome is orbital errors, an active area of research in the satellite geodesy community.

23.4.2.3 Cavity, Topographic, and Geological Effects.

To avoid the overwhelming noise generally caused by temperature changes, rainfall, and soil moisture variations, tidal strain and tilt measurements have traditionally been made in underground mines, tunnels, or special cavities excavated for specific geophysical purposes. These openings, often in mountainous terrain of complex geology, are almost always excavated by explosions. Furthermore, short-base (less than 1 m) tiltmeters have often been placed in special "niches," carved with hand tools or jackhammers, in tunnel walls [Melchior, 1966].

The spatial variations of tidal tilt parameters measured in Europe through the early 1970s showed a disturbing lack of smoothness far beyond that attributable to crustal struc-

ture, inadequate ocean loading corrections, or instrumental unknowns. At some sites, significant changes occurred among instruments separated by meters or less [Lennon and Baker, 1973]. In 1973 King and Bilham pointed out that the cavities in which most instruments had been operated were subject to distortion by tidal strains. Tiltmeters installed, for example, in a circular tunnel at A and B in Figure 23-27 will

HARRISON 1978

A CIRCULAR TUNNEL IS DEFORMED BY HORIZONTAL STRAIN. TILTMETERS AT A AND B RECORD STRAIN-COUPLED TILTS AND THE HORIZONTAL STRAINS ACROSS THE TUNNEL IS THREE TIMES AS LARGE AS THEY WOULD HAVE BEEN PRESENT.
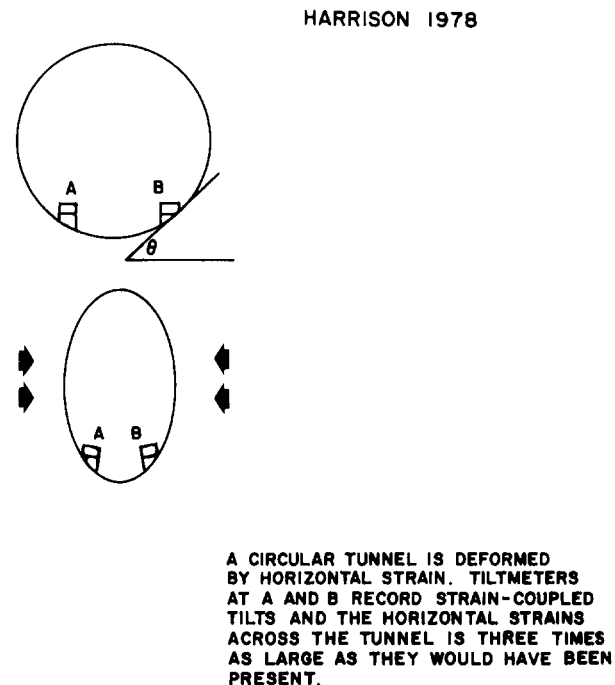
Figure 23-27. Strain-induced tilt in a circular tunnel [Harrison, 1978].

record strain-induced tilts equivalent to twice the horizontal strain. Similar effects are generated by topographic and geological irregularities. Since most theories dealing with the earth tides or seismic wave generation and propagation consider large-scale deformations on the free surface of comparatively simple earth models, it is difficult to relate these to the measurements made in locally complex regions.

Harrison [1976] has treated analytically the effects of ellipsoidal and cylindrical cavities and has made finite element calculations of more complex cavities, topography and geology. For example, the floor of a long tunnel shows no strain-tilt effect along the axis, nor does the side of a vertical borehole. Cracks and narrow cavities, however, induce large strains and tilts. Topographic distortion can also be substantial, with strain effects of several hundred percent. Berger and Beaumont [1976] have corrected the results from a number of earth strain observatories for cavity, topographic, and geological (that is, material inhomogeneity) effects using finite elements. These corrections generally improved the agreement between theory and observation, primarily because strain measurements are usually made over long (>30m) baselines along tunnels, where the corrections are normally small and cracks and inhomogeneities relatively

insignificant. For measurements made with short-base tilt-meters, however, the case is much more serious, not because of the complexity of the known cavity, which can be modeled sometimes expensively, but because of the unknown fracture pattern in the vicinity of the tiltmeters. Thus all earth tide measurements made with these instruments were essentially useless, except those made in vertical boreholes and possibly those designed to monitor temporal variations in the tidal parameters.

These cavity, topographic, and geological effects are frequency independent, including both slow tectonic movements and sudden earthquake offsets, as well as tides. Gravity measurements, however, are vitually unperturbed. To be free of such perturbations, tilts must be measured with long base instruments in shallow trenches excavated in flat terrain or borehole tiltmeters referenced to the side of a vertical hole [Wyatt et al., 1982].

23.4.3 Other Motions

In this section the causes, magnitude, and methods of measurement of other types of earth motions are discussed. Also addressed are those spurious motions that are often measured by an investigator who is attempting to record tectonic or tidal deformation. These include the effects of surface loading, groundwater and soil moisture, and temperature fluctuations, as well as those from the pumping of oil and water from wells. While probably not as geophysically interesting as the broader scale phenomena, these deformations are often larger and their causes more subtle, and they are often more likely to affect the testing and operation of sensitive systems, such as gyrocompasses.

23.4.3.1 Motion Background. In Section 23.3.3.1, the noise spectrum for short-period motions was discussed in terms of acceleration, velocity, and displacement. The large site-dependent amplitude variations cited are a result of both the type and strength of noise source and the proximity and characteristics of the measurement site; that is, the amplitude is much higher at a point on unconsolidated sediments near a freeway than on a pier on bedrock at an isolated location. Also, the short-period noise spectrum is characterized by a number of strong peaks and pronounced minima.

In contrast is the background strain spectrum derived from measurements at one site in Colorado and two sites in California [Berger and Levine, 1974]. They showed (Figure 23-28) that the background rises at an almost constant slope of f^{-2} over 10 decades (10^2 to 10^{-8} Hz) of frequency corresponding to periods ranging from 10 ms to about 1 yr, and that the power levels for two different types and lengths (30 m versus 750 m) of instruments at very different sites, Colorado mine versus California desert surface, are almost identical. Of course certain portions of the spectrum are not time or space invariant: large earthquakes excite the normal modes and the microseisms show pronounced peaks at 8
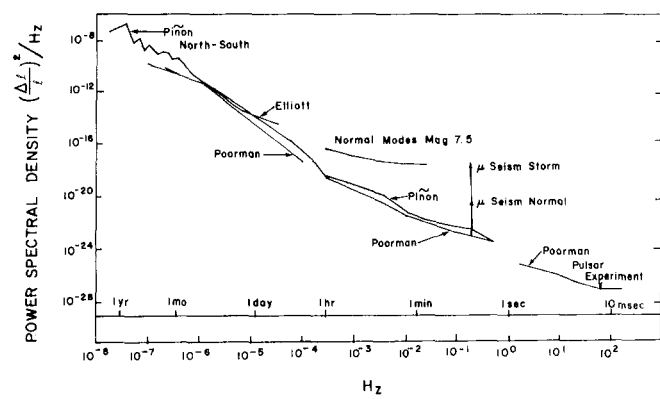

Figure 23-28. Background strain spectrum [Berger and Levine, 1974].

and 16 s periods. The earthtides were removed prior to computing the spectrum. Wyatt [1982] presents similar data on motions of reference monuments. These authors surmise that these observations are probably representative of the strain at any reasonably quiet site in the world or are an upper limit. The tilt spectrum should be essentially identical because the ampltidues of the rotational components, including tilt of the strain tensor, should be about the same as those of the linear ones.

23.4.3.2 Surface Loading. Ocean loading has a significant effect on earth tides. Their removal is particularly difficult because both occupy the same frequency space. Other variable or moving loads (trucks, trains, people, water in lakes or rivers, snow) can produce measurable deformations of observation sites. Their contributions can sometimes be calculated and removed, but almost always order of magnitude estimates can be made.

Farrell [1972] presents the method for computing Green's functions (point load response) for realistic earth models for tilt, gravity, and strain. Far simpler are the expressions for displacements at any depth in an elastic, homogeneous half-space, also included in Farrell's paper. These, as well as formulas for tilt of vertical and horizontal line elements, are given by Lewkowicz and Cabaniss [1980]. Near the load, the horizontal tilt can exceed the vertical by as much as a factor of three, the exact ratio being a fraction of Poisson's ratio. A number of authors, including Kuo [1969], have derived approximations of the response of horizontally layered elastic models to vertical point loads. The finite element method is useful for more complex models and loads. Formulas for distributed loads, such as discs, hemispheres, and hemi-ellipsoids, are given in a number of texts including Farrell [1972] and Herbst [1979]. Usually, effects of distributed loads can be very adequately and easily approximated by subdividing the surface into suitably sized cells, computing the point load contribution of each, and summing the results.

Numerous cases of atmospheric pressure changes causing significant (several times the tidal amplitude) tilts and

strains appeared until the early 1970s in the literature [Melchior, 1966]. Some authors postulated the coherent movement of crustal blocks hundreds of kilometers wide and partially decoupled from adjoining blocks. Herbst [1979] argues convincingly that such observations must result from local or instrumental phenomena. He modeled an unusually intense cyclonic low of 50 mb and found that the maximum vertical displacement for any reasonable load distribution was 16 mm at the center of the loaded region, with a tilt of 45 nrads at the center and edge, far less than the typical tidal tilt of 100 nrads. He was able to show that the apparent correlation with air pressure changes was actually a result of the concurrent rainfall draining into the fractured rock near his borehole instruments, a phenomenon that will be treated in greater detail later. This is not to say, of course, that air or water pressure changes acting normal to sloping terrain cannot produce significant tilts. This is especially true in clays and other low-permeability materials where diffusion of pore fluids becomes important [Zschau, 1976]. Direct pressure effects on instruments act by either distorting compliant sealed cases or buoying the mass in unsealed cases. The variations of mass attraction of the atmosphere must be considered in very precise earth tide gravimetry.

Vehicles and fluid storage tanks can produce significant tilts and tilt rates at nearby test facilities built on unconsolidated soils. The load produced by a vehicle can be modeled as a single point source at distances greater than three times the vehicle diameter, and as the superposition of four point loads, the wheels, at lesser distances. Lewkowicz and Cabaniss [1980] examined the tilts produced by a 1500 kg vehicle. They found the maximum vertical tilt at a depth of 1.3 m was 1.25 μrads at a horizontal distance of 1.3 m (nearest axle), which rapidly diminished to 0.2 μrads at 6 m. The maximum, unmeasured horizontal tilt was calculated to be a factor of three or larger. Water tanks or similar loads can be treated as disc loads nearby and point loads at distances greater than five times their radius.

23.4.3.3 Thermoelastic Effects. As materials are heated, they almost always expand, thus producing stresses and, usually, strains and tilts. These are almost always observable on instruments installed in buildings and on or near the earth's surface. Numerous authors give formulas, tables, and curves for calculating heat flow from various types of source distributions through media of some complexity. Finite element methods are also particularly suited to making such computations. In geological materials, problems almost always arise because the relevant material parameters are unknown: they vary both spatially and temporally, and the movement of groundwater and soil moisture greatly complicates the issue. Thus, most models used in geophysics are comparatively simple.

Harrison and Herbst [1977] discussed thermoelastic strains and tilts from the geophysical instrumentation standpoint. The most important components are the diurnal and annual temperature waves, which penetrate as damped progressive

waves in semi-infinite halfspaces. The skin depth at which the amplitude decays to 1/e is about 1 m and 20 m in typical earth materials for these two periods. In this model the rock or soil can expand only vertically because it is confined laterally by equally heated materials, and horizontal compressive stresses develop; therefore, there is only vertical strain, no tilts or horizontal strains. However, instruments installed even in such an ideal material could be affected by asymmetry of their mounts or inherent temperature sensitivity. In the real world with finite surface topography and variations of thermal properties, sideways expansion can take place, thus generating tilts and horizontal strains. Harrison and Herbst [1977] derive an expression for tilts and strains on uniformly sloping topography with a constant thickness thermal boundary layer. For a temperature wave of 283 K on a slope of 6°, the strain is 2×10^{-6} and the tilt is 20 μrads, both falling off at greater depths as does temperature.

For more complex topography, finite element calculations have proved quite satisfactory. Herbst [1979] was able to explain annual tilts of 0.625 and 0.125 μrads observed at depths of 15 and 30 m, respectively, with a 2-D, three-layer, finite element model of this site, which had an annual temperature wave of 281 K amplitude at a depth of 1 m. This technique should be useful in assessing the temperature sensitivity of various structures.

In buildings and other facilities, especially those exposed to solar insolation, the tilts can be very large. As one side of a building expands, it bends, flexing the floors and transmitting stresses to its foundation. These can affect test piers completely decoupled from the building floors and walls unless such piers are some distance from the foundation. Figure 23-29 [Tsutsumi, 1970] shows the tilt on a pier in an insulated building standing on exposed bedrock on a low, forested hill and with no temperature control. The annual variation is over 100 arcseconds (about 485 μrads). Even in buildings with some temperature control, thermoelastic effects are difficult to avoid because it is almost impossible to change temperatures uniformly throughout an entire room. Figure 23-30 shows the tilts and air temperature (clearly diurnal) measured near the center of a massive concrete pier. First, note that the phasing between temperature
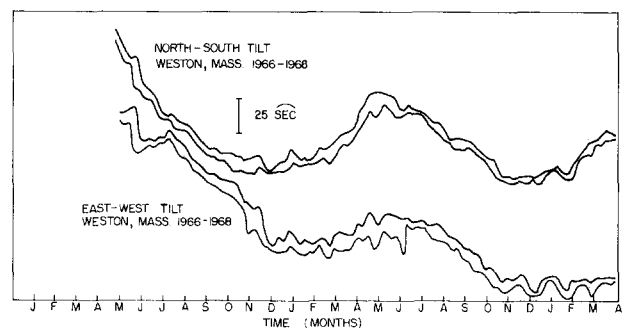

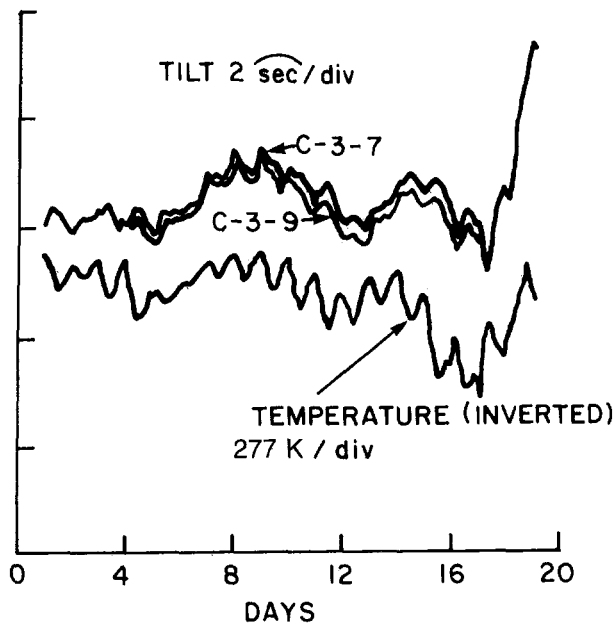Figure 23-29. Weston vault tilt [Tsutsumi, 1970].

Figure 23-30. Haskell pier tilts and temperature.

Figure 23-32. Silo rotations and temperature.

and tilt is not constant. This is because the pier is affected by thermoelastically-induced tilts, transmitted through the foundation and bedrock to the pier, caused by the outside air temperature and insolation variations that are out of phase with the room temperature. Second, note the disagreement between two tiltmeters set on the same plate several centimeters apart. The differences between two other pairs of adjacent instruments are shown on an expanded scale in

Figure 23-31. Haskell difference tilts and temperature.

Figure 23-31. Blk 2 and Blk 1 are in the same housing and the discrepancies, probably due to small misalignments, do not increase with temperature; however, the C3 and C4 obviously have different temperature coefficients, an example of the direct temperature effect. A clear and dramatic example of thermoelastic rotations is presented in Figure 23-32, which shows rotations about the vertical axis ϕ_z and two horizontal axes, Θ_{North} and Θ_{East}. Also shown is the temperature (T_B) measured at a depth of 10 m beneath the ground surface in a missile silo. Aside from various activities in the silo, the most striking feature is the strong diurnal character of the rotations and complete lack of daily fluctuation in air temperature. The tilts even have the shape of the typical diurnal outside temperature curve, a rapid change of temperature until noon and a decreasingly slow return during the afternoon and night. The troughs are within one hour of local noon and the measured flexure is in an ENE-WSW direction. The effects of heating the exposed concrete are obviously transmitted thermoelastically far down the structure. Such large motions would never be predicted from half-space calculations.

23.4.3.4 Soil Moisture and Groundwater. Soil moisture and the movement of groundwater through rock fractures, soil, and other unconsolidated sediments can cause large ground motions, and these are the most difficult to model and predict because of the complex mechanical behavior of soil materials.

The most obvious phenomenon is the lowering of the ground surface in regions where oil or water is being extracted from poorly consolidated sediments. Dramatic examples of this occur along the Texas-Louisiana Gulf Coast, Las Vegas, and the San Joaquin Valley of California, where

23-31

the elevation has changed 8.5 m from 1926 to 1972 due to groundwater pumping. Subsidence rates can be extremely high: 13 mm/yr in Louisiana and as great as 24 cm/yr in California [Committees on Geodesy and Seismology, 1981]. In Arizona, between Phoenix and Tucson, subsidence caused by groundwater pumping has produced a fault over 13 km long and with offsets up to a meter [Holzner et al., 1979]. The mechanism is the removal of the supporting pore pressure between the soil particles, particularly the clay fractions. The process can be halted and partially reversed by recharging the affected strata. In Long Beach, California, serious subsidence caused by oil pumping was arrested and is no longer a threat despite continued exploitation because water is injected at the same rate as petroleum is extracted. Damage appears in the form of ruptured well cases, coastal flooding, shifted foundations, and improper flow in surface canals and aqueducts. Subsidence patterns are mapped by releveling and by measurements on well casings. GPS and VLBI surveys (Chapter 24) should be applicable here.

The usually unpredictable effects of the subsurface movement of water can seriously hamper geophysical measurements. Herbst [1979] was able to show that surface water from rain and melting snow moving into vertically-fractured rock caused large, erratic tilts of borehole instruments. Apparently the pressure head differences in adjacent fractures caused sufficient bending movement in the rock between them. The noise levels created were so great they significantly degraded the tidal results, even from an instrument as deep as 30 m, and made it impossible to measure tectonic motion, if any. Attempts were made to model this mechanism using linear systems techniques to predict the effects and correct the tilt measurements given the amount of precipitation and temperature, but these were unsuccessful because of the nonlinear, time-varying nature of the phenomenon and other variables.

One of the most successful and stable sets of long-term strain measurements is from the Pinon Flat Observatory in southern California [Berger and Levine, 1974], but these results too are contaminated by tilts and horizontal motions of the large granite piers at each end of the three 750 m laser strain-meters. Wyatt [1982] has made an extensive study of six years of Pinon Flat data and concludes the random motion in the partially weathered bedrock, although obviously related to temperature and precipitation, is unpredictable. It seems that small-scale inhomogeneities and the subtle variations in the stress field caused by soil moisture and temperature variations are too time-variable to model. These effects are also obvious in the Pinon Flat shallow tiltmeter data [Figure 23-33, from Wyatt et al., 1982]. Beta and Delta are Kinemetric instruments (sensor in the base of a 1.1 m stainless steel tube) sand-packed into holes 4.5 m deep, ADL is an A. D. Little instrument at 26 m, and LFT is a 535 m long fluid tiltmeter. The precipitation effects on Beta and Delta are obvious, as are the thermal ones in their spectra [Figure 23-34, from Wyatt et al., 1982]. Here the meteorological inputs have raised the noise levels of the
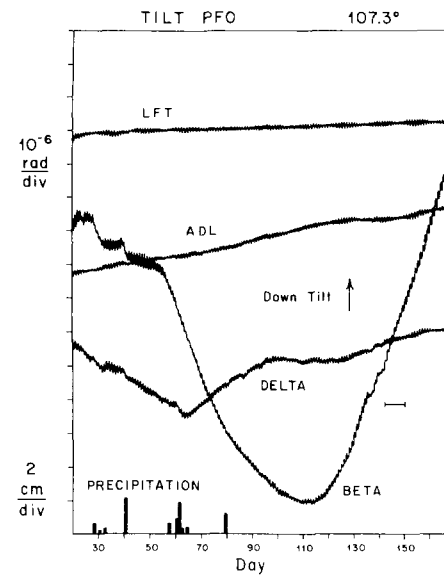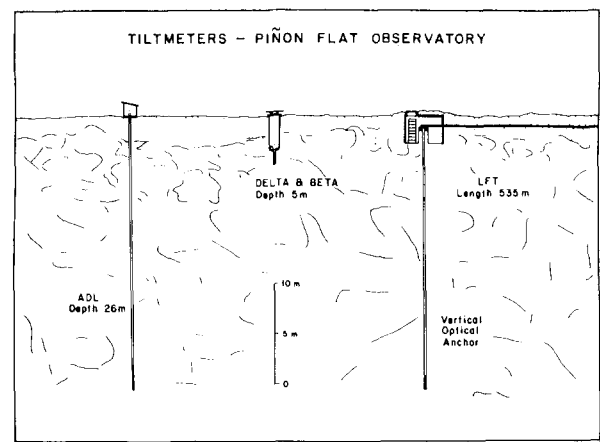

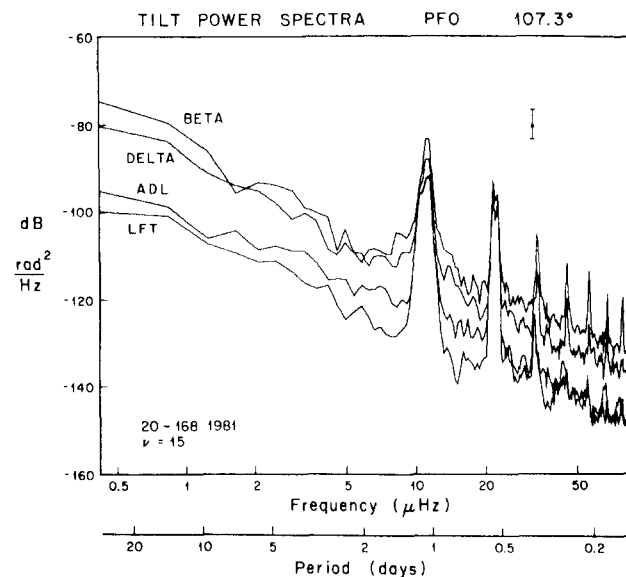Figure 23-33. Pinon flat tilts [Wyatt et al., 1982].

Figure 23-34. Pinon flat tilt spectrum [Wyatt et al., 1982].

shallow instruments about 20 dB above those of the other two and rendered them useless for the measurement of long-term tectonic movements. The unpredictable monument motions also have serious implications for strain measurements. Wyatt [1982] points out that a 7 km long instrument would be required to measure the approximately 1×10^{-7} yearly strain-rate observed in California to within 10%. His solution has been to reference the surface monuments to the deeper, presumably more stable, bedrock with an "optical anchor," which is essentially an interferometer with two paths inclined at 45° to the surface down to a depth of 15 m. Even with lines of 20-50 km, the stability of monuments

is important: 0.5 mm being 0.1×10^{-7} on a 50 km line, movement easily caused by thermal or soil creep phenomena.

Another example of the problems associated with continually monitoring secular crustal movements is shown in Figure 23-35 [Cabaniss, 1978]. Data from three borehole tiltmeters installed 3 m from the bottom of cased holes 100 m apart and 100 m into bedrock beneath 20 m of overburden have been rotated into North and East components. Relevels have not been removed from the first eight months of data from #1 or two months from #2. The rapid drift starting at Day 740 seen on #2 North actually occurred almost
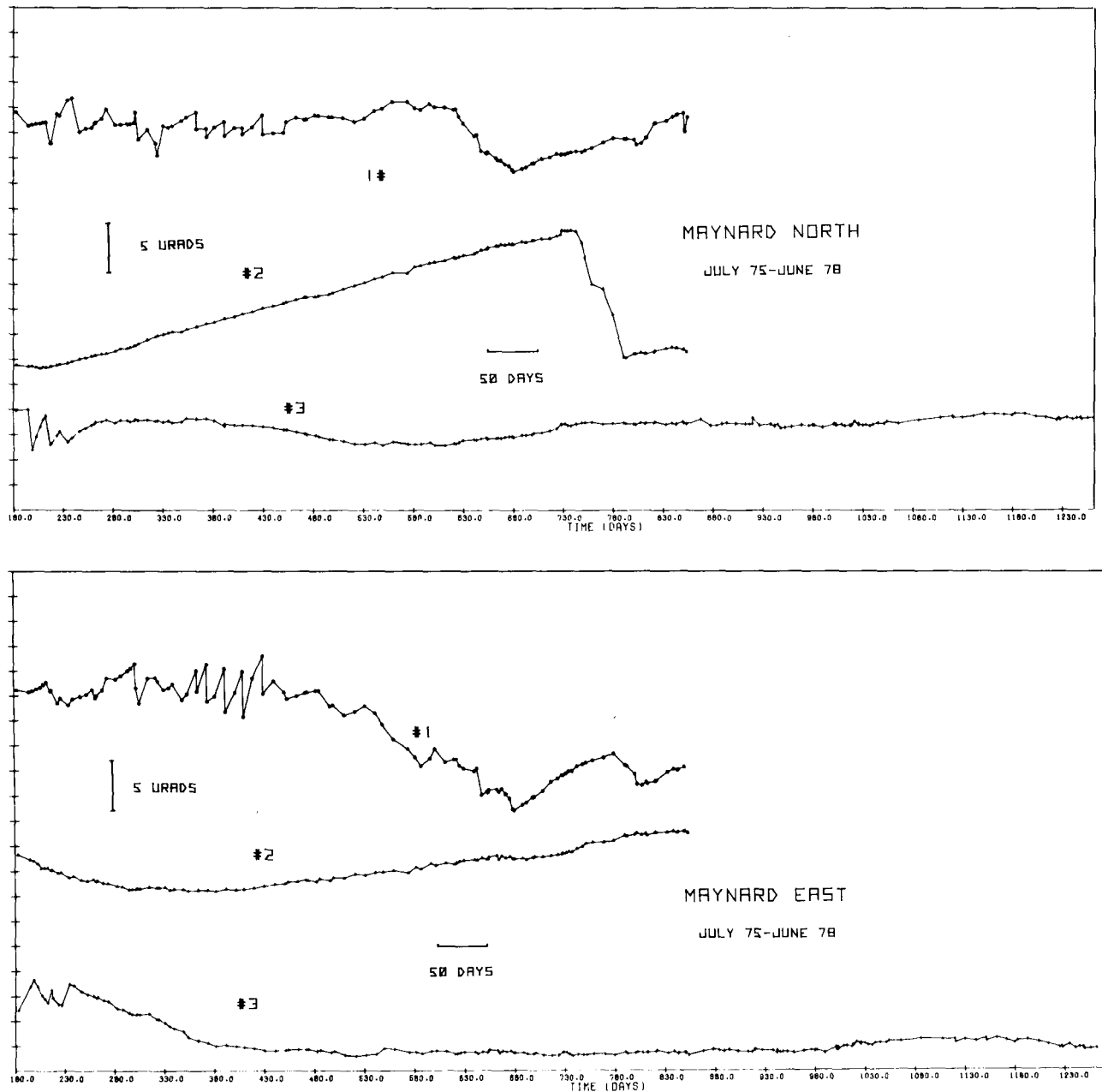

Figure 23-35. Maynard tilts.

equally on both channels but in opposite directions. It lasted for 45 days and was possibly caused by corrosion of the mild steel casing. Instrument #3 displayed remarkable stability over the three year period, the net change being 0.3 μrad, with a maximum excursion of 2.0 μrads. The #3 drift rate is about 0.1 μrad/year down to the SW. Leveling [Brown, 1978] and tide gauge data (Figure 23-24) suggest a rate of 0.01 μrad/year down to the North.

23.4.3.5 Conclusions.

A host of extraneous motions make the measurement of tectonic and other geophysically interesting crustal deformations difficult, particularly for long time periods. These same motions are usually the ones that cause structural damage and corrupt test results and operation of sensitive systems in near-surface facilities. In most cases, the usual geophysical deformations are of little or no consequence except, of course, for earthquakes and volcanic activity.

The measurement of long-term crustal deformation is highly dependent on reference point stability. At the present time only repeated annual surface-based geodetic measurements over 20 to 50 km lines and continuous long base tiltmeter measurements appear to have the necessary precision to monitor the strain-rates observed in California. Space-based techniques have the potential for extending this precision over longer distances and vastly increasing the frequency of measurement.

23.5 ROTATIONAL MOTIONS

Rotational motions are typically classified by geophysicists as either azimuthal rotations or tilt. Azimuthal rotations are those motions that occur in a horizontal plane about a vertical axis, while tilts occur about axes in the horizontal plane. Both the relative motion of a reference device over time and the absolute motion with respect to a permanent reference, such as an astronomical or earth fixed coordinate system, are of interest to geophysicists. However, since recent research has emphasized improving azimuth measurement accuracy, the discussion in the following sections will focus primarily on azimuthal rotations.

Knowlege of true azimuth or azimuthal rotations has applications for pointing, tracking, navigation, and evaluation of geophysical phenomena. Historically, except for surveying applications, the Air Force interest in making precise azimuth measurements has been limited to (1) establishing or verifying the azimuth of a reference mirror in a test laboratory, (2) establishing a reference for a tracking device such as a radar antenna, or (3) initializing and/or verifying the performance of an inertial navigation system.

Until recently, the accuracy required for these functions has been on the order of 5 arcseconds of uncertainty. Since short period motions of azimuth references are typically less than or equal to this measurement uncertainty, azimuth was normally considered to be a quasistatic parameter and was

measured intermittently (every few months or longer). A time history, referred to as a "data base," was frequently used to describe the long period or step motions of an azimuth reference.

Little improvement was made to either instrumentation or measurement techniques for several decades until the need for high accuracy missile navigation systems forced the R&D community to explore new technology for azimuth measurement. These systems require measurement accuracy of less than 1 arcsecond over much shorter measurement periods. Thus, the smaller geophysically and culturally induced motions of the target point as well as those of the measuring device are now significant, and classical measurement techniques are nearly obsolete.

Recent research has advanced both instrumentation and measurement techniques. This section addresses the most common of these advancements, including their improvements as well as their limitations. The discussion highlights both instrumentation errors and the geokinetic influence on instrument performance.

23.5.1 Definition of Azimuth

Prior to discussing the various measurement techniques, however, it is first important to define azimuth to ensure consistency in performing and reporting azimuth measurements. Generally, the azimuth of a point is defined in terms of either an astronomical or geodetic coordinate system [Department of Defense Glossary of Mapping, Charting, and Geodetic Terms, 1973].

The astronomic azimuth between two points P and Q is illustrated in Figure 23-36 [Mueller, 1969]. It is defined as the angle "α" formed by the intersection of the observer's astronomical meridian with the plane containing the observed point and the true normal (vertical) of the observer, measured in the local horizontal plane clockwise from true North.

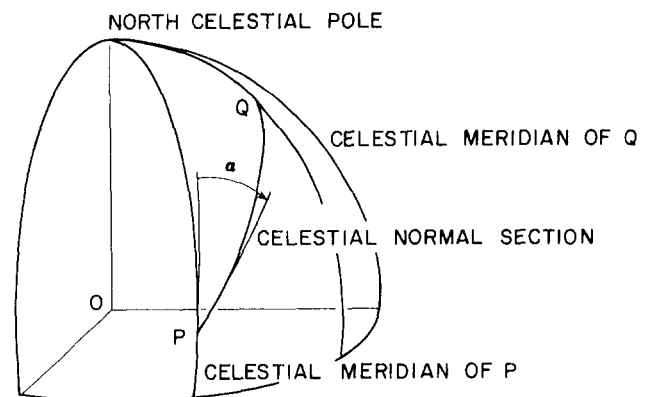The geodetic azimuth is the angle between the geodetic

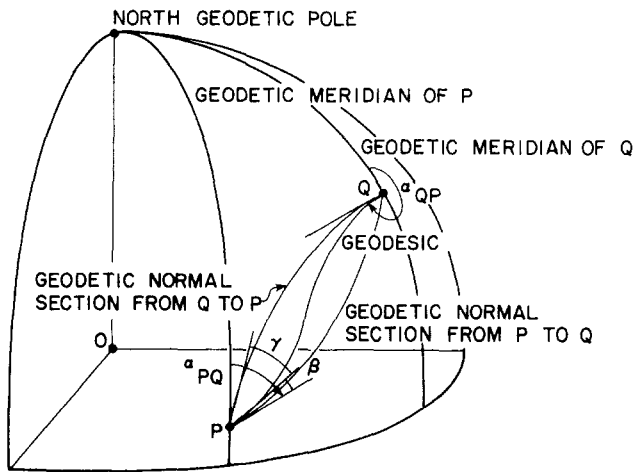Figure 23-36. Azimuth on the celestial sphere [Mueller, 1969].

Figure 23-37. Azimuth on the ellipsoid [Mueller, 1969].

meridian and the tangent to the geodesic line at the observer, measured in the plane perpendicular to the ellipsoidal normal of the observer, clockwise from South. This is illustrated in Figure 23-37.

It is sufficient to say that the difference between the two definitions is the figure of reference. Astronomical azimuth refers to the astronomic rotation axis of the earth while geodetic azimuth refers to an ellipsoidal model of the earth and its respective mathematically defined pole. For our discussion, we will refer only to astronomic azimuth.

23.5.2 Conventional Azimuth Determination

Normally, we want to know the azimuth of a line of sight normal to the mean surface of some target or test fixture which is located at some angle with respect to true North. Thus, the problem is divided into two parts: (1) determining the azimuth of the line between the observer and a known reference such as a star at a specific epoch of time, and (2) measuring the horizontal angle between the star and the target. Star observations are made using theodolites. The circumpolar star Polaris is preferably observed since its near-zero azimuth minimizes the effect of errors in knowledge of the station latitude on the azimuth determination. The celestial coordinates of Polaris required to compute its azimuth are obtained from a star catalogue.

Figure 23-38 illustrates how this technique may be used in a test facility to establish an azimuth reference with a fixed mirrored cube. The master cube is used as a mean azimuth reference after repeated observations of the star and the cube from the theodolite station. The azimuth of the master cube can be calculated simply by adding the angle between the cube and the star to the azimuth of the star. The pentaprism is used solely to observe the surface of the master cube from a geometric setup which does not allow direct access from the theodolite station.
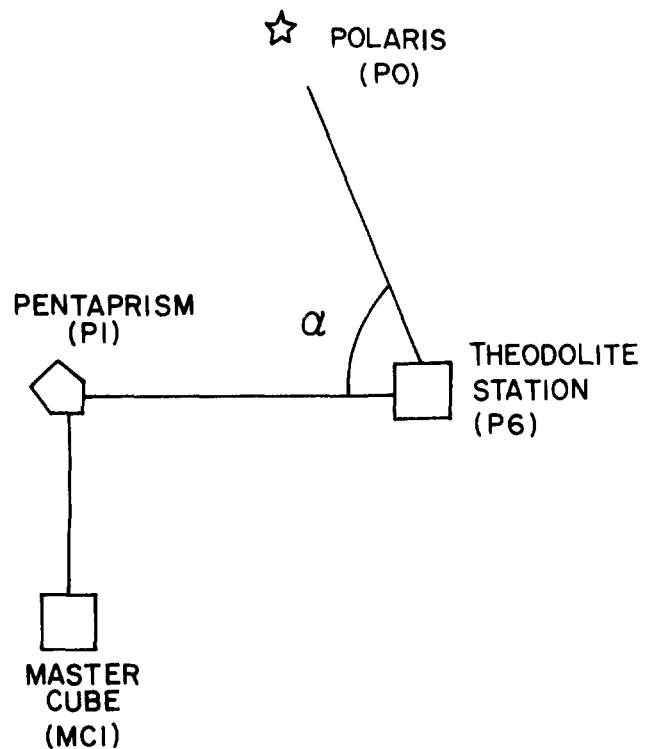

Figure 23-38. Schematic of typical astronomic azimuth observations in an inertial test facility.

Conventional azimuth measurement techniques are severely limited by a number of factors as illustrated in Table 23-6 [Roberts, 1980]. The largest single error source is the "personal equation" of the observer, which can contribute several arcseconds of bias and uncertainty to the azimuth estimate.

In addition, conventional observations are limited to clear nights and, therefore, inherently prohibit observation of motions of the desired target within periods of less than 24 hours. These motions are typically 1 arcsecond and can be as large as 5 arcseconds.

Few improvements to conventional measurement technolgy have been made in recent years. However, one significant improvement may result from research at the University of Maryland sponsored by the Defense Mapping Agency under the supervision of Air Force Geophysics Laboratory. This research has led to the development of a prototype array eyepiece system for a Wild T-4 theodolite known as a Charge Couple Device (CCD). The prototype CCD automatically "observes" and records the transit of a star across a photo-diode array which has known coordinates with respect to the T-4, thereby removing observer errors. The path of the star across the array is then used to determine an estimate of the reference azimuth that is independent of observer bias. This azimuth is then transferred in the conventional fashion to the desired target [Currie and Salvermoser, 1981].

Table 23-6. Azimuth or horizontal angle error sources [Roberts, 1980].

Error Source	Instrument	Magnitude (sec)	Ref	Notes
Elastic deformation of leveling screws	T4 DKM3	0.05 0.15	8	
Clamping error		0.1 to 0.2	1	Cancels by averaging for equal torques
Thermal flexing of telescope by touching one side	DKM3	0.16	9	May tend to cancel by reversal
Mechanical flexing of telescope	T4	0.7	10	
Trunnion axis roll error	T4 DKM3	0.6 0.1	8	
Trunnion axis wobble error	T3 T4 DKM3	−1 to +0.5 0.4 0.1	11 8 8	
Level vials	DKM3	0.5	1	Tends to cancel over many sets of observations
Atmospheric refraction		0.1	10	
Observer biases	T3	±2.84	12	
Timing error		0.06 to 0.15	1	
Petaprism residual error		±0.25	1	
Elliptic horizontal circle distortion of 10^{-4} inches		2		Cancels by circle rotation
Eccentric graduations on horizontal circle by 10^{-4} inches		0.4		Cancels by circle rotation
Porro prism can't angle		±0.14	1	
Misalignment of horizontal circle and telescope vertical axes of 10^{-4} inches		0.4		Does not cancel by circle rotation
Movement of long line mark by 1 cm in 1 nm		1		
Blunder. (Acceptance of one 5 s blunder in 16 sets)		0.3		Possible with wide rejection tolerance
Model assumptions		±0.45		This report

23-36

Table 23-6. (Continued)

Error Source	Instrument	Magnitude (sec)	Ref	Notes
Star Models		0.1		
Random circle graduation errors		~ 1.5 to 1	13	
Optical window		±0.125	2	
Non-flatness of cube or mirror faces		±0.06	2	
Thermal circle index drift		0.3	10	

23.5.3 Inertial Azimuth Determination

The heart of any inertial azimuth system is the gyroscope. When it is operated as a gyrocompass like the Azimuth Laying Set (ALS) in Figure 23-39, the gyro senses a component of the earth's rotation rate which is proportional to azimuth.

The single degree of freedom (SDOF) floated gyro used in the ALS may be described as a sealed cylindrical canister within another canister. The inner canister called the float, immersed in a fluid at neutral buoyancy, contains a rotating wheel which generates angular momentum. The SDOF gyro has three principal axes which are defined by the wheel and float orientation and the gimbals on which the gyro is mounted as illustrated in Figure 23-40a. The spin axis (SA) and output axis (OA) are physically defined by the wheel axis and the longitudinal axis of the float, respectively. The input axis

Figure 23-39. Azimuth laying set gyrocompass.

(IA) is defined as mutually perpendicular to SA and OA. In general, any gyroscopic element (wheel and axle) has an infinite number of pairs of input and output axes at right angles to each other. The number of gimbals, in our case two, defines the degrees of freedom and therefore the sensing axes.

During operation, the gyro wheel is rotated rapidly about the spin axis which generates angular momentum (H). When an angular rate is introduced about the input axis (ω_{IA}), a precessional torque (Mo) is generated about the output axis which is proportional to the vector cross product of H and ω_{IA}. This torque can then be expressed mathematically as

$$Mo = H \times \omega_{IA}$$

23.5.3.1 Gyrocompassing. The gyro is capable of sensing any rotation about its input axis. If the gyro is maintained in a fixed orientation on the earth, it senses a component of the earth's rotation rate that is proportional to the angle between the input axis and the earth's rotation axis.

To measure azimuth with a sensor like the ALS, the gyro is oriented so that the input axis is nearly east or west in a local horizontal plane where the sensitivity to small azimuth change (sensed earth rate) is maximized. The earth rate sensed by the gyro is then $\omega_{IA} = \omega_{EH} \sin \alpha$, where ω_{EH} is the horizontal component of the earth's rotation rate $[\omega_{EH} = \omega_E \cos (LAT)]$, and α is the desired azimuth of the input axis defined from astronomic East. Note that the effect of latitude on gyro output is compensated for by applying a scale factor to the gyro output signal. By combining the equations for torque and IA rate, we can solve for azimuth of the IA in terms of the gyro's torque output:

$$\sin \alpha = \frac{Mo}{HW_{EH}} - \varepsilon ,$$

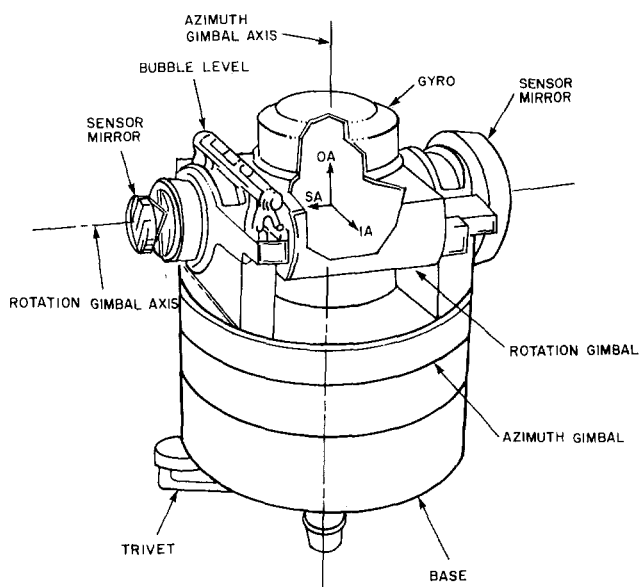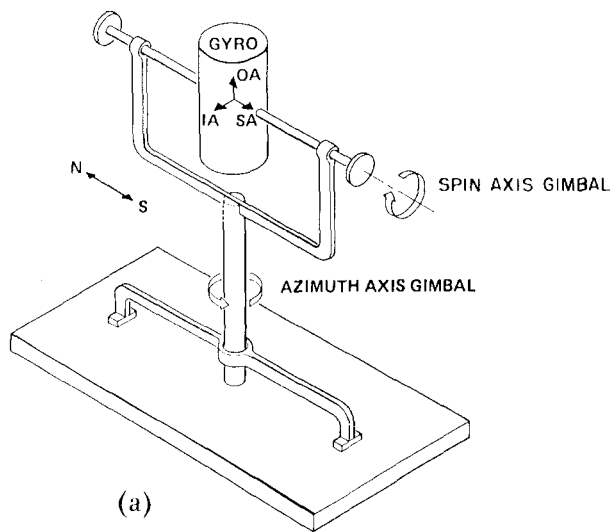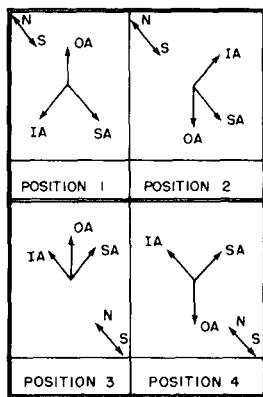where ε represents the sum of other error torques (to be discussed later).

(a)

(b)

Figure 23-40. (a) Functional representation of gyro gimbal mounting.
(b) Functional representation of gyro axes during four-position gyrocompassing.

In this orientation, the ALS sensor mirrors are aligned nearly North-South because of their perpendicularity with the gyro IA. The combination of the gyro torque output and theodolite or other angle measurements between the sensor mirror and the target then provide the desired target azimuth.

Unfortunately, mechanical gyroscopes exhibit substantial torque drift with time. Since these error torques are often large, some means of separating the drift of the azimuth signals is necessary. Traditionally, this is accomplished by repositioning the gyro's axes in four orientations during each sample sequence by moving the gyro on the two gimbal mounts, as shown in the functional representation in Figure 23-40b. This technique is known as four-position gyrocompassing. The repositioning creates a set of observation equations that, when combined, eliminates the average gyro drift errors. However, this same process introduces significant mechanical and electrical errors due to the act of repositioning the gyro. These errors represent the limit of accuracy for the four-positioning gyrocompassing

technique, and until recently were the limiting factor for inertial azimuth measurement.

23.5.3.2 Wheel Speed Modulation. Positioning errors no longer limit inertial azimuth measurement accuracy since recent technology advancement has eliminated the requirement for continuous gyro repositioning. A state-of-the-art mechanical gyroscope has been built with a permanent magnet (PM) wheel which exhibits highly repeatable torque output at any wheel speed. This characteristic makes a technique known as Wheel Speed Modulation a feasible alternative to four-position gyrocompassing [Shearer et al., 1980].

WSM is simply an iterative variation of the gyro's wheel speed, and thus its angular momentum H, between two discrete values. The gyro is maintained in a fixed orientation. For this special case, the gyro torque at each wheel speed is proportional to the respective value of angular momentum, and one can then write two observation equations for the gyro torque in the form

$$M_1 = H_1 \, \omega_{IA} + \varepsilon$$
$$M_2 = H_2 \, \omega_{IA} + \varepsilon + \varepsilon_{WSM} \, .$$

Substracting these two equations yields a new equation which is free of the traditional gyro torque errors ε without repositioning:

$$\Delta M = \Delta H \, \omega_{IA} + \varepsilon_{WSM} \, ,$$

where ε_{WSM}, the torque change due to the speed change, is quite repeatable for a permanent magnet wheel gyroscope and can be readily calibrated.

Sub-arcsecond azimuth measurement uncertainty has been achieved using WSM of a PM gyro [Shearer, 1982].

23.5.3.3 Ring Laser Gyroscope. Finally, recent technological developments in ring laser gyroscope (RLG) technology show promise for accurate azimuth measurement. For this technique, light from a pulsating laser is sent through a beam splitter. The resulting two identical signals are then sent in opposite directions around a closed path back to a signal detector. If no earth rate or other corrupting rates are sensed by the gyro input axis (IA East or West in the horizontal plane), the two signals will arrive at the signal detector exactly in phase with each other. However, if the gyro is sensing a component of earth rate due to its azimuth misalignment from E-W, the effect will be an apparent change in path length between the two directions, thereby resulting in a phase shift between the two signals at the signal detector. This phase shift is directly proportional to the azimuthal component of the earth rate being sensed by the gyro.

To date, high accuracy has not been achieved with Ring Laser Gyroscopes. Some of the practical problems with Ring Laser Gyroscopes, such as lock-in near zero torque and size versus accuracy tradeoffs, are now being addressed by on-

going research. However, these gyros have several desirable attributes. First, they can be sampled at very fast rates to obtain a rapid azimuth measurement. This estimate can be further enhanced by smoothing, averaging or other signal processing techniques. Second, they do not require long warm up periods, making them ideal for use in dormant systems. Finally, since they have no moving parts, high reliability is likely.

23.5.4 Geophysical and Local Environment Effects on Inertial Instruments

Generally, geophysical phenomena can be classified as global or local [Williams, 1970]. Global phenomena, such as polar motion, changes in the day length (Chapter 24), and plate motions (Section 23.2), although severe at times, generally have less effect in inertial instruments than local effects. Figure 23-41 shows the frequencies of some of the more important local motions. Table 23-7 indicates the parameters most affected by these motions and the expected level of disturbance [McKinley, 1975].

Large, even distant earthquakes (Section 23.3.2) can cause significant perturbations in the output of a gyro since ground accelerations sensed by the gyro generate error torques. Inertially derived azimuth data obtained during the passage of earthquake waves will therefore be degraded by the ground motions. However, these degradations are generally short-term phenomena and schemes for extrapolating across earthquake events are commonplace.

Long period crustal motions (Section 23.4) of concern in inertial hardware testing and operation are those caused by atmospheric and hydrostatic loading, fault displacements, and areal strain accumulation. Although these motions can cause sizable rotations and displacements [Gray et al., 1972], they generally have no instantaneous effect on inertial measurement instrumentation, and any cumula-
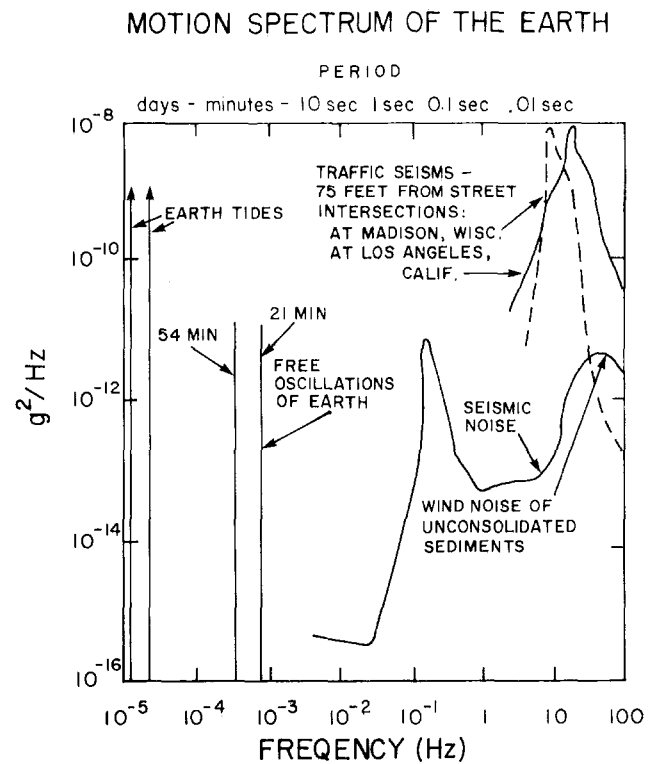

Figure 23-41. Typical natural and cultural ground motion spectrum [Weinstock, 1968].

tive errors can be accurately evaluated by repeated measurements and their effects removed computationally.

Despite the obvious contribution from these geophysical phenomena, variations in the local micro-environment are still the major error source for all inertial instruments. Daily temperature cycles, such as those shown in Figures 23-42 and 23-43, and localized thermal gradients can introduce significant time-varying base tilt motions. These tilts and

Table 23-7. Common gyro test parameters affected by motion environment [McKinley, 1975].

Parameter	Earthquake Waves 5 s–1 min to 100 μgal	Tides 12 · 24 hrs 0.25 μgal	Microseisms 1–0.1 s 10 μgal	Pole Motion 12 · 24 months 0.5 s (latitude)	Cultural/Thermal 0.5 μgal to 10 mgal 0.1 to 10 s
Accelerometer					
Scale Factor	X	X	X		X
Bias	X	X	X		X
Non-Linearity	X	X	X		X
Gyro Scale Factor				X	
Bias				X	
G-Sensitive	X	X			X
G²-Sensitive	X	X			X
Gyrocompass				X	X
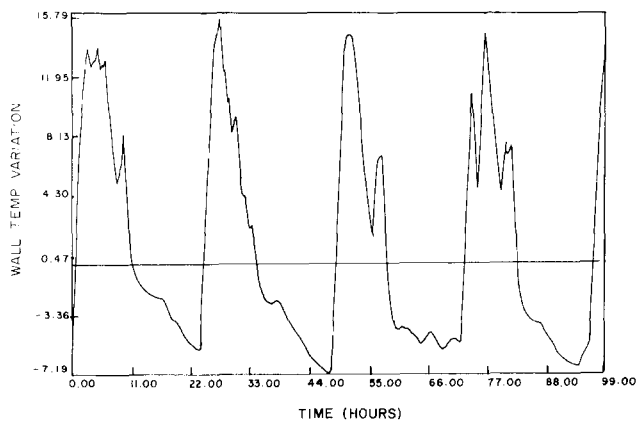
Figure 23-42. Typical temperature variation of test laboratory outside wall surface.

Figure 23-44. Azimuth error due to temperature-induced tilt.

the associated tilt rates can cause azimuth measurement errors of up to several arcseconds (Figure 23-44) and must be compensated for. For example, at 45° latitude, 1 arcsecond of tilt of the gyro IA results in a 1 arcsecond azimuth measurement error. A tilt rate about IA of less than 0.2 arcseconds per hour induces a 1 arcsecond azimuth error.

Two fundamental approaches have been developed for minimizing motion-induced errors in the testing and operation of inertial instrumentation. The most commonly used technique has been an attempt to isolate the test instrument or operational system from disturbing motions by either a passive or active isolation system. An alternate approach is to measure and characterize the perturbing noise field, estimate its contribution to component or system behavior, and remove the error term by signal processing. The characteristic of the noise field will determine the degree of sophistication required in estimating and removing the effects of the disturbing motions. A significant amount of research has been conducted to accurately measure and compensate for base tilt rates and additional research is required to successfully compensate inertial azi-
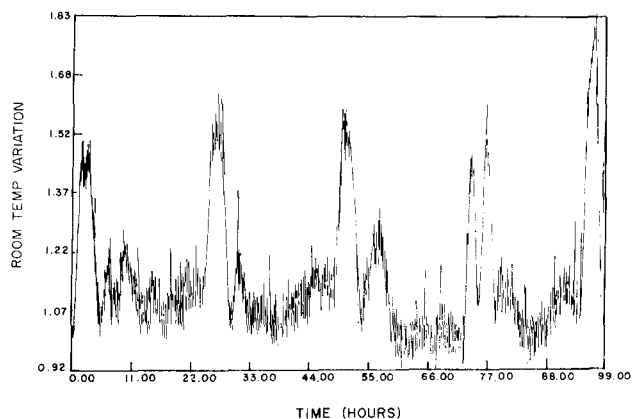
muth measurements for tilt rates to the present sub-arcsecond accuracy objectives.

23.4.5 Azimuth Data Base

A number of agencies maintain a time history of the average motions of azimuth references in the form of azimuth data bases. These azimuth data bases provide important information about the long period motions which affect all inertial test facilities and which can severely degrade test results.

One of the most extensive data bases now being maintained is at the Aerospace Guidance and Metrology Center (AGMC) in Newark, Ohio. Similar data bases described by Roberts [1980] include the Advanced Inertial Test Laboratory at Holloman AFB, the Northrop Test Laboratory Azimuth Facility at Hawthorne, California, and the Charles Stark Draper Laboratory in Cambridge, Mass. However, because of the amounts of data available, the AGMC facility will be described in some detail.

AGMC maintains an azimuth history of a master cube as depicted in Figure 23-45. Three different azimuth references are measured at AGMC. The azimuth of the master cube is determined by periodic observation of Polaris and transfer to the master cube, as previously described. The azimuth of a long line monument is also determined by transferring the azimuth from Polaris to the monument. Finally, azimuth is transferred from the master cube to cubes mounted on long isolation blocks to be used at selected test stations. On the average, ten azimuths are determined per month.

Figure 23-45 shows a plot of repeated azimuth estimates for the master cube azimuth data base for the years 1975–78. Each data point typically represents the average of 16 sightings on Polaris and the master cube. Two trends are immediately apparent, a sinusoidal annual variation and a decreasing steady linear drift. Annual climatic variations and

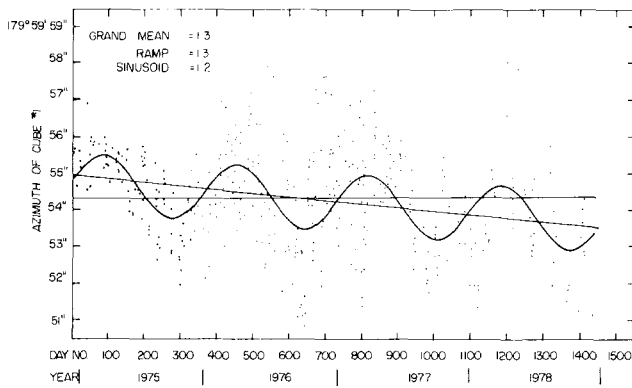Figure 23-43. Ambient room temperature variation near gyro test station.

Figure 23-45. Air Force Guidance and Metrology Center master reference.

a 1.2 year Chandler period variation caused by the earth's elasticity are possible causes of the sinusoidal pattern. The linear drift is probably the result of actual motion of the cube due to thermally, geophysically, and/or structurally-induced stresses.

In addition to the master cube, the azimuths of three other cubes and a long line monument were maintained during the four-year period (1975–78). Their average estimated annual drift rates are shown in Figure 23-46. It is interesting to note the one arcsecond/yr relative drift be-
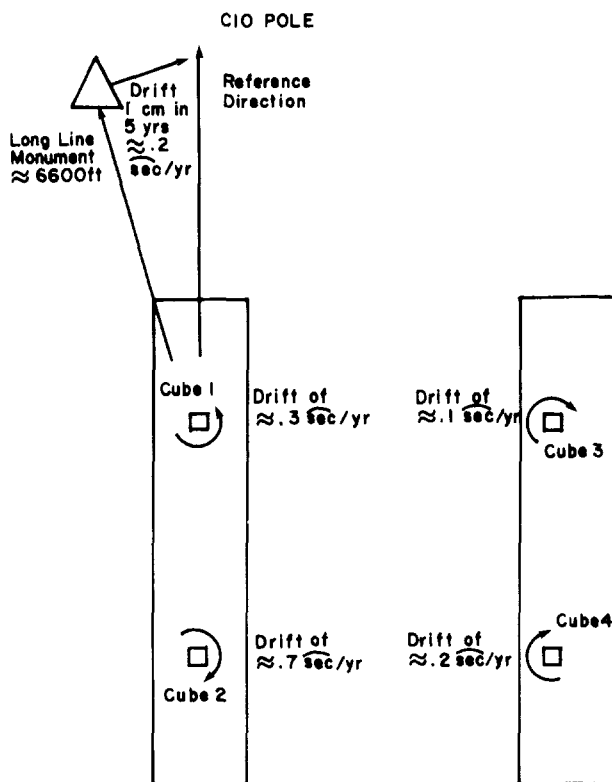
tween cubes 1 and 2. This may be accounted for by differential stress on opposite sides of the isolation mounting block. The block is 24 m long. Thus a change of 0.025 mm per year on one side is enough to produce the resulting apparent azimuth change.

Figure 23-47 shows the annual periodic motions for the AGMC facility as a whole, as well as for the four cubes shown in the previous diagram. Possible causes of the estimated facility motion of 0.7 arc s/yr include annual variations in precipitation and runoff patterns, seasonal variations in solar heating between opposite sides of the building, and freezing and thawing of the ground. Temperature gradients across the width of the support blocks can also account for the periodic motions of the cubes, especially cubes 2 and 3. A temperature change of 0.16 degree is enough to generate these types of motions.

A similar inertial azimuth measuring device was used by Dieselman, et al. [1970] to monitor a reference cube at an inertial component test facility similar to AGMC. Tilt and temperature data were collected and are plotted with the azimuth estimates in Figure 23-48. The reference cube shows long period annual variations similar to the ones for AGMC. Note that the long period azimuth variations are very well correlated with the long period tilt and temperature data. This data suggests that the rotation shown are most likely attributable to thermal and insolation effects on the local topography as well as the building (Section 23.4).
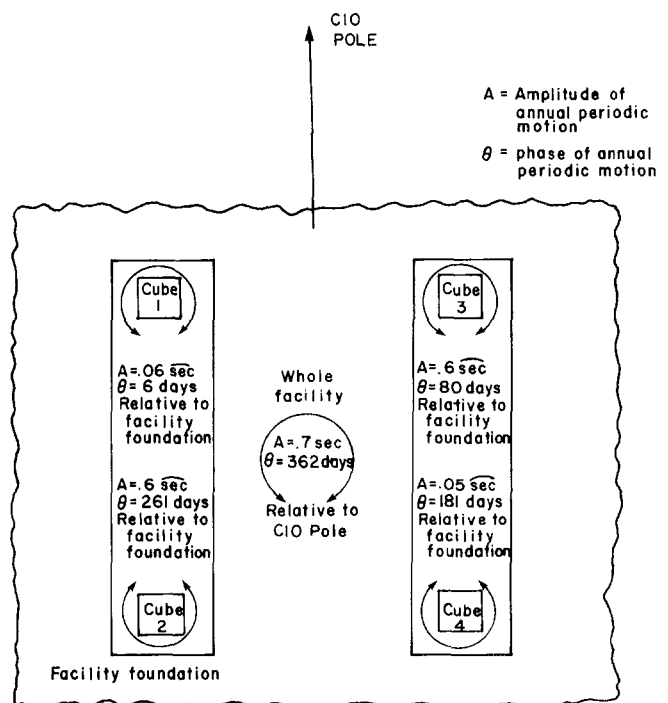

Figure 23-46. Average annual motion of AGMC reference cubes.

Figure 23-47. Mean annual periodic motions for the years 1975 to 1978, AGMC.
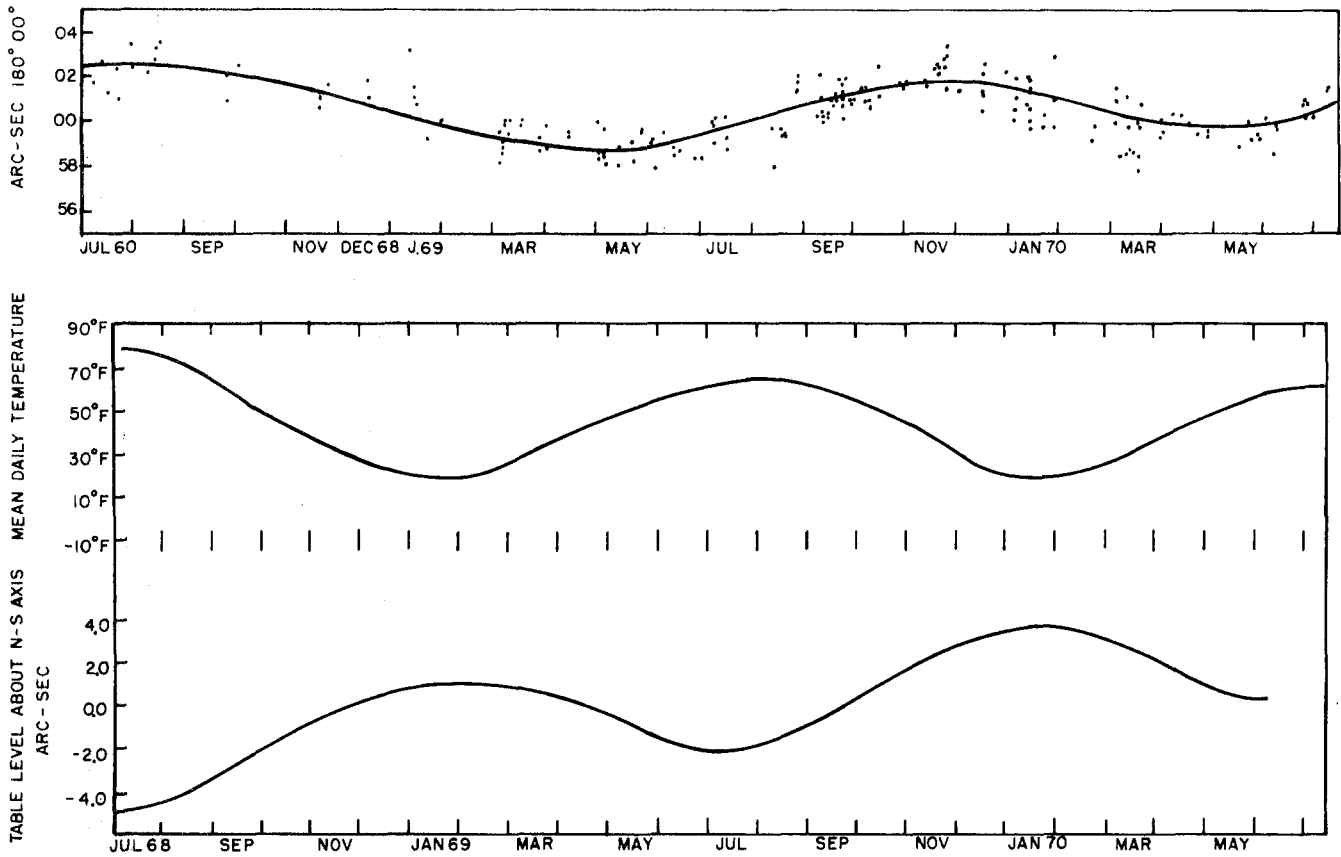
Figure 23-48. Long period variations of master reference cube, AGMC.

23.5.6 Conclusions

In summary, as modern systems become increasingly sophisticated, the effects of the ambient motion environment on their performance are also dramatically increasing. The ability to accurately measure and compensate for these environmental influences is complicated by the fact that the very motions being measured tend to degrade the performance of the measurement tool. Thus, what was once thought to be a simple static problem of classical geodesy is now a dynamic concern of modern geophysics.

Looking toward the future, one can only predict that the increasing demand for better measurement accuracy required to support new systems will continue to amplify the impact of the dynamic environment in which we operate. Continued research in rotational geophysics is required to ensure parity of the measurement technology with the operational requirements.

REFERENCES

Agnew, D.C., *Strain Tides at Pinon Flat: Analysis and Interpretation*, Ph.D. Thesis, University of California, San Diego, 1979.

Aki, K. and P.G. Richards, *Quantitative Seismology*, 1, Freeman, San Francisco, 1980.

Algermissen, S., *Seismic Risk Studies in the United States*, 4th World Conference on Earthquake Engineering, Santiago, Chile, 1969.

Anderson, D.L. and R.S. Hart, "An Earth Model Based on Free Oscillations and Body Waves," *J. Geophys. Res.*, 81: 1461–1475, 1976.

Anderson, E.G., "Modeling of Physical Influences in Sea Level Records for Vertical Crustal Movement Detection," Proceedings 9th Geodesy/Solid Earth and Ocean Physics (GEOP) Conference, *Report 280*, Dept. Geodetic Science, Ohio State University, Columbus, 145–152, 1978.

Baker, T., "What Can Earth Tide Measurements Tell Us about Ocean Tide or Earth Structure?," Proceedings 9th Geodesy/Solid Earth and Ocean Physics (GEOP) Conference, *Report 280*, Dept. Geodetic Science, Ohio State University, Columbus, 299–307, 1978.

Bath, M., *Introduction to Seismology*, Wiley, New York, 1973.

Battis, J., "Regional Modification of Acceleration Attenuation Functions," *Bull. Seismol. Soc. Am.*, 71: 1309–1321, 1981.

Beaumont, C., "Linear and Nonlinear Interactions between the Earth Tide and a Tectonically Stressed Earth," Proceedings 9th Geodesy/Solid Earth and Ocean Physics (GEOP) Conference, *Report 280*, Dept. Geodetic Science, Ohio State University, Columbus, 313–318, 1978.

Beaumont, C. and J. Berger, "Earthquake Prediction: Modification of the Earth Tide Tilts and Strains by Dilatancy," *Geophys. J. Royal Astron. Soc.*, 39: 111–121, 1974.

Beaumont, C. and A. Lambert, "Crustal Structure from Surface Load Tilts, Using a Finite Element Model," *Geophys. J. Royal Astron. Soc.*, 29: 203–226, 1972.

Ben-Menahem, A. and S.J. Singh, *Seismic Waves and Sources*, Springer Verlag, New York, 1981.

Berger, J. and C. Beaumont, "An Analysis of Tidal Strains from the USA: II The Inhomogeneous Tide." *Bull. Seismol. Soc. Am.*, 66: 1821–1846, 1976.

Berger, J. and J. Levine, "The Spectrum of Earth Strain from 10^{-8} to 10^2 Hz," *J. Geophys. Res.*, 79: 1210–1214, 1974.

Berger, J. and R. Lovberg, "Earth Strain Measurements with a Laser Interferometer," *Science*, 170: 296–303, 1970.

Bird, J.M. and B. Isacks (eds.), *Plate Tectonics*, selected papers from the *J. Geophys. Res.*, 1972.

Brazee, R., *Analysis of Earthquake Intensities With Respect to Attenuation, Magnitude and Rate of Recurrence*, NOAA, 1976.

Brown, L.D., "Recent Vertical Crustal Movement Along the East Coast of the United States," *Tectonophysics*, 44: 205–231, 1978.

Brune, J., "Surface Waves and Crustal Structures," *The Earth's Crust and Upper Mantle*, edited by P. Hart, AGU, Monograph 13, Washington, D.C. 1969.

Brune, J. and J. Oliver, "The Seismic Noise of the Earth's Surface," *Bull. Seismol. Soc. Am.*, 49: 349–353, 1959.

Bullen, K.E., *An Introduction to the Theory of Seismology*, Cambridge University Press, Cambridge, U.K., 1965.

Cabaniss, G.H., "The Measurement of Long Period and Secular Deformation with Deep Borehole Tiltmeters," Proceedings 9th Geodesy/Solid Earth and Ocean Physics (GEOP) Conference, *Report 280*, Dept. Geodetic Science, Ohio State University, Columbus, 165–169, 1978.

Cabaniss, G.H. and D.H. Eckhardt, "The AFCRL Earth Tide Program," AFCRL TR-73-0084, 1973.

Cartwright, D., "The IOS Program of Tidal Definition in the North Atlantic Ocean," *Proceedings 9th Earth Tide Symposium*, Columbia University, New York, 1982.

Cartwright, D. and A. Edden, "Corrected Tables of Tidal Harmonics," *Geophys. J. Royal Astron. Soc.*, 33: 253–264, 1973.

Castle, R.O., J.P. Church, and M.R. Elliot, "Aseismic Uplift in Southern California," *Science*, 192: 251–253, 1976.

Chilton, E.G., "Design Requirements for a Testing Laboratory for Inertial Guidance Systems and Components," Air Transport and Space Meeting, New York, 1964.

Chinnery, M.A., "The Frequency of Very Large Earthquakes," *Science*, 190(4222), 1975.

Clark, S.P. and A.E. Ringwood, "Density Distribution and Constitution of the Mantle," *Rev. Geophys.*, 2: 35–88, 1964.

Committees on Geodesy and Seismology, National Research Council, "Geodetic Monitoring of Tectonic Deformation — Toward a Strategy," National Academy of Sciences, Washington, D.C., 109, 1981.

Cox, A. (ed.), *Plate Tectonics and Geomagnetic Reversals*, Freeman, San Francisco, 1973.

Crowford, R., *The Air Force Manual for Design and Analysis of Hardened Structures*, AFWL-TR-74-102, Air Force Weapons Laboratory, Kirtland AFB, N. Mex., 1974.

Crowley, F.A. and H.A. Ossing, "An Analysis of the Vibration Environment with Applications to Single-Degree-of-Freedom Gyroscope Performance Tests," AIAA Paper No. 70-951, 1970.

Currie, D.G. and R. Salvermoser, "The Array Eyepiece System for the Wild T-4 Theodolite," *Program Review and Field Results*, University of Maryland, 1981.

Department of Defense, *Glossary of Mapping, Charting and Geodetic Terms*, Defense Mapping Agency Topographic Center, Washington, D.C., June 1973.

Dieselman, J., R.L. McLaughlin, K. Millo, and L.B. Thompson, "Recent Developments in the Testing of High Performance Gyrocompass Devices," *Proceedings 5th Guidance Test Symposium*, 2, 1970.

Dietz, R.S. and J.C. Holden, "Reconstruction to Pangaea: Breakup and Dispersion of Continents, Permian to Present," *J. Geophys. Res.*, 75: 4939-49-56, 1970.

Donovan, N., B. Bolt, and R. Whitman, *Technology Review*, Cambridge, Mass., May 1977.

Dorman, J., "Seismic Surface Wave Data on the Upper Mantle," *The Earth's Crust and Upper Mantle*, edited by P.J. Hart, AGU, Monograph 13, Washington, D.C., 1969.

Everndon, J.F., "Gravity Profiles in Southern California," *Earthquake Prediction: An International Review*, AGU, Washington, D.C. 485–496, 1981.

Ewing, C.E. and M.M. Mitchell, *Introduction to Geodesy*, Elsevier, New York, 1970.

Farrell, W.E., "Deformation of the Earth by Surface Loads," *Rev. Geophys. Space Phys.*, **10:** 761–797, 1972.

Fix, J., "Ambient Earth Motions in the Period Range from 0.1 to 2560 Sec, *Bull. Seismol. Soc. Am.*, **62:** 1753–1760, 1972.

Garland, G.D., *Introduction to Geophysics*, W.B. Saunders Co., Philadelphia, 1971.

Gass, I.G., "Ophiolites," *Sci. Am.*, August 1982.

Goad, C.C., "Gravimetric Tidal Loading Computed from Integrated Green's Functions," *J. Geophys. Res.*, **85:** 2679–2683, 1980.

Gray, R.A., G.H. Cabaniss, F.A. Crowley, H.A. Ossing, T.S. Rhoades, and L.B. Thompson, "Earth Motions and Their Effects on Inertial Instrument Performance," AFCRL-72-0278, AD748274, 1972.

Greensfelder, R., "Maximum Credible Rock Acceleration from Earthquakes in California," California Division of Mines and Geology, Map Sheet 25, 1974.

Harrison, J.C., "Cavity and Topographic Effects in Tilt and Strain Measurement," *J. Geophys. Res.*, **81:** 319–328, 1976.

Harrison, J.C., "Implications of Cavity, Topographic, and Geologic Influences on Tilt and Strain Measurements," Proceedings 9th Geodesy/Solid Earth and Ocean Physics (GEOP) Conference, *Report 280*, Dept. Geodetic Science, Ohio State University, Columbus, 283–287, 1978.

Harrison, J.C., and K. Herbst, "Thermoelastic Strains and Tilt Revisted," *Geophys. Res. Lett.*, **4:** 535–537, 1977.

Herbst, K., "Interpretation of Tilt Measurements in the Period Range above that of the Tides," AFGL-TR-79-0093, ADA074525 (Translation No. 109), 1979.

Holzner, T.L., S.N. Davis, and B.E. Lofgren, "Faulting Caused by Groundwater Extraction in South-Central Arizona," *J. Geophys. Res.*, **84:** 603–612, 1979.

Huggett, G.R., L.E. Slater, and J. Langbein, "Fault Slip Episodes near Hollister, California: Initial Results Using a Multiwavelength Distance Measuring Instrument," *J. Geophys. Res.*, **82:** 3361–3368, 1977.

Isacks, B., J. Oliver, and L. Sykes, "Seismology and the New Global Tectonics," *J. Geophys. Res.*, **73:**(18), 1968.

Iyer, H., *The History of Science of Microseisms*, VESIAC Report 4410-64-X, University of Michigan, Ann Arbor, 1964.

Jackson, D.D. and W.B. Lee, "The Palmdale Bulge — An Alternate Interpretation," *Eos, Trans. AGU*, **60, 810**, 1979.

Jaenke, M.G., "A Proposed Model for the Rotational Motions of a Test Pad," AIAA Paper No. 74-855, 1974.

Johnston, J.C., Z.A. Cybriwsky, and G.K. Leblanc, "The Regulatory Guide 1.60 Its Content and Applicability" abstract, *Earthquake Notes*, **51**(3), 1980.

Kanamori, H., "Velocity and Q of Mantle Waves," *Phys. Earth Planet. Int.*, **2:** 259–275, 1970.

Kanamori, H. and J. Cipar, "Focal Process of Great Chilean Earthquake," May 22, 1960, *Phys. Earth Planet. Int.*, **9:** 128–136, 1974.

Kanamori, H., "The Energy Release in Great Earthquakes," *J. Geophys. Res.*, **82**(20), 1977.

Kayton, M., "Fundamental Limitations on Inertial Measurements," *Guidance and Control*, Academic Press, New York, 1962.

Kuo, J.T., "Static Response of a Multilayered Medium Under Inclined Surface Loads," *J. Geophys. Res.*, **74:** 3195–3207, 1969.

Kuo, J.T., "The Inverse Problem: Ocean Tides Derived from Earth Tide Observations," Proceedings 9th Geodesy/Solid Earth and Ocean Physics (GEOP) Conference, *Report 280*, Dept. Geodetic Science, Ohio State University, Columbus, 319–326, 1978.

Lambert, A. and C. Beaumont, "Nano Variations in Gravity Due to Seasonal Groundwater Movements: Implications for the Gravitational Detection of Tectonic Movements," *J. Geophys. Res.*, **82**, 297–306, 1977.

Lambert, A. and J.O. Liard, "A Search for Long-Term Earthquake Precursors in Gravity Data in the Charlevoix Region, Quebec," *Earthquake Prediction: An International Review*, AGU, Washington, D.C., 473–483, 1981.

Lennon, G.W. and T.F. Baker, "The Earth Tide Signal and Its Coherency," *Qtrly. J. Roy. Astron. Soc.*, **14:** 161–182, 1973.

Levine, J., "Strain-Tide Spectroscopy," *Geophys. J. Royal Astron. Soc.*, **54:** 27–41, 1978.

Levine, S.A. and A. Gelb, "Geodetic and Geophysical Uncertainties Fundamental Limitations on Terrestrial Inertial Navigation," AIAA Guidance Control and Flight Dynamics Conference, Pasadena, Calif., 1968.

Lewkowicz, J.F. and G.H. Cabaniss, "Near-Field Static Tilts from Surface Loads," AFGL-TR-80-0221, ADA094123, 1980.

Lindh, A.G. and D.M. Boore, "Control of Rupture by Fault Geometry During the 1966 Parkfield Earthquake," *Bull. Seismo. Soc. Am.*, **71,** 95–116, 1981.

Longman, I.M., "A Green's Function for Determining the Deformation of the Earth Under Surface Mass Loads, I. Theory," *J. Geophys. Res.*, **67:** 845–850, 1962.

McGuire, R., *FORTRAN Computer Program for Seismic Risk Analysis*, U.S. Geological Survey, Open File Report, 76-67, 1976.

McKinley, H.L., "Geokinetic and Geophysical Influence on 1980's ICBM Guidance," AIAA Guidance and Control Conference, Boston, Mass, 1975.

Melchior, P., *The Earth Tides*, Pergamon Press, Oxford, 1966.

Minster, J.B. and T.H. Jordan, "Present day plate motions," *J. Geophys. Res.*, **83:** 5331–5354, 1978.

Mogi, K., "Earthquake Prediction in Japan," *Earthquake Prediction: An International Review*, AGU, Washington, D.C., 635–666, 1981.

Morgan, W.J., "Rises, Trenches, Great Faults, and Crustal Blocks," *J. Geophys. Res.*, **73**: 1959, 1968.

Morgan, W.J., "Plate Motions and Deep Mantle Convection," *Studies in Earth and Space Sciences*, Geol. Soc. Amer. Mem. 132, 1972.

Mueller, Ivan I., *Spherical and Practical Astronomy as Applied to Geodesy*, Ungar, New York, 1969.

Nuttli, O., "The Mississippi Valley Earthquakes of 1811 and 1812: Intensities, Ground Motion and Magnitudes," *Bull. Seismol. Soc. Am.*, **63**: 227–248, 1973.

Nuttli, O., *The Relation of Sustained Maximum Ground Acceleration and Velocity to Earthquake Intensity and Magnitude*, U.S. Army Engineer Waterways Experimentation Station, Miscellaneous Paper S-73-1, 1979.

Ossing H. and R. Gray, *A Survey of the Ambient Motion Environment in the Southwestern United States*, Interim Scientific Report AFGL-TR-78-0052, ADA056872, 1978.

Parke, M.E., "Open Ocean Tide Modelling," Proceedings 9th Geodesy/Solid Earth and Ocean Physics (GEOP) Conference, *Report 280*, Dept. Geodetic Science, Ohio State University, Columbus, 289–297, 1978.

Predicting Earthquakes, Panel on Earthquake Prediction, National Academy of Sciences, Washington, D.C., 1976.

Raisler, R.B. and J.C. Fatz, "Stability of Stable Areas," AIAA Paper No. 74-859, 1974.

Reilinger, R. and L.D. Brown, "Neotectonic deformation, near surface movements and systematic errors in U.S. releveling measurements: Implications for earthquake prediction," *Earthquake Prediction: An International Review*, AGU, Washington, D.C., 422–440, 1981.

Richter, C., *Elementary Seismology*, Freeman, San Francisco, 1958.

Roberts, G.E., "MX laboratory azimuth data base study (Status report)," Geodynamics Corporation, Santa Barbara, CDR-0008 (SR38OU)-1, 1980.

Savage, J.C., W.H. Prescott, M. Lisowski, and N.E. King, "Strain Accumulation in Southern California 1973–1980," *J. Geophys. Res.*, **86**: 6991–7001, 1981.

Schureman, P., "Manual of Harmonic Analysis and Prediction of Tides," *Spec. Pub. 98*, U.S. Coast and Geodetic Survey, 1958.

Schwiderski, E.W., "Ocean tides, Part I: Global Tidal Equations," *Marine Geodesy*, **3**: 161–187, 1979.

Schwiderski, E.W., "On Charting Global Ocean Tides," *Rev. Geophys. Space Phys.*, **18**: 38–61, 1980.

Schwiderski, E.W., "Ocean tides, Part II: A Hydrodynamic Interpolation Model," *Marine Geodesy*, **3**: 219–255, 1980.

Seismic Noise Survey, Geotech Technical Report 63-45, **1**: Garland Texas, 1963.

Seismic Noise Survey, Geotech Technical Report 63-45, **2**: Garland, Texas, 1963.

Shearer, J.A., "Evaluation of an Advanced Gyro and Wheel Speed Modulation for Highly Accurate Azimuth Determination," AFGL-TR-82-0016, AD114640, 1982.

Shearer, J.A., "Error Analysis and Performance Data from an Automated Azimuth Measuring System," AIAA Paper No. 80-1793, 1980.

Simmons, B.J., R.M. Hanes, and F.S. Heming, "Dynamic Analysis of Test Platform," AIAA Paper No. 81-1816, 1981.

Simpson, D.W. and P.G. Richards (eds.), *Earthquake Prediction: An International Review*, AGU, Washington, D.C., 1981.

Slemmons, D., *Faults and Earthquake Magnitude*, U.S. Army Engineers Waterways Experimentation Station, Miscellaneous Paper S-73-1, 1977.

Smith, D.E., "Spaceborn Ranging System," Proceedings 9th Geodesy/Solid Earth and Ocean Physics (GEOP) Conference, *Report 280*, Dept. Geodetic Science, Ohio State University, Columbus, 59–64, 1978.

Smith, D.E., R. Kolenkiewicz, P.J. Dunn, and M.H. Torrence, "The Measurement of Fault Motion by Satellite Laser Ranging," *Tectonophysics*, **52**: 59–67, 1979.

Stein, R.S., "Discrimination of Tectonic Displacement from Slope Dependent Errors in Geodetic Leveling from Southern California, 1953–1979," *Earthquake Prediction: An International Review*, AGU, Washington, D.C., 441–456, 1981.

Strange, W., "The Impact of Refraction Correction on Leveling Interpretations in Southern California," *J. Geophys. Res.*, **86**: 2809–2824, 1981.

Takeuchi, H., "On the Earth Tide," *J. Fac. Sci*, University of Tokyo, Sec II-7; Part II, 1–7, 1951.

Tsutsumi, K., "A Program of Study on Long-Term Earth Tilts," AFCRL-70-0268, AD724868, 1970.

Verhoogen, J., F.J. Turner, L.E. Weiss, C. Wahrhaftig, and W.S. Fyfe, *The Earth: An Introduction to Physical Geology*, Holt, Rinehart & Winston, New York, 1970.

Wahr, J.M., *The Tidal motions of a Rotating, Elliptical, Elastic, and Oceanless Earth*, Ph.D Thesis, University of Colorado, 1979.

Walcott, R.I., "Late Quaternary Vertical Movements in Eastern North America: Quantitative Evidence of Glacio-Isostatic Rebound," *Rev. Geophys. Space Phys.*, **10**: 849–884, 1972.

Weinstock, H., "Design of Precision Tilt and Rotational Vibration Isolation System for Inertial Sensor Testing," AIAA Paper No. 68-894, 1968.

Whitcomb, J.H., "New Vertical Geodesy," *J. Geophys. Res.*, **81**: 4937–4944, 1976.

Williams, O.W., "A Review of Geophysical Effects and Suggested Testing Conditions Related to Advanced Inertial Components" Paper presented to USAF Scientific Advisory Board Ad Hoc Committee on Geophysical Effects on Inertial Instruments, 1970.

Willmore, P.L. (ed.), *Manual of Seismological Observatory Practice*, World Data Center A for Solid Earth Geophysics, Report SE-20, 1979.

Wilson, J.T., "A New Class of Faults and their Bearing on Continental Drift," *Nature* **207**: 343–347, 1965.

Wittry, J.R., "Description of an Inertial Test Facility Incorporating a Passively Isolated and Actively Stabilized Platform," AIAA Paper No. 69-863, 1969.

Wyatt, F., "Displacement of Surface Monuments: Horizontal Motion," *J. Geophys. Res.*, **87**: 979–989, 1982.

Wyatt, F., G.H. Cabaniss, and D.C. Agnew, "A Comparison of Tiltmeters at Tidal Frequencies," *Geophys. Res. Ltrs.*, **9**: 743–746, 1982.

Wyllie, P.J., *The Dynamic Earth,* Wiley, New York, 1971.

Zienkiewicz, O.C., *The Finite Element Method in Structural and Continuum Mechanics,* McGraw-Hill, New York, 1967.

Zschau, J., "Tidal Sea Load Tilt of the Crust, and Its Application to the Study of Crustal and Upper Mantle Structure," *Geophys. J. Royal Astron. Soc.*, **44**: 577–593, 1976.